Title

MECHANISM OF GASEOUS PERMEATION THROUGH GLASS, SINGLE-CRYSTAL SILICON, AND GERMANIUM; AND STRESS-ENHANCED GASEOUS PERMEATION THROUGH ALUMINA BODIES

Author

Studt, Perry Louis.

Publication Date

1962-09-26

Thesis/dissertation

UCRL 10466

University of California

Ernest O. Lawrence
Radiation Laboratory

MECHANISM OF GASEOUS PERMEATION THROUGH GLASS, SINGLE-CRYSTAL SILICON, AND GERMANIUM; AND STRESS-ENHANCED GASEOUS PERMEATION THROUGH ALUMINA BODIES

Berkeley, California

DISCLAIMER

Research and Development

UCRL-10466
UC-25 Metals, Ceramics,
and Materials
TID-4500 (18th Ed.)

UNIVERSITY OF CALIFORNIA

Lawrence Radiation Laboratory
Berkeley, California

Contract No. W-7405-eng-48

MECHANISM OF GASEOUS PERMEATION THROUGH GLASS, SINGLE-CRYSTAL SILICON, AND GERMANIUM; AND STRESS-ENHANCED GASEOUS PERMEATION THROUGH ALUMINA BODIES

Perry Louis Studt
(Thesis)

September 26, 1962

Printed in USA. Price $2.50. Available from the
Office of Technical Services
U. S. Department of Commerce
Washington 25, D.C.

MECHANISM OF GASEOUS PERMEATION THROUGH GLASS, SINGLE-CRYSTAL SILICON, AND GERMANIUM; AND STRESS-ENHANCED GASEOUS PERMEATION THROUGH ALUMINA BODIES

Contents

MECHANISM OF GASEOUS PERMEATION THROUGH GLASS, SINGLE-CRYSTAL SILICON, AND GERMANIUM; AND STRESS-ENHANCED GASEOUS PERMEATION THROUGH ALUMINA BODIES

Perry Louis Studt

Lawrence Radiation Laboratory
University of California
Berkeley, California

September 26, 1962

ABSTRACT

This study consists of two parts. The first part is a development of a more fundamental and quantitative understanding of the transport of noble gas atoms through glasses and single-crystal Si and Ge. Literature pertinent to gaseous permeation through these materials is reviewed with respect to experimental data and explanations for the observed permeations. A series of equations for the permeation coefficient is developed in terms of the solubility coefficient and diffusion coefficient. The theory is further extended for Si and Ge to include calculation of the activation energy for diffusion and solution. From this resulting quantitative theory it is possible to explain the relationship of glass modifiers to permeability, and the increase in density with increasing amounts of glass modifiers up to about 10 mol percent, and to identify the forces probably responsible for the observed activation energies for diffusion and solution.

The second part consists of an investigation of the effect of induced stresses on permeation through normally impermeable high-purity Al_2O_3 bodies. Stress-enhanced permeation is found and related to the microstructure of these bodies. Adsorption of helium on internal surfaces of these bodies is also found as well as initial stress-free permeability for specimens that later become impermeable. The permeability found is considered to be significantly different from that discussed for glass and single-crystal silicon and germanium.

I. INTRODUCTION

In recent years the development of nuclear reactors as high-temperature energy sources has necessitated increasing use of refractory ceramic materials as structural members and fissile fuels. Glass-containing fuel elements have also been contemplated. A portion of the fission products generated by the fission process are gaseous and radioactive. Because of the high temperatures existing in reactors, evolution of such gases in confined spaces could cause high pressures and biologically dangerous discharge of radioactivity. Thus, permeation of gases through such materials is important.

Previous investigations of the evolution of noble gases from crystalline uranium oxides, carbides, etc., have been by postirradiation gaseous evolution experiments. The possibility exists that the gaseous evolution process during reactor operation may differ from the one investigated in such experiments. The dynamic stress-strain environment is significantly different owing to the very large local stresses and lattice disruptions that exist around fissioning atoms. Grain boundaries may be weaker regions in the fuel matrix. Consequently, portions of the grain-boundary surfaces may be separated momentarily by such stresses and gaseous evolution may be along such temporarily opened paths. Investigation of both the permeation process through glass and single crystals, and the effects of stress on permeation through brittle polycrystalline ceramic materials will therefore be of theoretical and practical value.

Because of the complex nature of polyphase-polycrystalline ceramics in which one phase may be a glass, it is necessary to consider permeation through glass, through crystal lattice, and along grain boundaries. Therefore, Part I of this study establishes the necessary theoretical background for permeation of gas through glass and crystals. Following this part the passage of gas through polycrystalline Al_2O_3 under cyclic stresses is analyzed.

II. GAS PERMEATION THROUGH GLASS, SINGLE-CRYSTAL SILICON, AND GERMANIUM

Published experimental data, previous analyses of these data, and the resulting theories for passage of rare gas atoms through glass are presented. The proposed theory is discussed, then compared to these available data. From this theory and its agreement with the available data, conclusions are drawn as to the location of gas atoms in glass, Si, and Ge, the state of the gas atom; the effect of composition on this state; and finally the mode of passage through the solids.

A. Mathematics of Flow of Gas Through Membranes

Darcy's law[1] states

$$F = K \Delta P \frac{A}{\ell} \quad , \tag{1}$$

where F = flow rate, in cc gas at STP per sec,

K = permeation constant, in cc gas at STP per atmos-unit thickness of membrane,

ΔP = pressure differential across membrane,

A = conducting area of membrane,

ℓ = thickness of membrane.

It is possible to relate K to a solubility coefficient and a diffusion coefficient if we make several simplifying assumptions. First, we assume the concentration, C, follows Henry's law as

$$C = SP, \tag{2}$$

where C = concentration of gas atoms per cc of solid,

S = solubility coefficient, which is a constant of proportionality dependent on temperature only,

P = pressure of gas in equilibrium with concentration, C, of gas in solid.

Second, we assume that the diffusion coefficient, D, is a constant independent of concentration and dependent only on the temperature. Third, we assume that the concentration at any point in the solid is an equilibrium one. Fourth, we assume that the diffusion process is the

rate-controlling process for passage of gas atoms through the membrane. That is, adsorption and desorption at the surfaces do not control rate or concentration. The flow rate may now be rewritten as

$$\frac{F}{A} = K' \frac{\Delta C}{\Delta L}, \text{ where } K' = \frac{K}{S}, \tag{3a}$$

or

$$J = K' \frac{dC}{dX}, \tag{3b}$$

where J = flow per unit time-unit area,

X = distance in direction of flow.

The diffusion coefficient is given by Ficks' first law as

$$J = D \frac{dC}{dX}, \text{ where } D = \text{diffusion coefficient.} \tag{4}$$

Therefore, K' or $\frac{K}{S}$ is equal to the diffusion coefficient as defined by Ficks' first law. Thus, the permeability coefficient is

$$K = DS. \tag{5}$$

With this equation we have identified the overall permeation coefficient as being in fact a product of two other more fundamental constants, each of which is determined by a different step in the overall permeation process. The diffusion coefficient, D, depends on the mechanism of gas atom transport through the glass structure. The solubility coefficient, S, depends on the mechanism of solution of the gas atoms in the glass structure.

Study of Ficks' first and second laws as they pertain to permeation shows that K can be found from the first law, i.e., steady-state flow conditions, and that D may be found from the second law, i.e., from the flow-rate time dependence. Since both D and K are known we can then calculate S, the solubility coefficient.

Many equivalent solutions to Ficks' second law have been presented in the literature from time to time.[2-8] Each one lends itself most readily to analysis of the data in a different way. To visualize these alternative treatments it is necessary to consider the forms of the experimental data. The experiment may be performed in two ways.

A given amount of gas may be introduced into a chamber on one side of the membrane and the pressure rise in a known volume on the other side of the membrane continuously recorded. Or the flow rate of the gas through the membrane may be continuously recorded by means of pressure sensors or a mass spectrometer.

The first method yields curves of the form given in Fig. 1. The time lag is $L = \frac{D}{6\ell^2}$, and is thoroughly covered by Barrer.[7]

In the second method curves of the form given in Fig. 2 are found. Such a curve may be integrated graphically to obtain one like Fig. 1. However, this is generally not done, since solution of Ficks' law gives the equation for the curve of Fig. 2. Therefore, fitting a calculated curve to the experimental curve yields the value of D.

Three fitting methods have been presented in the literature.[4, 6, 8] The first considers the slope at very short times.[6] A solution to the time-dependent equation is found that simplifies for small times. A second method considers times other than small ones and thus fits all but the beginning portion of the curve.[4] The third method considers the inflection point of the curve.[8] Experimental and calculated inflection points are matched to determine the diffusion coefficient.

A further experimental variation is to compare the diffusion coefficient found from the rise in flow rate with that calculated from the decay in flow rate on instantaneous removal of He from the high-pressure side of the membrane.[3, 9] A possible advantage of using the decay scheme is that there is no stress applied to the membrane through He pressure. This effect, however, should not be important for a pressure of 1 to 2 atmospheres and a usual membrane thickness of approx 1 mm.

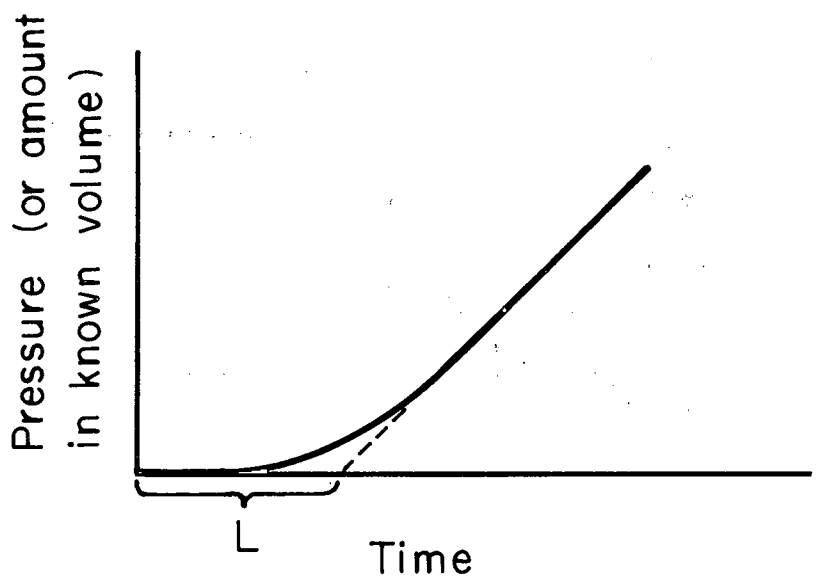

Fig. 1. Amount of gas permeating a membrane as a function of time.

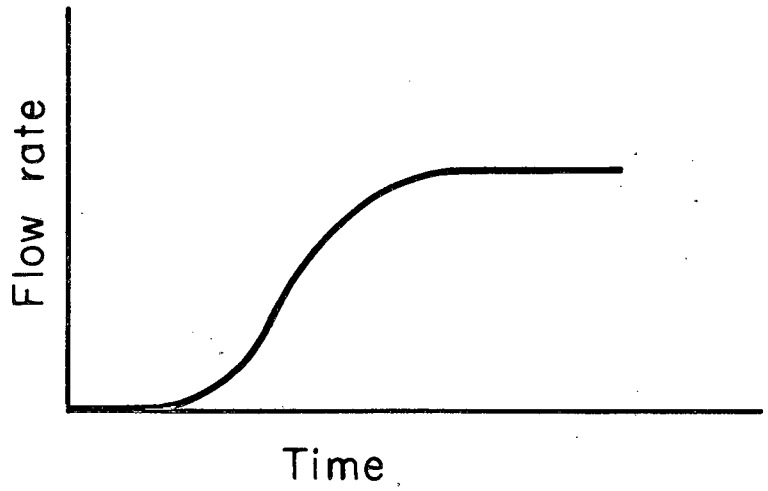

MU-28441

Fig. 2. Rate of gas permeation of membrane as a function of time.

B. Literature Review

1. Experimental Data for Glass

Data sufficiently complete and accurate to be used as a test for a quantitative explanation of gas flow through glass are given in Tables I through III. Table I consists of a recompilation of the glass compositions for the important published materials. Table II is a listing of the best data available for He flow through these glasses. Table III is a compilation of the same data for flow of Ne through these glasses. Table IV is a summary of the data on flow of He through single-crystal germanium and silicon.

All these data have been evaluated in the form of

$$D = D_0 \exp(-\Delta H_D/RT), \quad S = S_0 \exp(-\Delta H_s/RT), \quad K = K_0 \exp(-\Delta H_K/RT. \quad (6)$$

The values for D, S, And K have been plotted vs 1/T on semilog paper and straight lines drawn through the points. Figures 3, 4, and 5 are plots of D, S, and K, respectively, from the data from Tables I, II, and III. In the case of He diffusion through and solution in fused quartz, Swets et al.[3] consider the best least-mean-squares fit to be two curves. All the other curves are best approximated by single straight lines. These equations are, for He in fused quartz,[3]

T = 24° C to 300° C,

$$D = 3.04 \times 10^{-4} \exp\left(\frac{-5580 \pm 56 \text{ cal/g atom}}{RT}\right), \text{ in } \text{cm}^2/\text{sec}, \quad (7a)$$

$$S = 1.99 \times 10 \exp\left(-\frac{-680 \pm 60 \text{ cal/g atom}}{RT}\right), \text{ in } \frac{\text{atoms}}{\text{cc-atm}}, \quad (7b)$$

T = 300° C - 1034° C,

$$D = 7.40 \times 10^{-4} \exp\left(\frac{-6613 \pm 40 \text{ cal/g atom}}{RT}\right), \text{ in } \text{cm}^2/\text{sec}, \quad (8a)$$

$$S = 1.28 \times 10^{17} \exp\left(-\frac{-1174 \pm 120 \text{ cal/g atom}}{RT}\right), \text{ in } \frac{\text{atoms}}{\text{cc-atm}}. \quad (8b)$$

Table I. Glass compositions.

Glass type	Mole fraction: glass former ($SiO_2 + B_2O_3 + P_2O_5$)	glass modifier ($Na_2O + Li_2O + K_2O$)	PbO	other Oxides	Reference
Fused silica[a] or fused quartz	1.00	0.00	0.00	0.00	2, 3, 5, 6, 10
Corning 7740[b]	0.94	0.05	0.00	0.01	2, 4, 6, 8
Corning 7720	0.93	0.04	0.02	0.01	6
Corning 7056	0.90	0.08	0.00	0.02	6
Corning 8160	0.74	0.12	0.08	0.06	6

[a] Vycor (7900) ($\approx 3\% B_2O_3$) $\approx$ 99% glass former + 1% other oxides.

[b] 7740 = Pyrex.

Table II. Diffusion coefficients and solubility coefficients for He in glass.

Glass type	T(°K)	D (cm^2/sec) ($\times 10^7$)	S (atoms per cc) ($\times 10^{-17}$)	K (atoms per cm-sec-atm) ($\times 10^{-11}$)	Ref.
Fused silica	1307	610	1.935	118	
	1134	416 408	2.09	86.1	
	990	250 248	2.52	62.8	
	978	245	2.28	55.8	
	765	94.5	2.89	27.3	
	763	90.2	2.46	22.2	
	653	48.1	3.18	15.3	3
	557	19.5	3.55	6.92	
	464	7.28	4.12	3.00	
	421	3.73	4.72	1.76	
	385	2.15	4.625	0.995	
	351	1.06	5.02	0.532	
	297	0.239	6.32	0.151	
(Amersil)	743			30.7	
	586			13.1	
	448			3.5	6
	442			3.1	
	298			0.24	
	298			0.24	
(GE)	758			34.7	
	606			13.0	6
	434			2.7	
	298			0.20	
Corning Vycor (7900)	728			2.17	
	723			1.85	
	673			1.28	
	573			0.608	5[a]
	473			0.235	
	373	12.6	2.53	0.0415	
	299	0.61	1.21	0.0968	
7740	765	140.0	1.24	17.3	6[a]
	583	38.0	1.02	3.9	6
	472	5.4	2.26	0.12	
7740	579	15.8	Av. sol. coeff. = 1.75; std. dev. = ±58%		4[a]
	503	6.99			
	477	4.52			
	405	1.41			
	360	0.463			
	300	0.0774			
	626	21.0	Av. sol. coeff. = 2.13; std. dev. = ±48%		4[b]
	533	9.1			
	423	1.9			
	422	1.8			
	356	0.44			
	356	0.44			
7740	296.3	0.0726	1.40	0.0101	8[a]
7720	665	22.0	2.69	5.91	6[a]
	382	0.68	2.3	0.156	
7056	675	17.0	1.59	2.7	6[a]
	388	0.31	1.05	0.32	
8160	642	5.6	0.59	0.33	6[a]
	615	4.2	0.46	0.19	

[a] Early-time approximation of D.

[b] Late-time approximation of D.

Table III. Diffusion coefficients and solubility coefficients for Ne in glass (Ne_{20})

Glass type	T(°K)	D (cm^2/sec) ($\times 10^7$)	S (atoms per cc) ($\times 10^{-17}$)	K (atoms per cm-sec-atm) ($\times 10^{-11}$)	Ref.
Fused silica (GE Type 204)	1257	21.3	1.178	2.51	10[a]
	1255	25.7	1.058	2.72	
	1233	22.0	1.323	2.91	
	1182	17.3	1.284	2.22	
	1182	17.2	1.290	2.22	
	1113	13.5	1.26	1.70	
	1111	12.4	1.52	1.89	
	1109	12.9	1.52	1.96	
	1105	12.0	1.59	1.91	
	1103	12.5	1.424	1.78	
	961	5.89	1.47	0.868	
	910	4.33	1.56	0.677	
	908	7.30	1.425	1.04	
	896	3.62	1.75	0.633	
	894	3.70	1.54	0.568	
	893	3.54	1.62	0.575	
	828	2.16	1.93	0.417	
	803	3.71	1.676	0.607	
	713	0.73	2.32	0.169	
Vycor (7900)	673			0.0129	5[a]
	673			0.0135	
	673			0.0129	
	723	0.60	1.61	0.0242	
	723			0.0242	

[a] Decay method for D.

[b] Early-time approximation of D.

Table IV. Diffusion and solubility coefficient for He permeation through Si and Ge.[11]

Single crystal	Temperature range (°K)	D (cm²/sec)	S (atoms/cm³ - sec-atm)
Si	1240 - 1480	$D = 0.11 \exp(\frac{-29\times10^3}{RT})$	$S = 6.5\times10^{14} \exp(\frac{-11\times10^3}{RT})$
Ge	1068 - 1145	$D = 6.1\times10^{-3} \exp(\frac{-16\times10^3}{RT})$	$S = 1.4\times10^{15} \exp(\frac{-13\times10^3 \text{ cal/g-mole}}{RT})$

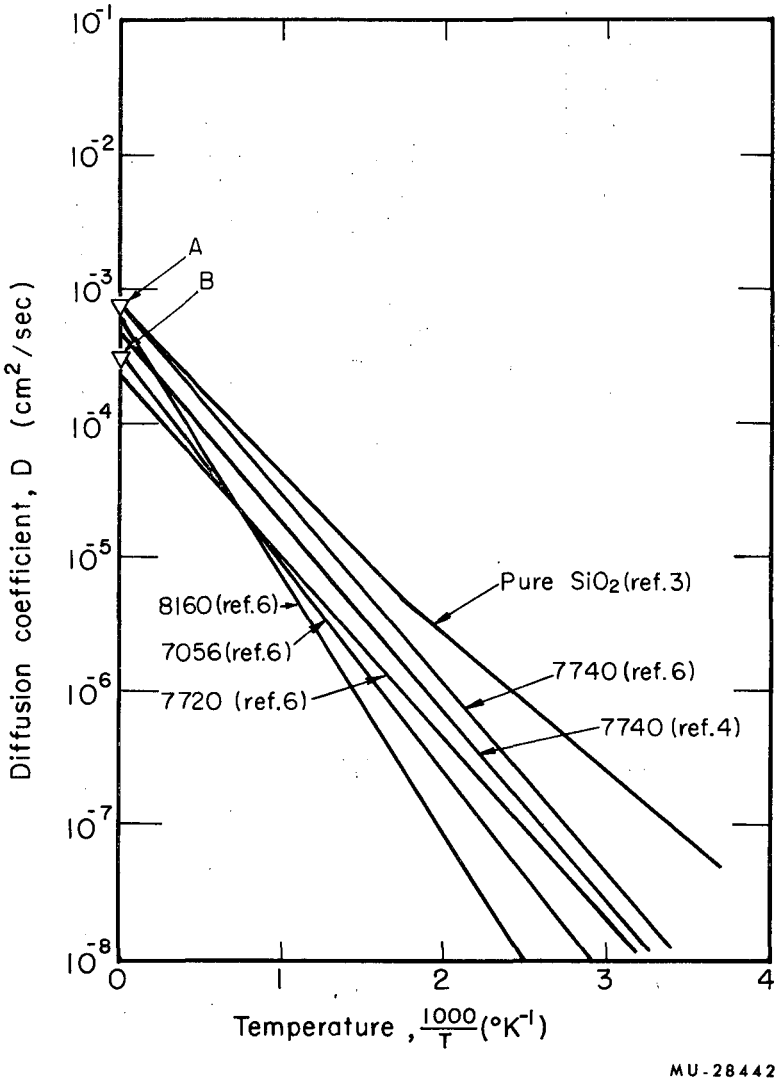

Fig. 3. Diffusion coefficient for helium in glass as a function of (temperature)$^{-1}$.
A. High-temperature D_0, pure SiO_2 (ref.3)
B. Low-temperature D_0, pure SiO_2 (ref.3)

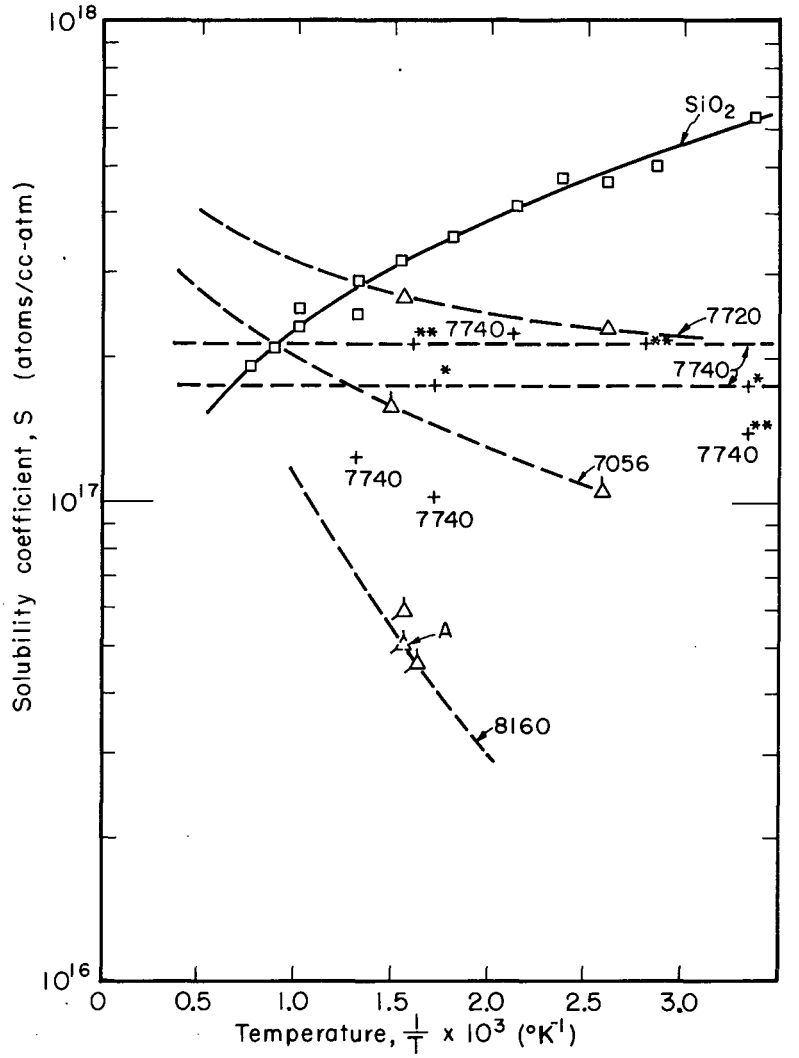

Fig. 4. Solubility coefficient for helium in glass as a function of $(\text{temperature})^{-1}$.

A. Correct value of this point, assuming diffusion coefficients are nearly correct as shown by Fig. 3 and permeability coefficients are as shown by Fig. 5.

* Ref. 4, short-time approximation.

** Ref. 4, late-time approximation on He delay.

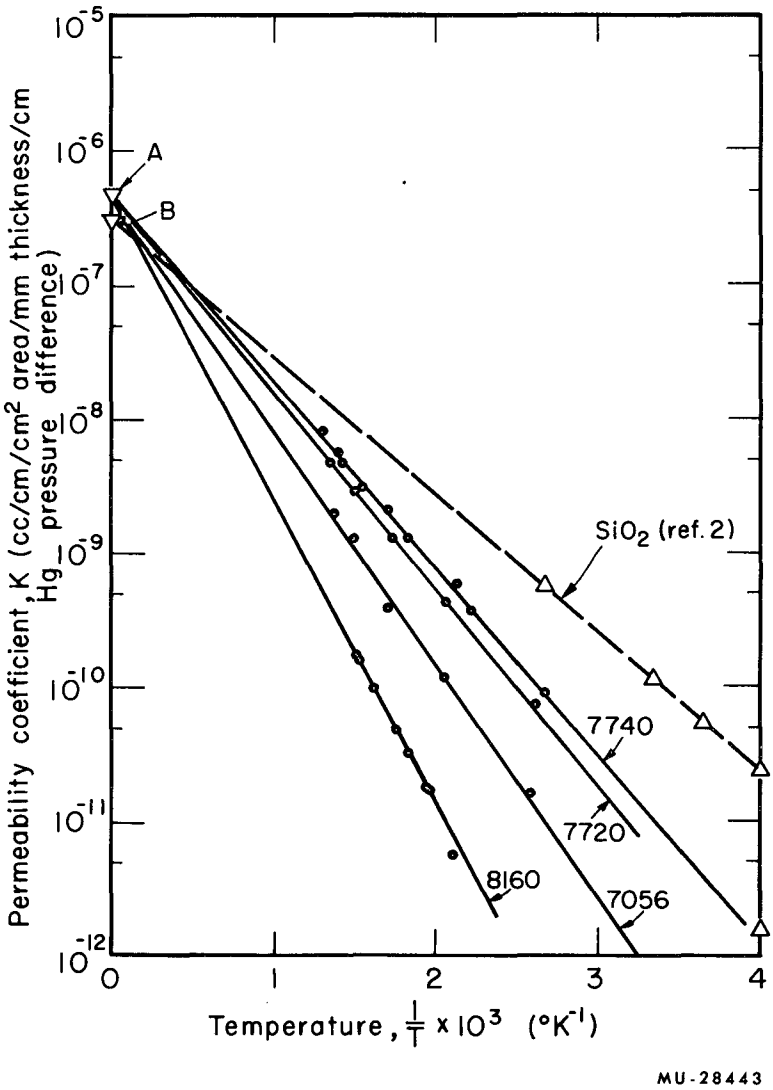

Fig. 5. Permeability coefficient for helium through glass as a function of (temperature)$^{-1}$. (Ref. 6 except where noted.)
A. K_0, high temperature, pure SiO_2 (ref. 3).
B. K_0, low temperature, pure SiO_2 (ref. 3).

For Ne_{20} in fused quartz,[10, 12]

$$T = 440^\circ C \text{ to } 985^\circ C,$$

$$D = 2.21 \times 10^{-4} \exp\left(-\frac{11370 \text{ cal/g atom}}{RT}\right) \text{ in } \frac{cm^2}{sec} , \tag{9a}$$

$$S = 5.59 \times 10^{16} \exp\left(-\frac{-1950 \text{ cal/g atom}}{RT}\right) \text{ in } \frac{\text{atoms}}{\text{cc-atm}} . \tag{9b}$$

Figure 6 is a plot of further permeation data presented by Altemose.[6] Figure 7 is a plot of the activation energies for permeation against mole % glass former as given by Altemose[6] for the glasses of Fig. 6. From the straight line through these values an equation was developed by Altemose for the activation energy for permeation as a function of glass former. A value was also determined for the product,

$$K_0 = S_0 D_0 = 9.8 \times 10^{13}, \text{ in } \frac{\text{atoms}}{\text{cm-sec-atm}} . \tag{10}$$

The activation energy[6] is

$$\Delta H_K = -260\ M + 30.8 \times 10^3, \text{ in cal/g-atom,} \tag{11}$$

and

$$K = 9.8 \times 10^{13} \exp\left(-\frac{-260\ M + 30.8 \times 10^3}{RT}\right), \text{in} \frac{\text{atoms}}{\text{cm-sec-atm}} , \tag{12}$$

where M = mole % glass former. Owing apparently to typographical errors, ΔH_K was given by Altemose[6] as $260\ M + 30 \times 10^3$, but his plot gives $-260\ M + 30.8 \times 10^3$. This latter equation is the one that agrees with his experimental data.

The effects of pressure on the flow rate were investigated by Swets[3, 10] et al. for He and Ne in fused quartz and by McAfee for He in Corning 7740 glass.[8] Urry also investigated the pressure effect on a similar system.[13] Swets et al. find that for He the flow rate through fused silica is proportional to p^x, where $x = 0.95 \pm .02$. McAfee finds that x is greater than 1 for Pyrex (7740). In fact, when the glass membrane is under tension near the breaking stress, x becomes much greater than 1. For compressive stresses x remains 1 for pressures to

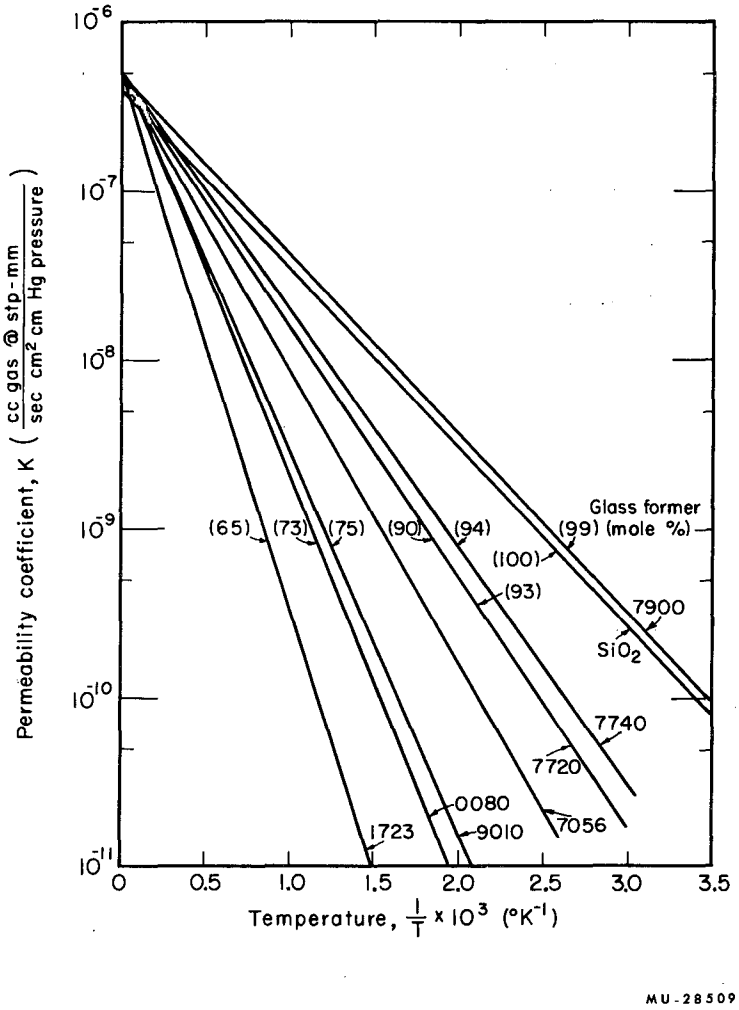

Fig. 6. Permeability coefficient for helium through glass as a function of (temperature)$^{-1}$, illustrating its dependence on glass-former content. (Data from ref. 6.)

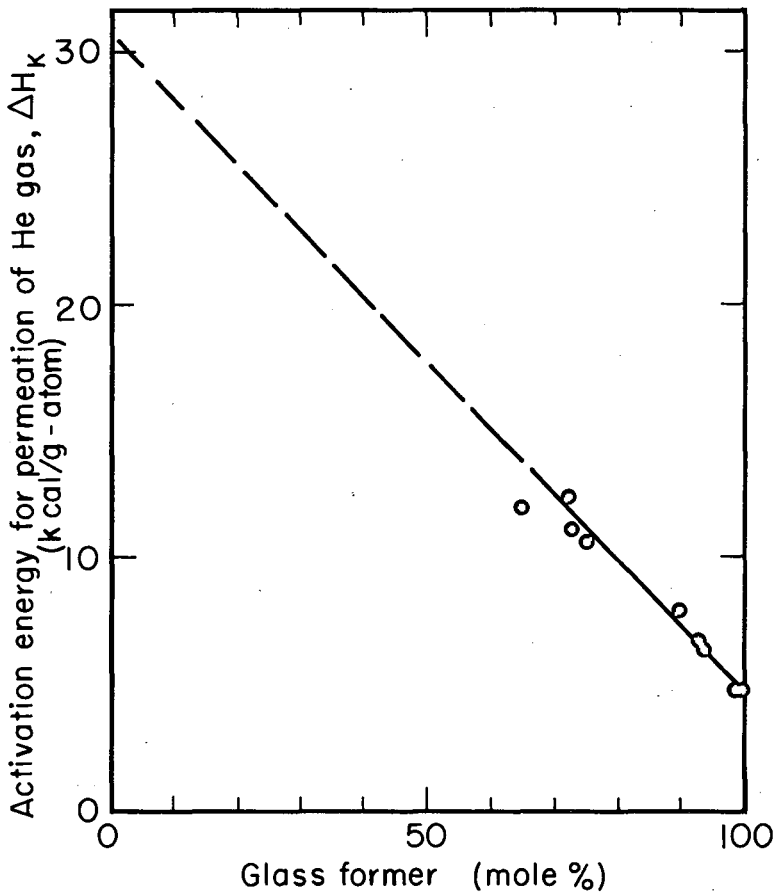

Fig. 7. Activation energies for permeation of helium through glass as a function of mole % of glass former (from ref. 6).

approx 100 psi. Urry, on the other hand, finds $x = 0.88$. Again, Frank et al. find, for Ne, $x \approx 1$ in tension over their pressure range of a few atmospheres.[10]

2. Explanations for Permeation Through Glass

a. Composition-Dependent Explanations

Beginning with work by C. C. Van Voorhis[14] in 1924, a series of investigations[6, 12-19] of the relationship between glass structure and permeability has been carried out. In the former work it was found that increasing the fractional amounts of the "acidic" oxides SiO_2 and B_2O_3 increased the permeability at a given temperature. Increasing amounts of the basic oxides Na_2O, K_2O, BaO, etc. decreased the permeabilities. But the neutral oxides such as PbO and Al_2O_3 had only minor effects on the permeability. The other investigations substantiated the general effect (given above), namely, that glass formers gave high permeabilities, while glass modifiers reduced the permeabilities. Norton in 1953 showed that there was a general smooth relationship between the amount of glass former (SiO_2, P_2O_5, and B_2O_3) by weight and the log of the permeability.[20] Finally, in 1961, Altemose,[6] in an extensive series of glasses ranging from pure fused quartz to approx 56% (by gram molecular weight) glass former, showed that there was a nearly linear correlation between the gram molecular fraction of glass former and the activation energy for permeation. The activation energy was a minimum for pure fused silica and increased linearly with decreasing content of glass former.

The explanation offered by Altemose for this behavior was based on the irregular glass lattice network of SiO_2 tetrahedra proposed by Zachariasen. The glass-forming oxides (network formers) form a network with holes large enough for small gas molecules or atoms to pass through. As glass modifiers are added they plug or block these openings. Since holes are being blocked, Altemose felt that the effective size and number of modifier atoms are important rather than their weight. Because Pb^{+2} and Na^{+1} ions are nearly the same size, they should be equally effective and thus only the numbers of each would be

important in reducing permeation. Altemose[6] therefore considered it more reasonable to plot log permeation rate vs mole percent of glass former than vs weight percent, as discussed by Norton.[20]

b. Structural Explanations

McAfee considered diffusion of gas atoms to proceed along internal surfaces or internal voids.[8] He termed such paths channels, to distinguish this mass transport from true activated-lattice diffusion. This conclusion was based on his experiments with stress-enhanced diffusion in glass. For large tensile stresses greatly increased flow rates were observed, but comparable compressive stresses produced no corresponding decreased flow rates. Because of the sharp dependence of the diffusion constant on elastic deformation of the glass, McAfee considered flow to be along these channels for a considerable portion of its travel. However, he did not completely discount the concept of diffusion as atoms squeezing their way in a random fashion between the ions of the glass lattice, and assumed that this took place for a portion of the diffusion path. His glass model for diffusion under stress thus consisted of randomly oriented submicroscopic flaws or voids separated by narrow necks.

Altemose[6] and Norton[20] both discussed permeation of gas atoms through glass from the point of view of gas atoms passing through an irregular lattice network of SiO_2 tetrahedra. The gas atoms were considered to pass between the ions of the network.

Leiby and Chen[5] (on the basis of their own results), P. W. Bridgman,[21] and others[7, 22-25] considered that the low-temperature permeation rates were much too high for linear dependence on the high-temperature permeation rates on a semilog plot. They concluded that $K \approx BT^{1/2} \exp(-\Delta H_K/RT)$, and felt that the $T^{1/2}$ indicated a molecular streaming process through extremely small voids or channels of molecular cross section. By assuming a distribution of channel sizes they reasoned that the number of channels undergoing molecular streaming would depend on the average energy of the molecules. Therefore, the total streaming rate would depend strongly on the average separation

of wall potentials and on their profile. Thus, both an activation-energy dependence and the $T^{1/2}$ dependence would be found. Leiby and Chen felt that neither pure activated-lattice diffusion alone nor grain-boundary diffusion or molecular streaming alone could explain the experimental behavior.

Swets et al. partially returned to the network theory of glass structure.[3] They pointed out that the activation energy found experimentally should be an average one, since the spaces between ions must vary in size. They also found that two connecting straight lines of different slope on a semilog plot fitted their data better than a $T^{1/2}$ effect. Swets et al. based this conclusion on a least-squares analysis of their experimental data. The connecting point was at approx 300° C. Their justification for the occurrence of such a change in slope was that crystalline forms of silica undergo phase transformations in the temperature range 160° to 280° C. Curves of SiO_2 birefringency vs temperature also show inversions in this temperature range. They therefore felt that some of these characteristics may be carried over into the glassy state. Swets et al. pointed out[3] that the Zachariasen concept of a glass network is partially invalidated by the experiments of Westman and Crowther[26] and Prebus and Michener.[27] These experiments indicated that instead of a completely random network the glass may consist of ordered regions of relatively uniform structure. This view of glass structure is similar to the small-crystallite model for glass proposed by Lebedev.[28]

In their discussion of neon isotope diffusion in fused quartz these same authors suggested that the transition-state diffusion theory of Wert and Zener[29, 30] might be applied to diffusion of gases through fused quartz. No calculations were made, but the concept of a negative entropy of activation for diffusion was considered. Such a negative entropy arises from the fact that the temperature coefficient of the shear modulus of quartz is positive. The implication is that the lattice becomes more rigid with increasing temperature.

Two explanations for this increase in rigidity were offered by Babcock, Barber, and Fajans[31] and by Anderson and Bömmel.[32] The

first explanation was that the fused quartz lattice consists of two co-existing structures. One predominates at high temperatures and the other predominates at low temperatures. The high-temperature structure is more rigid than the low-temperature one. The increasing rigidity with temperature is thus an apparent increase and not an actual one, and is actually a manifestation of the change from the low-temperature structure to the high-temperature one. The second explanation assumed that the transition from the short-range order of the silica tetrahedra to the long-range disorder of the lattice requires slight warping of the Si-O bonds. The oxygen atoms may then have two equilibrium positions between which they can oscillate. As the temperature increases the frequency of oscillation increases and the lattice becomes more rigid. Low-temperature internal friction experiments tend to support such an explanation for the increased lattice rigidity with rising temperature.[32]

In summary, the theories so far advanced to explain the mechanism of gaseous flow through silica have been almost entirely qualitative in nature and have considered only the possible diffusion mechanisms. They are generally based on Zachariasen's[33] and Warren's[34] network theory of glass structure, or on the assumption of pores and channels[35] within the glass, or on a combination of these two ideas. Network modifiers enter the network randomly to block holes and thus reduce the number of available flow channels. Use of Zener and Wert's diffusion-mechanism theory has been suggested but no calculations performed. No one has considered a theoretical interpretation of the solubility coefficient as an aid to understanding the flow of gases through glass membranes.

3. Permeation Through Silicon and Germanium

Reiss and Fuller considered the flow of He and atomic hydrogen to be by interstitial movement of the atoms from one tetrahedral site to another.[36] They applied the Wert-Zener theory for the duffusion coefficient to the experimental data of reference 11. Their results for D_0 are given in Table V along with the experimental values. The close

Table V. Calculated and experimental diffusion coefficient. Pre-exponential term for H in Si, and He in Si and in Ge (ref. 36).

	D_0, calc. (cm^2/sec)	D_0, exp (cm^2/sec)
H in Si	4.1×10^{-3}	9.4×10^{-3}
He in Si	0.26×10^{-1}	1.1×10^{-1}
He in Ge	4.7×10^{-3}	6.1×10^{-3}

agreement between their calculated values and the experimental ones lends support to their conclusions that these gas atoms occupy tetrahedral interstitial sites and diffuse interstitially.

Swalin calculated the activation energy for diffusion of H, He, and Li^+ in Si and Ge.[37] He rejected calculation of ΔH_D from classical strain hypotheses by pointing out that the minimum radius for a hard sphere to pass through the saddle point is significantly larger than the radii of helium or hydrogen atoms. Thus there should be no geometric barrier such as assumed by Anderson et al. in his calculation of ΔH_D for diffusion of various ions and atoms in glass.[38] Atomic polarizability does not seem to be a determining factor, according to Swalin, as he could find no consistent relationship between ΔH_D and polarizability. However, Coulombic interactions between gas atoms and the host lattice atoms did give calculated values for ΔH_D that agree relatively well with empirical ones. For Coulombic interactions ΔH_D was given by[37]

$$\Delta H_D = \frac{Z_i Z_{sq}^2}{D} \sum_j^{\infty} \left(\frac{1}{dij'} - \frac{1}{dij} \right) , \qquad (13)$$

where Z_i = effective valence of the gas atom,

Z_s = effective valence of the solvent ion,

dij = distance between solvent ion j and gas atom i in interstitial site,

dij' = distance dij when gas atom is at saddle point,

D = macroscopic dielectric constant,

q = electronic charge.

Swalin's results are given in Table VI along with the calculated ones. Values for the dielectric constant D were given as 16 and 12 for germanium and silicon, respectively. Z_i and Z_s were calculated by considering the electrons in the valence orbitals to have a nucleus-screening coefficient of 0.4 and the deeper-lying ones to have 1.0. Thus Si and Ge, with four valence electrons, have $Z_s = 2.4$, and He, with two valence electrons, has $Z_i = 1.2$. Atomic hydrogen has 0.6. Since his calculated values agreed relatively well with the experimental ones, Swalin considered Coulombic repulsion the predominant force in determining the activation energy for diffusion.

C. Proposed Theory

In Section II-A, the permeability coefficient was identified as the product of two other, more fundamental, coefficients. These are diffusion and solubility. This implies that two different physical processes essentially determine the magnitude and temperature dependence of the permeability coefficient, K. The first-mentioned process, diffusion, pertains to the passage of gas atoms through the glass or crystalline matrix. It depends on the mechanism of gas-atom transport from one position in the matrix to another. The second-mentioned process, solution, pertains to the connection between the gas-atom concentration in the glass (or crystalline) matrix and in the adjoining gas phase. It depends on the size and number of solution sites as well as upon the number of filled sites.

The permeability coefficient, K, may be written as

$$\begin{aligned} K &= K_0 \exp(-\Delta H_K/RT) \\ &= DS \\ &= D_0 \exp(-\Delta H_D/RT)\, S_0 \exp(-\Delta H_S/RT). \end{aligned} \tag{14}$$

Table VI. Experimental and calculated activation energies for diffusion of H, Li^+ and He atoms through Ge and Si (ref. 37).

	Germanium			Silicon		
Gas atom	ΔH_Dexp	ref	ΔH_Dcalc	ΔH_Dexp	ref	ΔH_Dcalc
H	8.7	39	7.6	11.0	11	10.5
Li^+	11.8	40	12.6	15.1	41	17.5
He	16.0	11	15.2	29.0	11	21.0

Table VII. Calculated and actual number of solution sites, μ_S, in Ge and Si.

	μ_S (calculated) from Eq. (36)	μ_S (calculated) assuming tetrahedral solution sites
Si	2.7×10^{22} $\frac{\text{sites}}{\text{cc}}$	5×10^{22} $\frac{\text{sites}}{\text{cc}}$
Ge	1.5×10^{23} $\frac{\text{sites}}{\text{cc}}$	4.4×10^{22} $\frac{\text{sites}}{\text{cc}}$

In Part 1 below a theory for the solubility coefficient $S = S_0 \exp(-\Delta H_S/RT)$ is developed that is valid for solution of gas atoms in both crystals and glass. In Part 2 the Wert-Zener theory for D_0 is presented. In Part 3 a theory for the activation energy for diffusion and the enthalpy for solution of solute atoms with three degrees of vibration only are developed. The equations developed or presented in the three parts are in principle valid for permeation of gases through glass and crystalline solids.

1. Solubility Coefficient

The concepts upon which development of an equation for the solubility coefficient are based are drawn largely from theory developed to explain gas adsorption in porous materials. The solubility constant is

$$S = S_0 \exp(-\Delta H_S/RT). \qquad (6)$$

From Appendix I we see that S_0 may be expressed as the concentration of gas atoms dissolved in the solid, C, and the entropy change accompanying the solution process. Thus,

$$S = C \exp(\Delta S_S/R) \exp(-\Delta H_S/RT). \qquad (15)$$

In Appendix I are presented the mathematical details of this development. What is presented here is a summary and explanation of the equations. Expressions may be written for ΔS_S and ΔH_S that vary according to the model proposed for the state of the gas atom dissolved in the solid. Each model gives a different temperature dependence to S. By comparing the predicted shape with the experimental shape the correct model or models may be selected.

Consider ΔS_S first. ΔS_S is the change in entropy between the state of the atom in the gas and in the solid, and can be written as

$$\Delta S_S = -S_{tr} + \overline{S}_c + \overline{S}_{th} \quad \text{for a monatomic gas,} \qquad (16)$$

where S_{tr} = total translational entropy of gas atom in gas state,

$\overline{S}_c$ = partial molal configurational entropy due

to gas atoms dissolving randomly on possible sites,

$\overline{S}_{th}$ = thermal entropy of gas atoms in the dissolved state.

S_{tr} may be expressed by the Sackur-Tetrode equation as[42]

$$S_{tr} = R\,(\ell n[(V/N)e(2\pi mkT/h^2)^{3/2}] + 3/2), \qquad (17)$$

where V = volume enclosing N atoms,

m = atomic mass of atom,

c = Boltzmann constant,

T = absolute temperature,

h = Planck's constant.

If we consider all the solution sites to be essentially identical to one another, we can calculate $\overline{S}_c$ by means of the usual mixing equation,[43]

$$\overline{S}_c = \frac{\partial S_c}{\partial n_g'} + R\,\ell n\left(\frac{n_S - n_g}{n_g}\right), \qquad (18)$$

where S_c = total entropy of mixing,

n_S = number of sites,

n_g = number of gas atoms dissolved,

n_g' = moles of gas atoms.

The thermal entropy of the dissolved gas atom depends on the number and kind of degrees of freedom it has in the solid. For each vibrational degree of freedom[43,44] we have

$$\overline{S}_{th} = R\,\{\mu/(\exp(\mu)-1) - \ell n[1-\exp(-\mu)]\}, \qquad (19)$$

where $\mu = h\gamma/kT$,

γ = vibrational frequency for a quantized harmonic oscillator.

This assumes, of course, that the vibration can be described by the harmonic oscillator model.

The dissolved gas atoms, however, may also retain translational degrees of freedom.[43,44] For an ideal two-dimensional gas the entropy is

$$S_{tr} = R\,(\ell n(A_S/N)e(2\pi mkT/h^2)^{2/2} + 2/2), \qquad (20)$$

where A_S = area containing N gas atoms,

N = number of gas atoms contained in area A_S.

The remaining terms are the same as for the three-dimensional gas. Again, for an ideal one-dimensional gas, the entropy becomes

$$S_{tr} = R\,(\ell n(L/N)e(2\pi mkT/h^2)^{1/2} + 1/2) \quad , \qquad (21)$$

where the remaining terms are as described for the three-dimensional case.

The actual entropy term is a combination of these expressions, depending on how many degrees of freedom of translation and vibration are assumed.

ΔH_S is now treated in like manner. Its value is

$$\Delta H_S = \bar{H}_S - H_g, \qquad (22)$$

where $\bar{H}_S$ = partial molal enthalpy in the dissolved state for the gas atom,

H_g = enthalpy in the gas state for the gas atom.

For a perfect monatomic gas,

$$H_g = (3/2)RT + RT = (5/2)\,RT. \qquad (23)$$

H_S varies according to the type and kind of degree of freedom of the gas atom in the dissolved state. For a harmonic oscillator, we have, per degree of freedom,[42]

$$\bar{H}_S \approx E = n[(1/2)h\gamma + h\gamma/\exp(h\gamma/kT) - 1], \qquad (24)$$

where n = number of oscillators, and the other values are as above. The translational protion of the enthalpy is

$$\bar{H}_S \approx x\,(1/2)\,RT + PV\text{term}, \tag{25}$$

where x = number of translational degrees of freedom. Substitution of these equations for the entropy and enthalpy changes allows calculation of what the solubility coefficient should be for each combination of translation and vibration.

Equations for the solubility constant are derived in Appendix I for four different models of the state of the dissolved gas atom. These models are:

1. Dissolved gas atom has three degrees of vibration.
2. Dissolved gas atom has two degrees of vibration plus one degree of translation.
3. Dissolved gas atom has one degree of vibration plus two degrees of translation.
4. Dissolved gas atom has three degrees of translation and no degrees of vibration.

The equations for the solubility coefficient for these models are:

1. Three degrees vibration:

$$S = \frac{n_g}{n_1 p} = \frac{T^{-5/2} P_0}{k(2mk/h^2)^{3/2}} \left[\frac{\exp(h\gamma/2kT)}{\exp(h\gamma/kT)-1}\right]^3 \left(\frac{n_S - n_g}{n_1}\right), \text{ in } \frac{\text{cc(STP)gas}}{\text{cc solid-atm}} \tag{26a}$$

$$\text{or } n_g = P(n_S - n_g)\,\frac{P_0\,T^{-5/2}}{k(2\pi mk/h^2)^{3/2}} \left[\frac{\exp(h\gamma/2kT)}{\exp(h\gamma/kT)-1}\right]^3, \text{ in } \frac{\text{gas atoms}}{\text{cc solid}} \tag{26b}$$

2. Two degrees vibration plus one degree translation:

$$S = \frac{n_g}{n_1 P} = \left(\frac{n_S - n_g}{n_1}\right)\left(\frac{L_S}{N}\right) \frac{T^{-2} P_0}{k(2\pi mk/h^2)} \left[\frac{\exp(h\gamma/2kT)}{\exp(h\gamma/kT)-1}\right]^2, \text{ in } \frac{\text{cc gas (STP)}}{\text{cc solid-atm}} \tag{27a}$$

$$\text{or } n_g = P(n_S - n_g)\,\frac{L_S}{N}\,\frac{P_0\,T^{-2}}{k(2\pi mk/h^2)} \left[\frac{\exp(h\gamma/2kT}{\exp(h\gamma/kT)-1}\right]^2 \frac{\text{gas atoms}}{\text{cc solid}} \tag{27b}$$

3. One degree vibration plus two degrees translation:

$$S = \frac{n_g}{n_1 P} = \left(\frac{n_S - n_g}{n_1}\right)\left(\frac{A_S}{N}\right) \frac{P_0 T^{-3/2}}{k(2\pi mk/h^2)^{1/2}} \left[\frac{\exp(h\gamma/2kT}{\exp(h\gamma/kT)-1}\right] \tag{28a}$$

$$\text{or } n_g = P(n_S - n_g)\left(\frac{A_S}{N}\right) \frac{P_0 T^{-3/2}}{k(2\pi mk/h)^{1/2}} \left[\frac{\exp(h\gamma/2kT}{\exp(h\gamma/kT)-1}\right]. \tag{28b}$$

4. Three degrees translation plus no degree vibration:

$$S = \frac{n_g}{n_1 P} = \left(\frac{n_S - n_g}{n_1}\right)\left(\frac{V_S}{N}\right)\left(\frac{1}{kT}\right) P_0 \tag{29a}$$

$$\text{or } n_g = P(n_S - n_g)\left(\frac{V_S}{N}\right)\left(\frac{P_0}{k}\right)\left(T^{-1}\right). \tag{29b}$$

2. Pre-exponential Term, D_0, of Diffusion Coefficient

Wert and Zener[29, 30, 36, 45] have developed a theoretical equation for D_0:

$$D_0 = g\lambda^2 \sqrt{\Delta H_D/2Nm\lambda^2} \exp\left(-\Delta H_D \frac{\partial G}{\partial T}/G_0 R\right), \tag{30}$$

where $\frac{\partial G}{\partial T}$ = temperature dependence of modulus of rigidity,

G_0 = modulus of rigidity at 0° K (extrapolated value),

N = Avogadro's number,

m = mass of diffusing atom,

λ = mean distance between jump sites,

g = 1/6 × number of paths leading out of an interstice $\times\left(\frac{\text{net distance moved in diffusion direction per jump}}{\text{distance between jump sites}}\right)^2$

This equation is unique in its general accuracy for interstitial diffusion in semiconductors and metals.[46]

To apply this equation to glass requires assumption of values for λ and g, since all other factors are known or directly determinable. These values are determined by the location of the diffusion atoms in the crystalline lattice.

3. Prediction of Activation Energy for Diffusion and Solution in Silicon and Germanium

If Eq. (24) in Section II-B-2 given by Swalin[37] for the activation energy for diffusion is correct, the activation energy for solution should be closely related to this same Coulombic interaction. The enthalpy of a gas atom with three vibrational degrees of freedom in an interstitial site should be the negative term in Eq. (24). From this value the net change in enthalpy on solution of the gas atom in the interstitial site may be calculated and finally the overall activation energy for permeation determined.

Calculation of H_S by

$$H_S = \frac{Z_i Z_j q^2}{D_{d_0}} \sum_{j}^{\infty} \frac{1}{dij} \quad , \tag{31}$$

where the symbols have the same meaning as in Eq. (24), and with Swalin's values used for the constants, gives H_S = approx 273×10^3 cal/g atom for Ge. Subtraction of the enthalpy for gas atoms in the gaseous state gives values for ΔH_S that are an order of magnitude too large. Therefore, some other repulsive force must be responsible for energies of diffusion and solution. The agreement between calculated and experimental values found by Swalin must be fortuitous.

Consider the repulsive interaction between atoms and ions. Seitz[47] gives Born and Mayer's repulsive term between ions as

$$\epsilon = ae^{-r/\rho} \quad , \tag{32}$$

where ϵ = repulsive energy between a pair of ions or atoms,

a = constant $= b\left(1+\frac{Z_i}{n_i}\,\frac{Z_j}{n_j}\right)\exp\left[(r_i+r_j)/\rho\right]$,

r = distance between ions,

ρ = constant $= 0.345\times 10^{-8}$ cm,

Z_i = valence of ion i,

Z_j = valence of ion j,

n_i = number of valence electrons in outer shells of ions i,

n_j = number of valence electrons in outer shells of ions j,

r_i, r_j = ionic radii of ions i and j, respectively.

If we consider $e^{(r_i+r_j)/\rho}$ a constant and part of b, and assume

Z_i = number of electrons in the outer filled or partially filled shell of solvent atom,

Z_j = number of electrons in the outer filled or partially filled shell of diffusing atom or ion,

n_i, n_j = possible number of electrons in the outer shells of the solvent and diffusing atoms (8 or 2),

then

$$\Delta H_D = A_0 b\left(1+\frac{Z_i}{n_i}+\frac{Z_j}{n_j}\right)\sum_{n=1}^{2}\left[\exp(-r_n/\rho)\right]-\sum_{m=1}^{2}\left[\exp(-r_m/\rho)\right]; \quad (33)$$

$$H_S \text{ is also } H_S = A_0 b\left(1+\frac{Z_i}{n_i}\,\frac{Z_i}{n_j}\right)\sum_{m=1}^{2}\left[\exp(-r_m/\rho)\right]. \quad (34)$$

The summations refer to the summation of repulsive forces about the diffusing atom at the saddle point, n, and the interstitial point, m. A_0 is Avogadro's number. Instead of summing over the nearest 55 neighbors as in Swalin's treatment, one need here consider only the first two nearest neighbors, as the atoms farther away make no significant contribution. For Si and Ge the constant b may be evaluated

by determining it from ΔH_D for one gaseous element in Si or Ge and then using this value in all subsequent calculations.

D. Application of Proposed Theory to Analysis of Experimental Data

1. Glass

a. Solubility Coefficient

To determine the two unknowns, γ and n_S, in the derived solubility equations for fused silica, it is necessary to use both the solubility data for He in fused quartz[3] and for Ne in fused quartz.[10] Figure 8 is a plot of solubility vs 1/T for these two gases in fused silica. although Swets et al. fitted their data for Ne by $S = S_0 \exp(-\Delta H_S/RT)$, it can be fitted equally well by a curve of slope T^{-1}. Such a curve corresponds to the Ne atom's retaining three translational degrees of freedom. The slope of the curve for He, on the other hand, is not constant and is less negative than for Ne. This means that the He atoms must have less than three translational degrees of freedom. It is apparent from Fig. 8, however, that the curve plotted for a dissolved atom having one degree of vibrational and two degrees of translational freedom does not have a steep enough slope even though its general shape is correct. Therefore the state of He atoms dissolved in fused quartz is a mixture of the two states. One state is the dissolved atom with one degree of vibration and two of translation. The other state is the dissolved atom with three degrees of translation. To calculate γ, n_S, and the volume per site from the data for He and Ne, it is necessary to assume first

$$n_{S_{He}} \approx n_{S_{Ne}},$$

and assume second

$$S_{total} = (x)S_{(1\ vib + 2\ tr)} + S_{(3\ tr)}(1-x).$$

That is, the total solubility curve can be represented by a combination of the solubility curves for the two pure states. By extrapolating the curves for He[4] and Ne[20] back to the point where they cross, the highest temperature is found at which all the dissolved He atoms can exist with

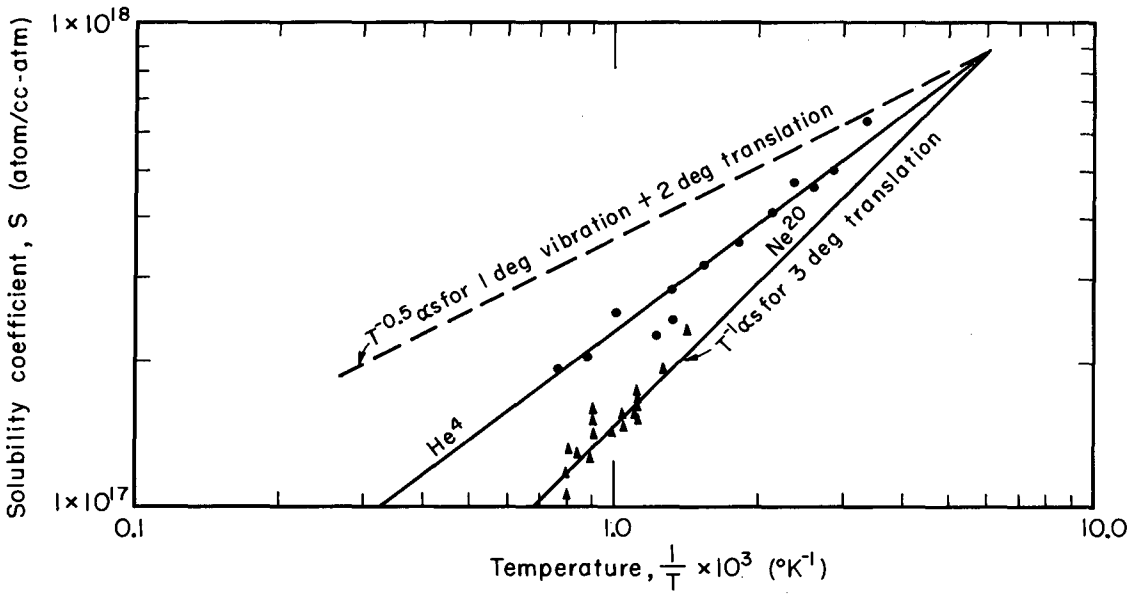

Fig. 8. Solubility coefficient for helium and neon-20 in fused quartz as a function of (temperature)$^{-1}$.

one degree of vibration and two degrees of translation. This is a result of the second assumption. The temperature is 167° K. Using Eq. (29) for three degrees of translation and this temperature gives

$$(n_S - n_g)\ \frac{V_S}{N} = 2\times10^{-2} \text{ cc site space per cc glass volume.}$$

For a minimum size of site, such as in Fig. 9, $(n_S - n_g) \approx 4\times10^{20}$ holes/cc. As $n_g \sim 10^{17}$, n_S is 4×10^{20} holes /cc. Larger holes would of necessity reduce this number. It is interesting to note that there are on the order of 10^{22} SiO_2 molecules per cc of glass. This means that at most there is only 1 hole for approximately 25.0 SiO_2 molecules in fused silica.

Substitution of this n_S value into Eq. (28) for one degree of vibration + two degrees of translation allows calculation of γ, the vibration frequency. This frequency for He in fused silica is $\gamma \approx 7\times10^{11}\text{sec}^{-1}$. Such a frequency is in keeping with a hole that is large in comparison with the He atom (approx 2 Å in diameter), and is of the order found for He atoms adsorbed on graphite.[44,48]

Solution of He in the remaining glasses under consideration may now be explained. Figure 10 is a semilog plot of the proposed solubility equations for $\gamma = 1\times10^{12}\ \text{sec}^{-1}$ and $n_S = 4\times10^{20}$ sites/cc. We see that there is a very dramatic change in the slope of the solubility curves. The slope changes from a positive one for three degrees of translation to less positive slope for transformation of one degree of translation to vibration. On transformation of two degrees of translation to vibration and retention of one degree of translation, the slope becomes 0. Finally, on transformation of all three degrees of translation to vibration, the slope is negative.

If we compare this behavior with the behavior of the solubility curves of Fig. 4, we find the same phenomena. As more and more glass modifier is added to SiO_2, the slopes change from positive through 0 to negative. The proposed theory thus appears to predict this experimentally observed behavior.

From the curves in Fig. 4 it is apparent that the slopes become progressively more negative with increasing glass-modifier content.

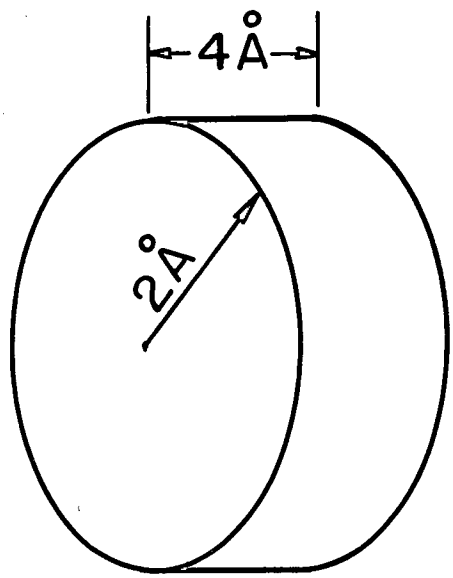

MU-28445

Fig. 9. Model of gas-atom solute site for fused SiO_2.

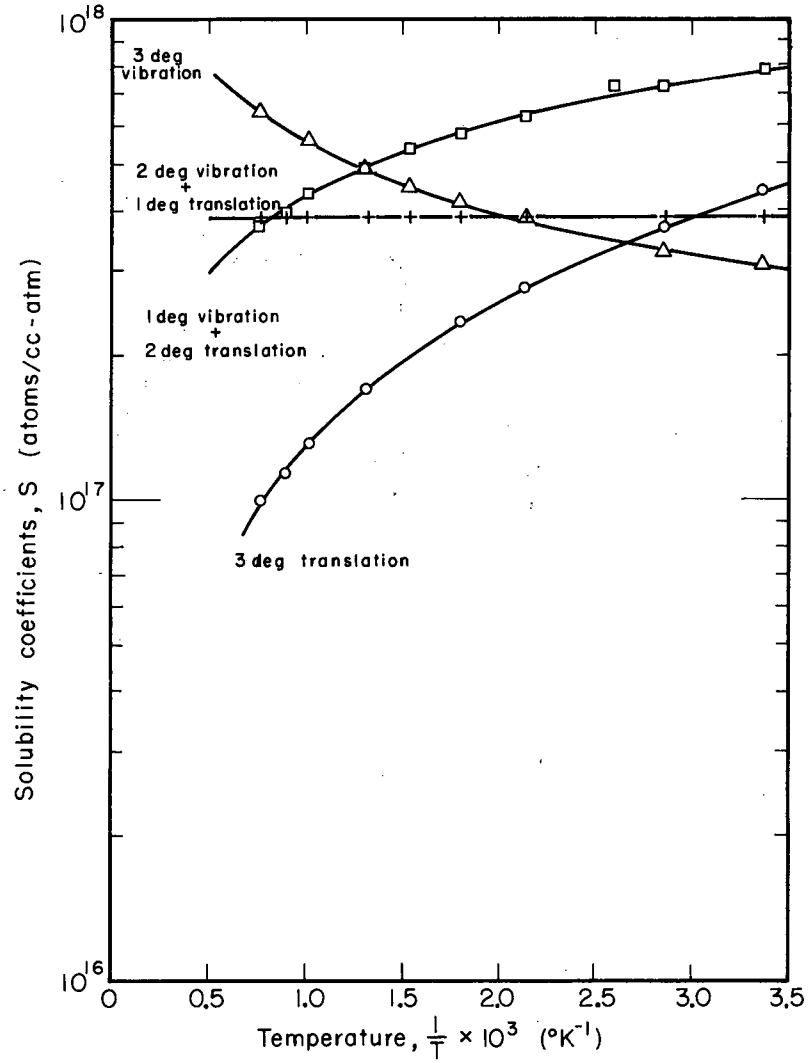

Fig. 10. Calculated solubility coefficients for monatomic cases in glass as a function of (temperature)$^{-1}$ for 4×10^{20} gas-atom solution sites per cc glass; 1×10^{12} sec^{-1} vibration frequency.

Again this may be explained by an increase in the vibration frequency γ from a minimum value of approx 7×10^{11} sec^{-1} in fused quartz to values greater than 10^{13} sec^{-1}. Table VIII lists the vibration frequencies for SiO_2, 7740, 7720, 7056, 8160, Si, and Ge for the proposed models, calculated from the slopes of the solubility curves of Fig. 4 and the summary data for Si and Ge.

Table VIII. Calculated vibration frequencies and number of vibration degrees of freedom.

Glass type	Degrees of vibratory freedom	Frequency
SiO_2	1	0.7×10^{12} sec^{-1}
7740	2	0.7 to 1×10^{12} sec^{-1}
7720	3	0.1 to 0.7×10^{12} sec^{-1}
7056	3	9×10^{12} sec^{-1}
8160	3	3.3×10^{13} sec^{-1}
Si	3	1×10^{14} sec^{-1}
Ge	3	1.4×10^{14} sec^{-1}

b. Diffusion Coefficient

Complete comparison of the Wert-Zener equation for D_0 with experimental data is limited to fused quartz.

For SiO_2 $\frac{\partial G}{\partial T}/G_0$, λ, and g must be determined. The λ was assumed to be the Si-O bond distance in fused silica of 1.60Å.[34] The average number of equivalent diffusion paths per jump site was taken as four. This value corresponds to a tetrahedral arrangement of jump sites about any one site. For fused silica,[1] $G_0 = 4.3\times10^6$ psi and $\frac{\partial G}{\partial T} = +4.88\times10^2$ psi/°K. A test of this diffusion equation is not only the agreement in experimental and calculated values of D_0 but also whether

or not the calculated and empirical values of ΔS_D agree in sign and are similar in magnitude. Table IX gives the calculated and experimental values for D_0 for SiO_2 and the calculated and empirical values for ΔS_D.

A less complete but nevertheless valuable comparison may be made for the other glasses. Complete calculations are limited by the lack of shear-modulus data for these glasses. However, a comparison was made by using the Wert-Zener formula and determining what the empirical entropy term should be for equivalence of experiment and calculation. Table X is a tabulation of the calculated and empirical values for ΔS_D. The range for all these glasses is from -2 to -4 entropy units. All the entropy values are negative, which suggests that the temperature coefficient of the modulus of rigidity for all the glasses considered here is positive. This is certainly the case for fused silica and some of the other high-silica glasses.[49] Though the data are incomplete it is clear that this equation, as suggested by Swets et al.,[10] adequately applies to glasses as well as crystalline solids for at least diffusion of rare gas atoms.

The effect of glass composition on diffusion may be seen from Fig. 11. A straight line can be drawn without great error through the activation energies for diffusion. The slope of this curve is just one-half the slope of the empirical equation given by Altemose for the permeability activation energy. This means that glass modifiers affect equally the solubility and the diffusion processes in glass.

2. Silicon and Germanium

Application of Eq. (26), for the solubility coefficient for solute gas atoms with three degrees of vibration, to the data of Table IV yields the vibration frequencies given in Table VIII. Calculation of the number of solute sites by using Eq. (26) and these frequencies yields the values given in Table VII. These values are compared in Table VII to the calculated number of tetrahedral interstitial sites in Si and Ge. The agreement is satisfactory.

Table IX. Calculated and experimental D_0 and ΔS_D for helium diffusion in fused silica.

	Temperature range (° C)	Calculated	Experimental	Calculated D_0 / Experimental D_0
D_0	24 to 300	$1.8\times10^{-3}\ \frac{cm^2}{sec}$	$3.04\times10^{-4}\ \frac{cm^2}{sec}$	5.9
	300 to 1034	$2.0\times10^{-3}\ \frac{cm^2}{sec}$	$7.4\times10^{-4}\ \frac{cm^2}{sec}$	2.7
		Calculated	Empirical	Calculated ΔS_D / Empirical ΔS_D
ΔS_D	24 to 300	-0.62 eu	-3.55 eu	0.18
	300 to 1034	-0.74 eu	-1.95 eu	0.38

Table X. Experimental ΔH_K and ΔH_D, calculated ΔS_D, and empirical ΔS_D for helium permeation through several glasses.

Glass	% Glass former	ΔH_K	ΔH_{Dexp}	ΔH_{Sexp}	ΔS_D Calc	ΔS_D Empirical (eu)
SiO_2	100	4900	5580	- 680	-0.62	-3.55
		5439	6613	-1174	-0.74	-1.95
7740	94	6400	6500	- 100		-2.06
7720	93	6770	6200	+ 468		-4.13
7056	90	7930	7240	+ 940		-3.85
8160	74	10500	8780	+1460		-2.66

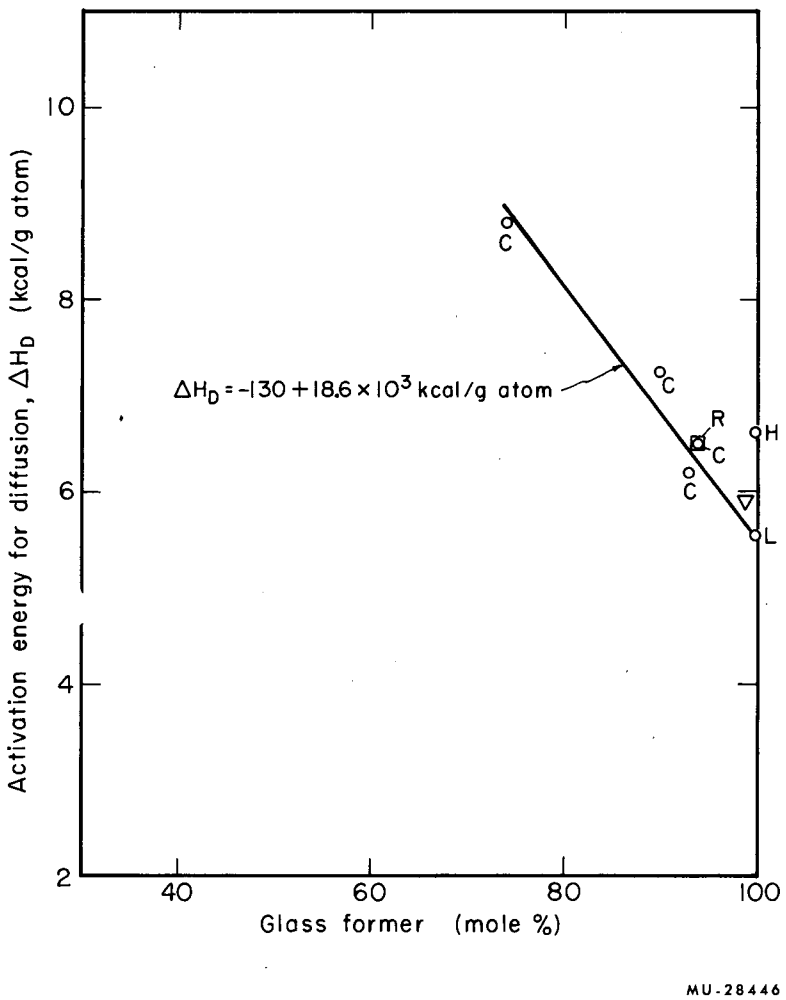

Fig. 11. Activation energy for helium diffusion through glass as a function of mole % glass former.
Oc: calculated from data in Ref. 6
OH, OL: Ref. 3.
□R: Ref. 4.
▽ : Ref. 5.

The theory of Wert-Zener for the diffusion coefficient appears adequate to explain the diffusion coefficients for hydrogen and helium. It is now necessary to determine whether Eq. (33) holds satisfactorily for the activation energies both for diffusion and for solution. To perform such calculations it is necessary to evaluate b; b was determined by setting $\Delta H_{Dexp} = \Delta H_{Dcal}$ for hydrogen monatomic diffusion in germanium. This value of b was then used in all subsequent calculations. The calculated and experimental values are given in Table XI. Values for hydrogen diffusion agree closely with those found experimentally. Helium does not agree as satisfactorily as does hydrogen. The activation energy for diffusion is underestimated, whereas that for solution is overestimated. But their values are of the proper order of magnitude and their sum, the activation energy for permeation, agrees very well with experimental values.

If instead of using the same constant b for He and H, one calculated a new one for He in the same way as b was calculated previously and also considers ρ to change with the kind of diffusing atom, then the activation energies both for diffusion and for solution can be made to agree more closely with the experimental ones. The ρ used for He was taken as the ρ in the repulsive term for repulsive forces between two He atoms.[47] Conclusions that may be drawn from this semi-empirical treatment of activation energies are:

1. Repulsive forces between solvent atoms and solute atoms are the primary contributors to the energies associated with solution and transport of H and He atoms and Li^+ ions in Si and Ge.

2. Coulombic and Van der Waals forces are secondary contributors to the total energies found.

3. Because the electronic state of the constituents is much the same in glass as for Si and Ge, it is probable that repulsive forces between solvent atoms or ions and rare gas atoms also constitute the primary contributor to the permeation energies found for glasses. The influence of glass modifiers may be felt in two ways. The first way would be in narrowing the hole through which the diffusing atoms pass.

Table XI. Calculated and experimental ΔH, $\bar{H}_s$, $\overline{\Delta H}_s$, and ΔH_K for H, Li^+, and He atom permeation through Ge and Si.

	Germanium			Silicon		
Diff. Atom	ΔH_{Dexp}	Ref.	ΔH_{Dcalc}	ΔH_{Dexp}	Ref.	ΔH_{Dcalc}
H	8.7	39	8.7	11.8	11	11.0
Li^+	11.8	40	11	15.1	41	14.7
He	16.0	11	11	29	11	14.7
	$\bar{H}_{sexp}$	Ref.	$\bar{H}_{scalc}$	$\bar{H}_{sexp}$	Ref.	$\bar{H}_{scalc}$
H	[a]17.9	11	17.9	24.3	b	24.5
Li^+				no data available		
He	[a]18.6	11	22.4	[a]18.3	11	30.7
	$\overline{\Delta H}_{sexp}$	Ref.	$\overline{\Delta H}_{scalc}$	$\overline{\Delta H}_{sexp}$	Ref.	$\overline{\Delta H}_{scalc}$
H	12.3	11	12.3	17	c	17.2
Li^+	no data					
He	13	11	16.8	11	11	23.4
	ΔH_{Kexp}	Ref.	ΔH_{Kcalc}	ΔH_{Kexp}	Ref.	ΔH_{Kcalc}
H	21	11	21	28	11	29
Li^+						
He	29	11	27.7	40	11	38.1

[a] $\bar{H}_{sexp} = \overline{\Delta H}_{sexp} + 5/2\ RT$ T = 1200°C for Si; T = 860°C for Ge

[b] $\bar{H}_{sexp} = Q_{exp\ ref.\ 11} - \Delta H_{Dexp\ ref.\ 39} + 5/2\ RT$

Units are kcal/g atom.

a, b, c $\Delta H_{sexp} = Q_{exp\ ref.\ 11} - \Delta H_{Dexp\ ref.\ 39}$.

Note: $\bar{H}_s$ and $\Delta\bar{H}_s$ for hydrogen exclude enthalpy for transformation of H_2 to H.

This would increase the repulsive-energy terms. The second way would be in disturbing the electron distribution about the ions in the glass. This would cause Coulombic interactions to become more important in glasses as the glass-modifier content becomes larger.

E. Glass Structure Based on Solubility-Diffusion Model

The correspondence of the proposed theory of gaseous permeability with available experimental data suggests a model for glass structure that is similar to a polycrystalline one. It is proposed that the glass body consists of groups of silica tetrahedra packed in a dense arrangement separated from other similar groups by grain-like boundary regions. In effect the glass is envisioned as a grouping of crystallites of say five- or sevenfold symmetry[50] connected to other crystallites at tetrahedral corners or connected by bridges of closely matched tetrahedra. The resulting structure may be loosely described as a very fine-grained body. Most of the increase in void volume on going from crystalline silica to fused silica would be concentrated in the formation of these grain-boundary-like regions. The total volume in model void sites is approx 0.02 cc per cc glass volume, or about 2%. The volume increase on transformation from quartz crystal to glass is about 15%; for cristobalite it is only about 2 to 5%. A portion of the discrepancy between the figures is due to the difference between model site shape and real shape. However, a considerable portion of the difference will be in what may be termed closed voids if the suggested structure is indeed correct. In other words, connections between non-repeatable symmetry crystallites may be like Mott islands[51] of good fit with a hole in the island.

Flow will then be along these grain-boundary-like regions and not through the voids in the tetrahedra-composed crystallites. It is reasonable not to expect diffusion through such holes, since He diffusion through quartz crystals is at least 10^{-3} of the flow through fused quartz[15,52] at several hundred degrees centigrade. Also, it is known that the distances between Si^{+4} and $O^{=}$ ions remain nearly the same in

fused quartz as in crystalline quartz. From a geometrical point of view the hole sizes in the various crystalline forms of silica are large enough to accommodate He atoms, yet they do not.

The hole radius–that is, the diameter of the largest hard sphere that can be accommodated in the cyrstalline silica form–is given by R. B. Langston (of the University of California Department of Mineral Technology) as 3.4Å for β-tridymite, 2.6Å for β-cristobalite, and 2.0Å for β-quartz. The hole sizes in Si and Ge are even larger, yet both heat of solution and heat of diffusion are positive and large. Thus the holes available in the glass structure must be significantly larger than those in the crystalline forms even though there is very little change in the interatomic spacings. Since the volume change on fusion is also relatively large, the void increase cannot be distributed uniformly throughout the glass body but must be concentrated in small regions of the body.

Supporting the existence of microscopic voids is the work of P. W. Bridgman,[21] who found that the compressibility of silica increases with increasing pressure up to approx 350 atm, after which it acts like other amorphous structures. Bridgman's explanation for such phenomena was that there were lenticular cavities in SiO_2 which were squeezed flatter and flatter. Ordinary glasses show similar behavior in that permanent density changes amounting to several percent can be produced with pressure.[8] Both Vycor and fused silica were compressed by Bridgman,[21] who found the threshold for permanent compaction was nearly the same. The Si-O bond distances determined by x-ray diffraction on samples of density nearly equal to crystalline quartz (approx 10% increase in glass density) were nearly identical to those for uncompacted glass.

Such a model allows explanation of the "stuffing" of silica with glass modifiers. The modifiers first fill the holes in the islands of good fit and the microscopic voids of the grain-boundary-like region. This filling allows an increase in bulk density with very little change in the Si-O, Si-Si, and O-O distances. It also results in a reduction in size of sites. Eventually there will have to be a break

in the bulk-density curve, as all the voids large enough to accept modifiers will be filled. The density will then follow a more normal curve for physical mixing of two materials. Such behavior is observed in silicate glasses, with the break coming near a void volume limit of 10%.

The change in degrees of freedom may be explained by invoking a Lennard-Jones model of the potential energy between two atoms. Figure 12 shows schematically the change of the potential well shape with decrease in hole size; 12(a) is the Lennard-Jones "6-12" potential well shape; 12(b) is superposition of two 6-12 potentials at a distance such that a gas atom is held on one wall or the other. As the sides contract the hole assumes a more nearly parabolic potential well shape of ever steepening sides, as in Figs. 12(c) and (d). For the harmonic-oscillator model this means an increasing frequency of vibration. For He in glass, 12(b) must be the picture of the cross section of lens-like voids. The plane of the lens would appear much like 12(c). The motion then would be described as translation in two dimensions along the surface of the lens and vibration in one dimension perpendicular to the surface of the lens. If the lens were squeezed into a cylinder by adding glass modifier there would be translation in one dimension along the cylinder axis but vibration in two dimensions perpendicular to the axis. Finally further constriction along the cylinder axis would give vibration in all three directions.

Diffusion in the glass matrix is accomplished by jumping from one to another of these holes. Bulk diffusion equations apply, since the conducting volume is nearly constant independent of composition, "crystallite" regions are nearly impermeable to diffusion compared with the grain-boundary-like boundaries, and the size of the crystallite is limited by symmetry. The potential barrier to diffusion is the potential barrier between solution sites. The effective jump distance is then the distance across this barrier and not the distance between solution sites. As the barrier influences both diffusion and solution, both should be affected in about the same way by glass-modifier content. This again is found to be experimentally correct.

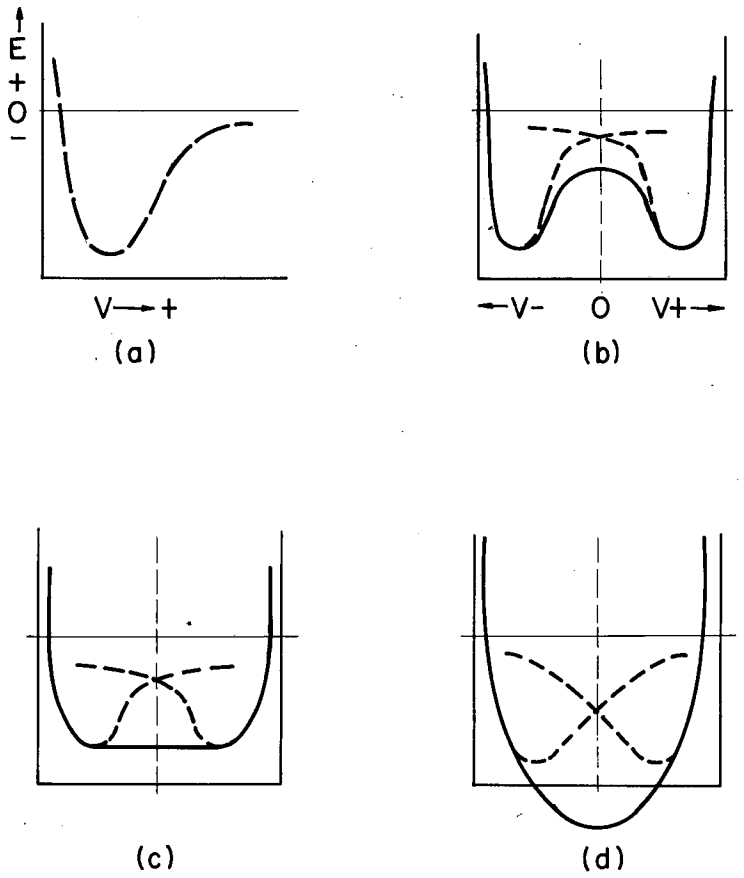

Fig. 12. Schematic representation of potential wells for gas atoms in solution sites for different separation distances of site walls.

In summary, the glass-structure concept that agrees most satisfactorily with gaseous permeability and the previous data concerning bond distances, hole sizes, and glass densities is one that assumes crystallites of nontranslatable symmetry connected to one another by bonding at tetrahedral corners, the volume between crystallites being largely void. The whole collection of crystallites thus makes up a kind of "fine-grained polycrystalline structure" in which the crystallites act as grains and the high-void-volume regions between act as grain boundaries.

III. STRESS-ENHANCED GASEOUS PERMEATION OF Al_2O_3 BODIES

Stress-enhanced gaseous permeation of high-alumina bodies is shown to occur. The dependence of the observed enhanced helium flow rate on loading rate, magnitude of stress, specimen prior history, specimen fabrication, and specimen microstructure are investigated. From this investigation a process is postulated for stress-enhanced gaseous permeation through polycrystalline ceramic bodies.

A. Literature Review

There is no previously published direct experimental evidence of recoverable permeation change with stress for normally impermeable crystalline ceramic materials. Evidence does exist for nonrecoverable change with temperature.[12] A theory has been developed for lattice diffusion that considers the effect of static strains.[53] According to this theory the activation energy for diffusion is reduced for tensile stresses and increased for compressive ones. Girifalco and Grimes show that some experimental data may be explained in this way. However, no usable theory for transient stresses is developed.

Helium permeation through polycrystalline and single-crystal high-purity alumina has been investigated.[54] No studies have been made of the influence of porosity within the alumina body on its permeability characteristics. However, a related study has been made of the relationship between open and closed porosity in BeO by a permeation method.[55] In this study it was found that open porosity disappeared at about 95% of theoretical density. O'Neill et al. also found that the amount of closed porosity remained essentially constant at approx 5% for greater total porosity. Again, these studies were done under stress-free conditions.

B. Experimental Procedure

Effects of stress on gaseous flow through commercial high-alumina bodies were investigated by mechanically inducing in them static and transient stresses. The specimens were manufactured in the form of thin flat disks, 3 in. in diameter and 1/8 in. thick. The loading apparatus was designed so that these specimens were stressed as concentrically loaded fixed-edge rigid diaphragms.

Detection of gaseous flow through the specimens was accomplished by means of a mass spectrometer whose output was continuously recorded. Continuous monitoring of the flow through the specimens allowed observation of any rapid flow changes that might accompany transient stress conditions as well as flow under static stress conditions. Helium gas was used in all the experiments, which were conducted at room temperature.

1. Specimens

a. Composition and Physical Properties

Four commercially prepared high-alumina materials were selected for study. Three of these materials were manufactured by one firm, and the fourth material by a second firm. Pertinent physical properties of these four different high-alumina materials are given in Table XII. The specimens were manufactured in the form of disks 1/8 in. thick by 3 in. in diameter. All these bodies were impermeable to helium under stress-freee conditions.

b. Specimen Preparation

Because these disks were to be tested in the form of a rigid diaphragm, it was necessary to eliminate the effects of the center plane being at "0" stress. This problem was solved by grinding blind holes in the fabricated disks. Three blind-hole arrangements and two grinding methods were used. Figure 13 is a schematic representation of the blind-hole placements. The placements are drawn in chronological order of use. Hole placement was varied to take advantage of various loading methods. The first blind-hole arrangement

Table XII. Physical properties of investigated high-alumina bodies.

Material		No. 1	No. 2	No. 3	No. 4
Bulk density	(g/cc)	3.70	3.76	3.89	3.98
Bulk porosity	(%)	7.2	5.6	2.4	0.3-0.4
Open porosity	(%)	0.00	0.00	0.00	0.00
Flexural strength	(psi)	64,000	46,000	62,000	55,000 min
Al_2O_3 content	(%)	95	97.6	99.5	99.9+
E	(psi)	-	-	-	56.1×10^6
μ	-	-	-	-	0.205

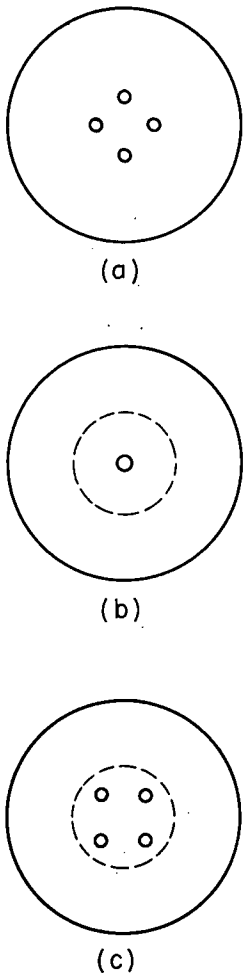

Fig. 13. Schematic indication of locations of blind holes in fabricated specimens, and load distribution.

was used with center-point or ram loading. The last two were used with ring loading. Two hole sizes were used--1/4 in. and 1/8 in. diameter. Membrane thicknesses varied from 0.3 mm to 1 mm.

Ultrasonic impact and diamond drill grinding methods were used to form the blind holes. These two methods were employed to investigate the influence of blind hole preparation on gas flow through the membranes. A second consideration was that the only published data on flow of helium through single-crystal and polycrystalline alumina were for ultrasonic-impact-ground specimens.[54]

c. Microstructure

Metallographic studies were made on all four specimen bodies. All but two specimens were polished on a diamond lap, then etched with orthophosphoric acid for 3 min at temperatures between 190 and 240° C. For material No. 4 the etching time was increased to 5 min. One specimen was differentially polished with Linde A polishing alumina for electron transmission photomicrographs. Both photomigrographs and low-magnification electron-transmission micrographs of shadowed replicas were taken. Figures 14 through 18 are photomicrographs of materials Nos. 1, 2, 3, and 4, respectively.

Grain size in the bodies is given in Table XIII. Average grain size for these bodies varied from 3 to 10 μ for the 95%-purity body to 30 to 40 μ for No. 4.

Porosity in materials 1 and 2 appeared as pores at junctions of three grain boundaries and as pores surrounded by sintered grains. The latter pores were as large as or larger than the average grain size. Porosity was not found in the form of tiny pores distributed along grain boundaries. In material 2 some intergranular porosity was found. In Material 3 the porosity was divided about equally between intragranular and intergranular porosity. In material No. 4 the slight porosity was almost entirely localized at three grain-boundary junctions.

Photomicrographs were made of cross sections of the membrane, membrane surface, cross section of the disks, and disk

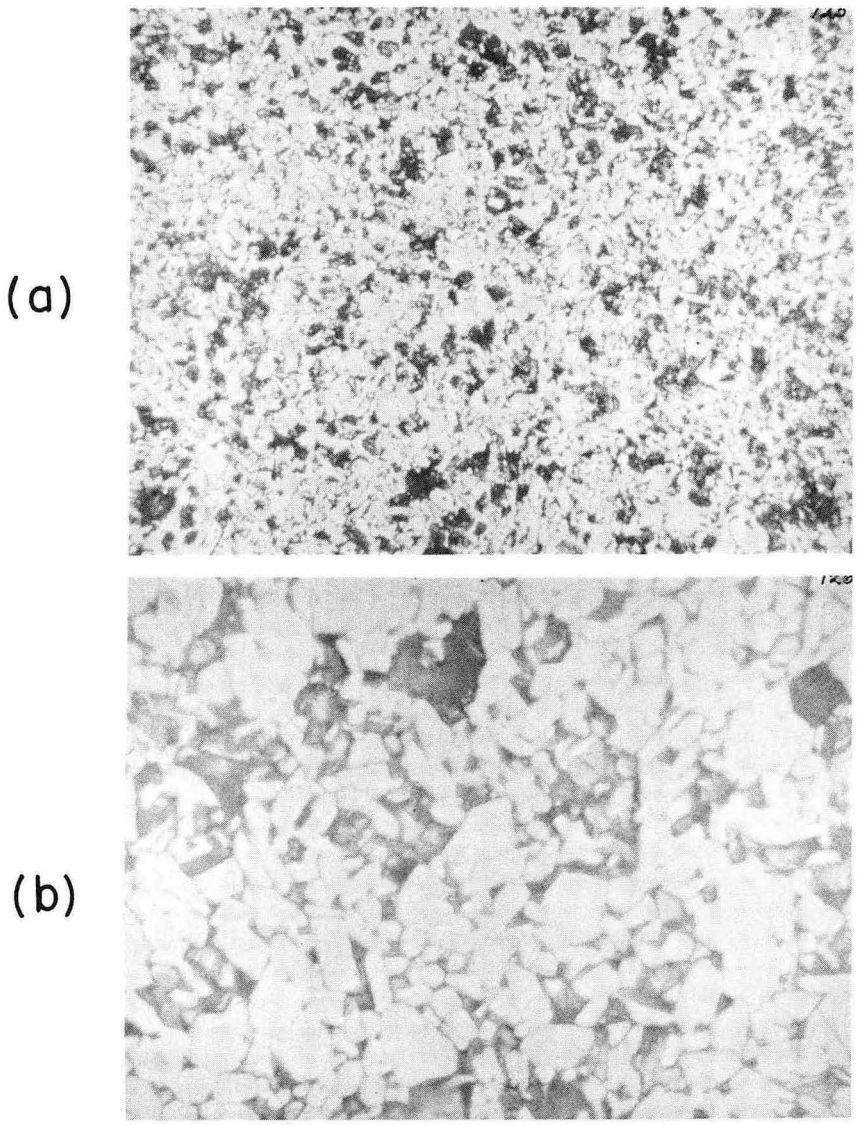

Fig. 14. Photomicrographs of material No. 1, showing grain and pore structure.

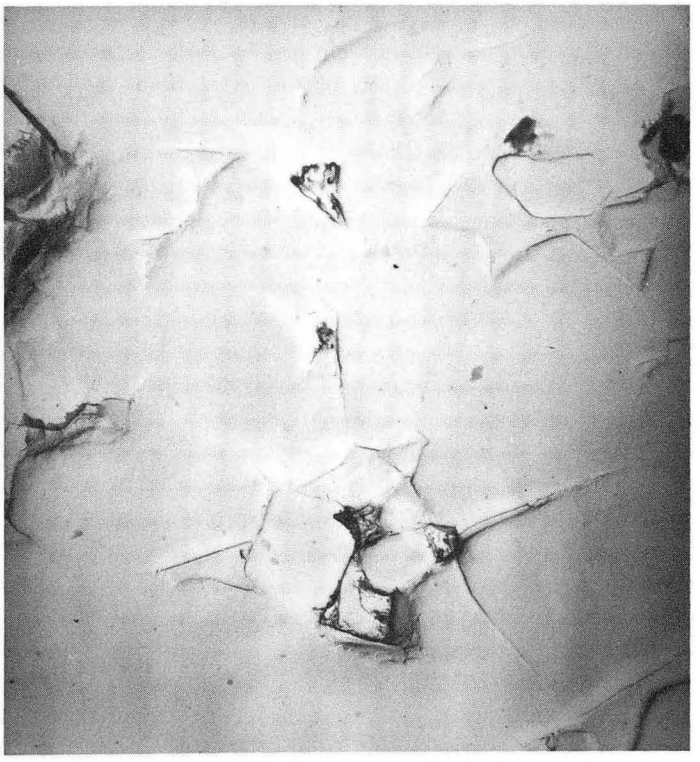

5600 X

ZN-3394

Fig. 15. Photomicrographs of material No. 1, showing second-phase location.

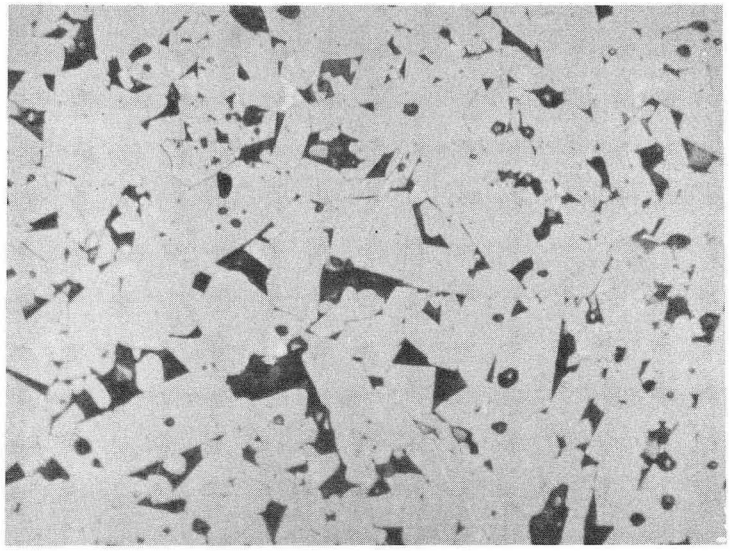

250X

ZN-3395

Fig. 16. Photomicrograph of material No. 2, showing grain and pore structure.

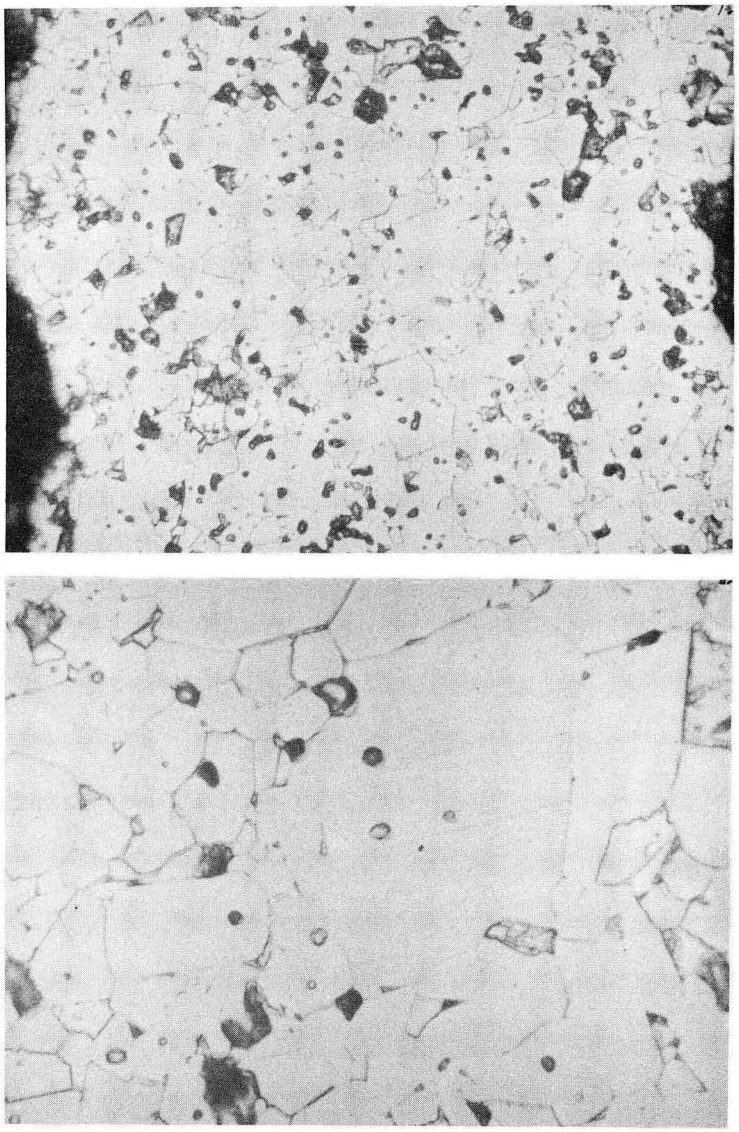

Fig. 17. Photomicrographs of material No. 3, showing grain and pore structure.

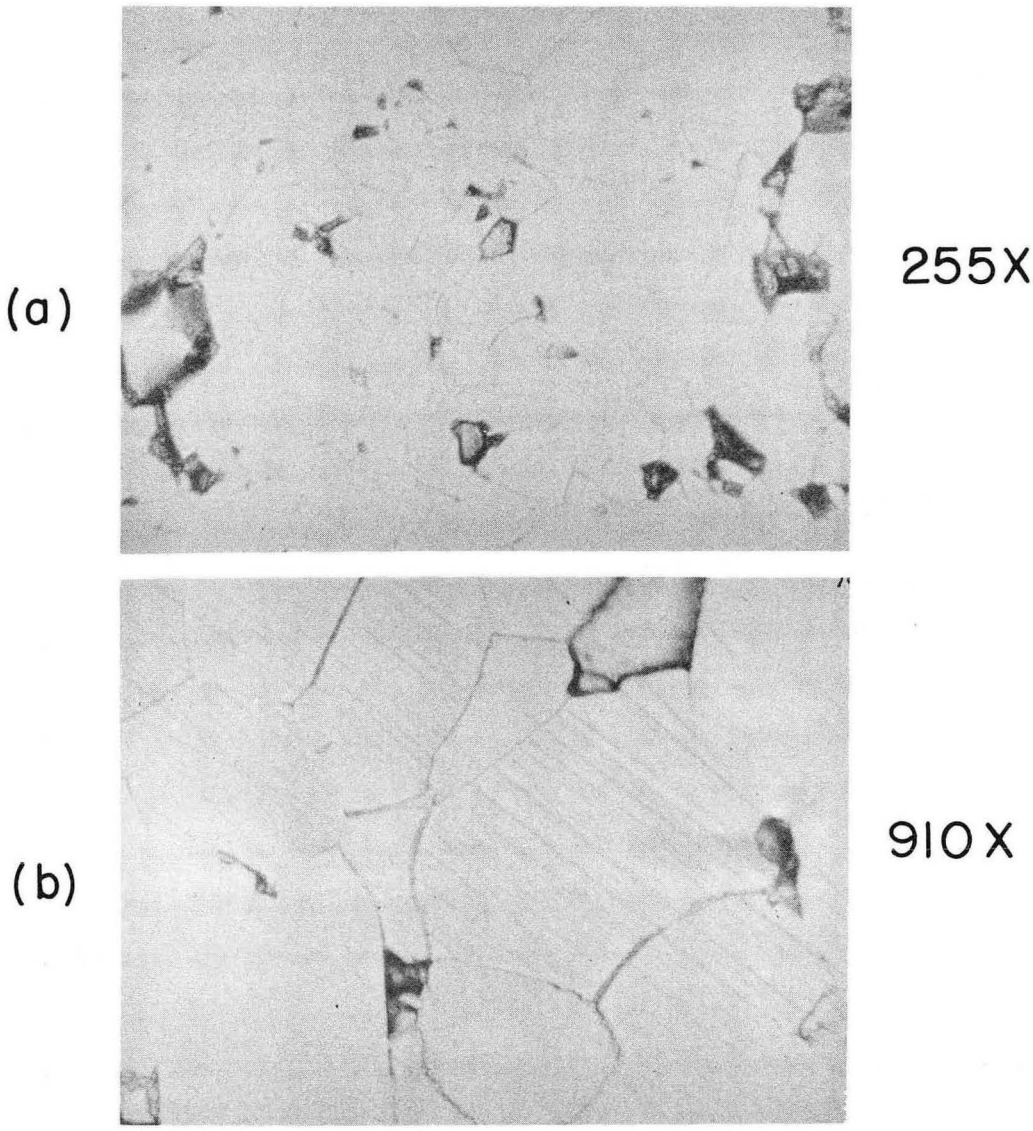

Fig. 18. Photomicrographs of material No. 4, showing grain and pore structure.

Table XIII. Average grain sizes for alumina materials investigated.

Body	Grain size (μ)	
No. 1	3 to 5	Porosity at three boundary junctures
No. 2	10×30 to 30×70	Acicular platelets generally with one unbonded boundary
No. 3	20	Some 60 μ
No. 4	20 to 40	Duplex grain structure ; approximately 25% of grains > 100 μ diameter

surface. No skin effect or other change in structure dependent on distance from surface or other position within the body was found.

2. Equipment

a. Loading Arrangement

The disk specimens were mounted as clamped-edge diaphragms and were loaded concentrically. A schematic of the cross section of the disk and loading arrangement is shown in Fig. 19. There were three vacuum chambers, numbered 1, 2, and 3. Helium was introduced into chamber 2. Chamber 3 was connected to the mass spectrometer, and chamber 1 was added to reduce the likelihood that the test gas would leak out of chamber 2 through the O-ring seal and then into chamber 3 through its O-ring seal.

The loading arrangement shown is for ram loading. Brass bellows sealed the chambers from one another and from the atmosphere. Loads were applied to the rams by means of diaphragm cylinders actuated by air pressure. Air pressure applied to the diaphragm cylinders was controlled by a pressure regulator. Loads available with the diaphragm cylinders employed were 0 to 1600 lb.

b. Cycling Arrangement

Reversal of loading direction, which reversed the stress distribution in the disk, was accomplished by means of time switches and solenoid valves on the pressure lines leading to the diaphragm cylinders. A schematic diagram of the cycling arrangement is shown in Fig. 20. Part (a) represents the arrangement of pressure lines, and part (b) represents the electrical connections between timer and solenoid valves. The lengths of time for load application from either direction were set independently on the timer. Each of these time intervals was variable from 15 sec to 15 min. Thus a complete cycle interval was available from 30 sec to 30 min.

The rate of loading after load direction had been reversed was varied by use of a needle valve between the solenoid valves and the pressure regulator. Usable times for complete reversal of load

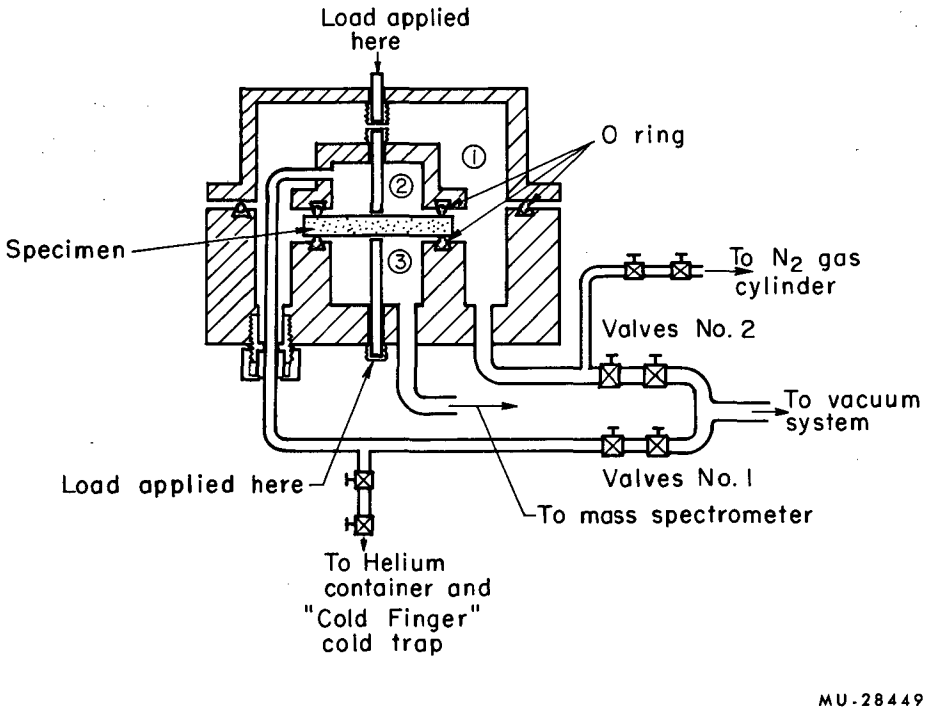

Fig. 19. Schematic representation of disk-stressing device.

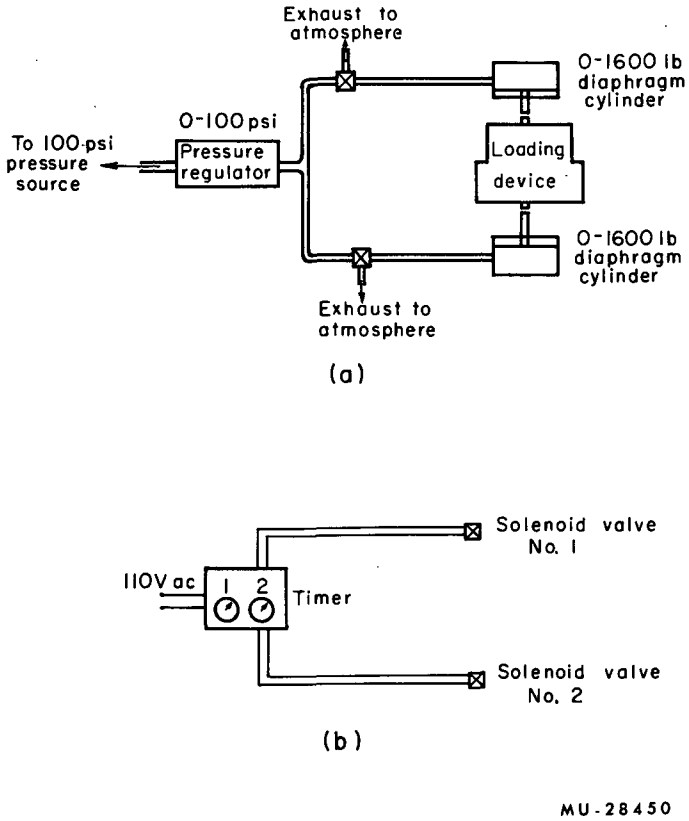

Fig. 20. Schematic representation of
(a) loading apparatus,
(b) loading control apparatus.

direction were on the order of 1/10 sec to several seconds. Load change by manually varying the pressure regulator setting extended this time to several minutes. The effect of rate of change of stress was investigated by these arrangements.

C. Flow-Rate Measurement

A helium leak detector was used to measure the gas flow through disks. A Consolidated Electrodynamics (CEC) leak detector, Model 24-120, was used. All gas passing through the disk passed through the leak detector. Output of the instrument was recorded on a stripchart recorder. A Weston recorder, Model 6701, Type 1, was employed for this purpose.

3. Test Procedure

After a test specimen was placed in the loading device, valves 1 and 2 were opened to the forepump and oil diffusion pump and chambers 1 and 2 pumped down to 1 to 2×10^{-6} mm of Hg and maintained at this pressure for 12 or more hours. To begin a run valves No. 1 were closed and helium admitted. Load magnitude and cycle were selected and applied as required. Mass-spectrometer readings were then recorded continuously.

Some experiments were performed by putting N_2 gas at 1 atm in chamber 2 rather than maintaining a vacuum in it. This was tried in order to reduce the load on the connecting bolts caused by the helium in the chamber and to reduce the amount of helium flow through the O-ring seals.

The actual cycle employed in the experiments reported here consisted of application of the load in a given direction for a fixed time period, then automatic release of the load for a fixed but not necessarily identical period of time. These time periods were set independently of each other. The resulting cycle was repeated automatically as long as desired.

4. Calibration of Equipment

a. Pressure Regulator

The pressure regulator was calibrated in terms of (a) pressure at the diaphragm cylinders and (b) micrometer setting. Calibration was performed with SR_4 strain gages on an aluminum specimen which was previously calibrated in terms of total load on the specimen vs strain. Strain was measured directly with a Baldwin SR_4 strain-gage indicator and converted to load, P, from the calibration curves of the aluminum strain gage device. In Appendix II the data are tabulated in Table XV and plotted in Fig. 33.

b. Mass Spectrometer

The mass spectrometer was calibrated by use of a helium source of known flow rate. The background for the mass spectrometer was determined and then the helium source was vented to the mass spectrometer and allowed to reach steady state. Flow rate is given in the form of cc helium gas (at standard pressure and 26.1° C) per second. Sensitivity is given in the form of this flow rate per percent of recorder full scale with the mass spectrometer on its most sensitive setting. These calculations are given in Appendix III.

C. Outer-Fiber Stresses in Disks

1. Stress Calculations

Stresses induced in the membranes of the blind holes by application of load P were calculated by assuming that the test specimens in the loading device were clamped-edge rigid diaphragms. Three load distributions were investigated. First, a load distributed uniformly over the diaphragm surface was considered. This corresponds to the stress induced by test gas pressure. Second, a point load acting along the diaphragm axis was considered. Third, a load distributed uniformly in a ring concentric with the diaphragm axis was considered. Schematics of loading model and equations that were used for radial and tangential outer-fiber stresses are given in Appendix IV.

2. Stress-Strain Measurements

Strain measurements on specimen 1-4 with a 1/4-in.-diameter blind hole in the center were undertaken to test the applicability of the stress equations and accuracy of the calculated stresses. Three SR_4 (Baldwin) foil-type strain gages were attached to the disk. One was on the surface of the membrane at the bottom of the hole. A second was attached to the opposite surface of the membrane. The third was attached to the disk surface near the edge of the blind-hole opening and within the ring loading radius. Load was applied by the ring arrangement. Plots of strain vs load for all three gages are given in Part F, Appendix IV.

To convert the experimentally determined strains into outer-fiber stresses, it was necessary to determine E, the elastic modulus, and μ Poisson's ratio. These calculations are given in Part D of Appendix IV. The elastic modulus was calculated by an empirical formula given by Knudsen[56] which takes into account the porosity dependency of E. Spriggs presented a similar empirical formula,[57] but Knudsen's formula appears more accurate for high-alumina bodies of the type used in this investigation. Poisson's ratio was also calculated from an empirical formula relating μ to porosity.[56]

With these constants and the biaxial stress-strain relationship, stresses were calculated from the experimental strains. These stresses were compared with the ones calculated from the derived stress formulas. These stresses are compiled in Table XVIII of Part E, Appendix IV. Agreement between experimental and theoretical stresses is satisfactory for tensile stresses but is unsatisfactory for compressive ones. Apparently in compression the 1/4-in.-diameter thin membrane (approx 40 mils) acts like a diaphragm compressed by a load acting radially along its circumference. The result is that the membrane acquires a 0 stress plane and the stress reverses in sign from one surface of the membrane to the other.

On the basis of the above results, four 1/8-in.-diameter blind holes were substituted for the one larger 1/4-in.-diameter

blind hole. Strain measurements were not made on this configuration, but flow measurements made with the configuration strongly suggest that stress, both in compression and in tension, is adequately described by the derived equations.

D. Experimental Results

The observed stress-enhanced flow rates are first grouped according to the kind of applied stress--compressive or tensile. Then within these groups the flow rates are further grouped by material beginning with material No. 1. Finally, for each specimen of each material the flow rates are arranged chronologically.

From the general pattern of flow-rate dependence on stress, loading rate, prior history of the specimen, and microstructure disclosed by this grouping of the experimental data, three different but related phenomena are found. First, initial permeability was found for material No. 1. Second, changing stresses could induce momentary permeability in both materials 1 and 2. Third, the magnitude of both the initial and stress-induced permeabilities decreased with time.

Dimensions of the membranes for each of the specimens are given in Table XIV. Helium flow data for each of the specimens are given in Table XIX through XXXIV in Appendix V. These data are tabulated in the form of

$$\frac{\text{cc He gas (at standard pressure at 79° F)}}{\text{atmosphere He pressure difference} \cdot \text{cm}^2 \text{ conducting area} \cdot \text{sec}}$$

Specimen material is denoted by the first number, while the second number denotes the particular specimen of that material, and the third (final) number denotes the experimental series performed on the particular specimen.

1. Membranes under Compression

Four specimens of material No. 1 and two of material No. 4 were investigated. Three of the specimens of material No. 1 and one of the specimens of material No. 4 contained four 1/8-in.-

Table XIV. Membrane thickness and surface area for Alumina specimens investigated.

Specimen	Membrane thickness (mm)	Membrane diameter (mm)	No. of membranes	Total membrane area (cm^2)	Grinding method
1-2	0.8	5.0	1	0.19	Ultrasonic impact grinding
1-5	0.5	3.0	4	0.28	Diamond + lapping
1-6	1.0	3.0	4	0.28	Diamond + lapping
1-7	0.5	3.0	4	0.28	Diamond + lapping
1-8	1.0	3.0	4	0.28	Diamond + lapping
1-9	0.8	3.0	4	0.28	Diamond + lapping
1-10	0.3	3.0	4	0.28	Diamond + lapping
2-9	0.5	3.0	4	0.28	Diamond + lapping
2-8	1.0	3.0	4	0.28	Diamond + lapping
3-7	0.5	3.0	4	0.28	Diamond + lapping
4-2	0.8	5.0	1	0.19	Ultrasonic impact grinding
4-3	1.0	3.0	4	0.28	Diamond drill + lapping
4-5	0.5	3.0	4	0.28	Diamond drill + lapping

diameter blind holes each. One specimen of material No. 1 and one of material No. 4 each contained one 1/4-in.-diameter blind hole. Table XIX consists of flow-rate data for specimens 1-2, 1-6, 1-7, and 1-9 of material No. 1, and Tables XX and XXI consist of flow-rate data for specimens 4-2 and 4-3 of material No. 4. Membrane thicknesses are given in Table XIV.

No flow was detected through membranes of materials No. 1 and No. 4 for application or release of cyclic compressive stresses for ring-loaded specimens with four 1/8-in.-diameter holes. Compressive stress-induced flow was observed for specimen 1-2 on cyclic release of compressive stresses. Ring loading was used in this case, but the arrangement was one 1/4-in.-diameter blind hole instead of four 1/8-in.-diameter blind holes. Flow-rate data for this specimen may be best plotted against magnitude of released stress. Such a plot is given in Fig. 21. No flow for either release or application of cyclic compressive stresses was detected through the specimen of material No. 4 that contained the one 1/4-in.-diameter blind hole.

Three specimens of material No. 3 were tested earlier. They gave no indication of permeability change with stress. However, these disks contained four 1/4-in.-diameter blind holes and were stressed through center-point loading. Actual stresses were thus uncertain. For this reason they are not listed.

2. Membranes in Tension

a. Material No. 1

Six specimens of material No. 1 were investigated. Helium flow-rate data for specimens 1-2, 1-5, 1-7, 1-8, 1-9, and 1-10 are presented in Tables XXII through XXVIII in the Appendix. Data from these tables are plotted in Figs. 21 through 30. Specimens 1-7-3 and 1-7-4 were run consecutively without removal of disk 1-7 from the test apparatus. The other series for this and the other specimens of material 1 were run after cleaning and oven-drying between series. Specimen 1-2 contained one 1/4-in.-diameter blind hole. The other

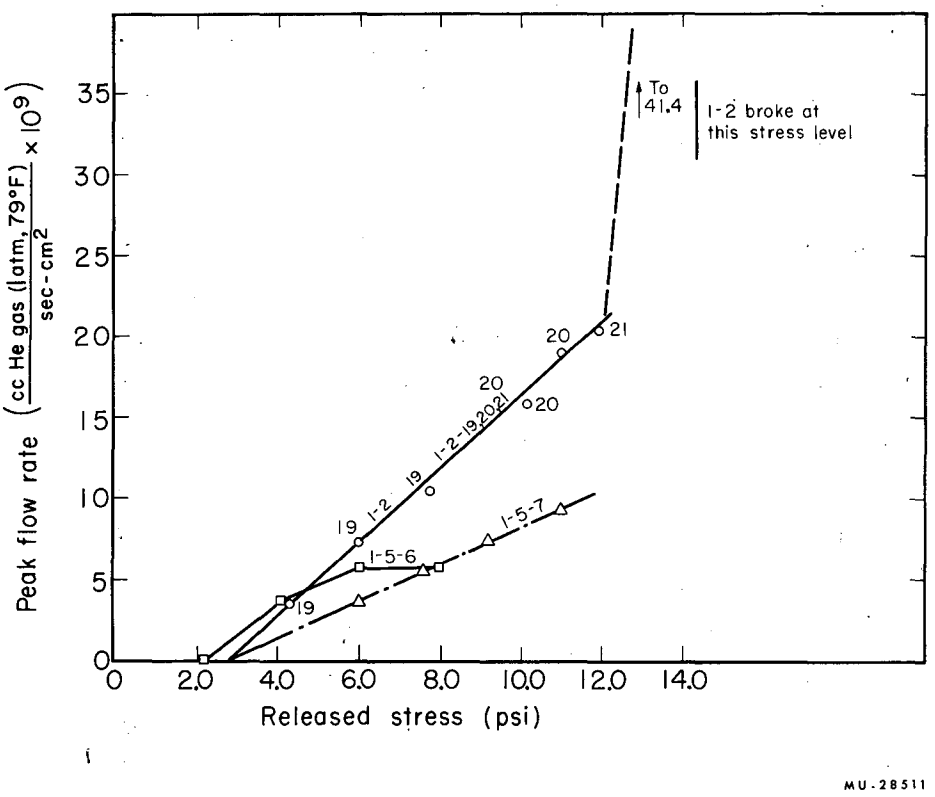

Fig. 21. Peak flow rate as a function of released stress. (Data from Tables XIX, XXIII.)
Specimen 1-2: release of compressive stress, □, △.
Specimen 1-5: release of tensile stress, O.

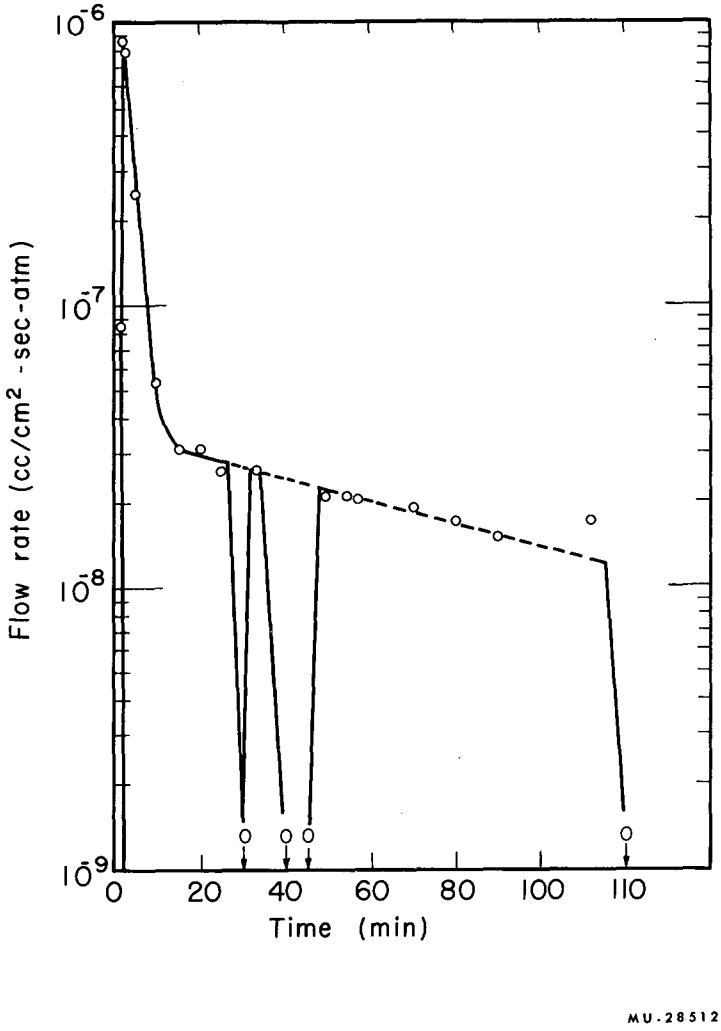

Fig. 22. Flow rate as a function of time for initial contact of helium at 1 atm pressure with specimen 1-7. No applied stress. (Data from Table XXIV a.)

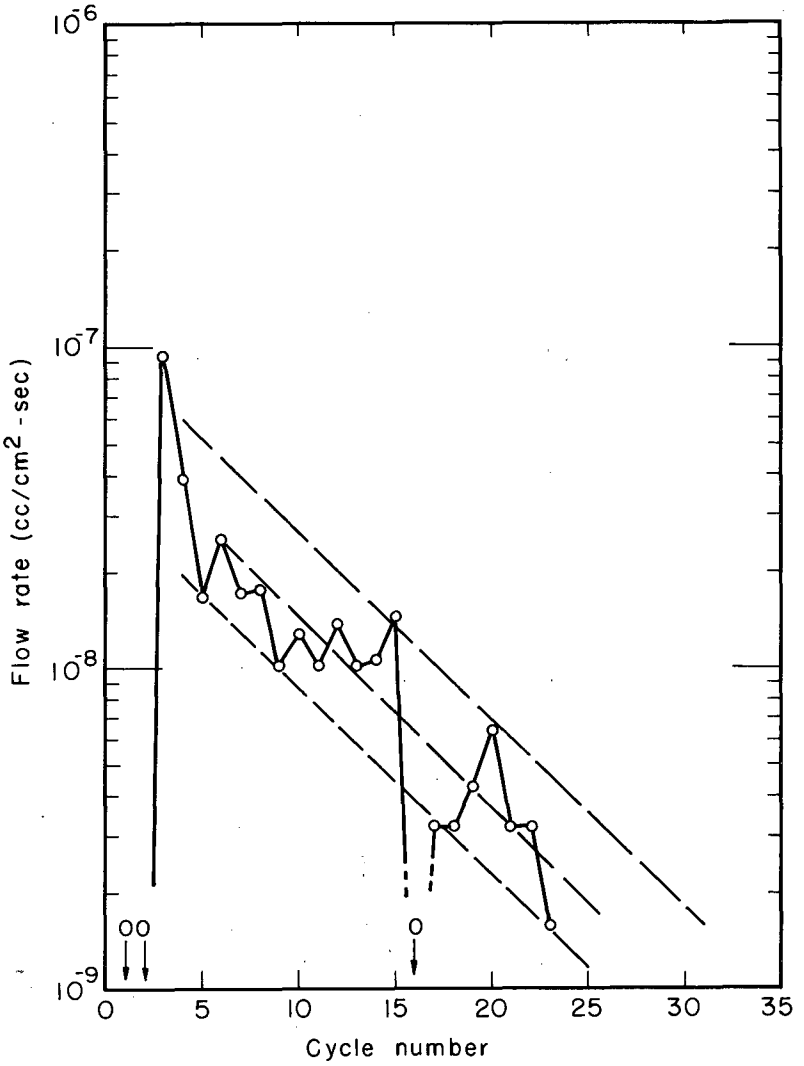

Fig. 23. Peak flow rate under applied tensile stress (TS) as a function of cycle for specimen 1-7-3.
(Data from Table XXV.)
Applied TS = 2500 psi; av load rate = (1.7 to 3)$\times 10^5$ psi/min.

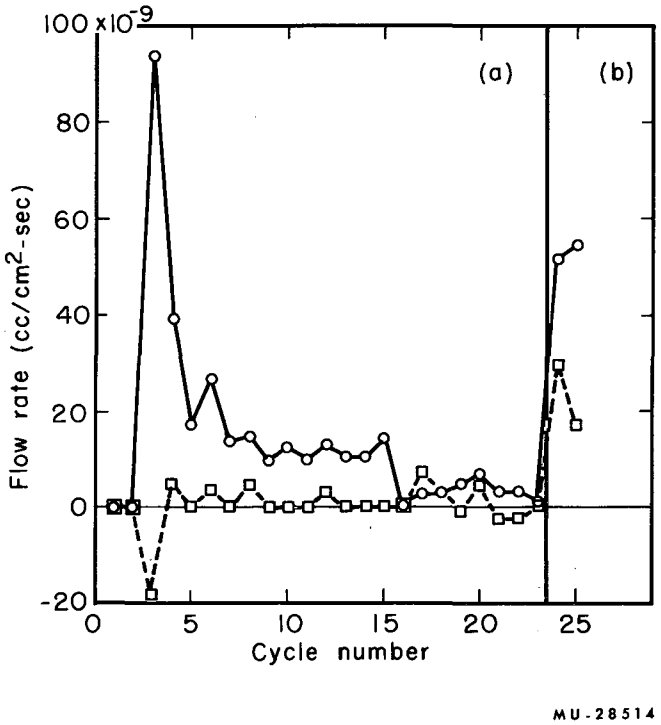

Fig. 24. Peak flow rate for applied and released tensile stress (TS) as a function of cycle for specimen 1-7-3 (Data from Table XXV.)
O———O applied TS.
□-----□ released TS.
TS: Cycles 1-23, 2500 psi;
av load rate = (1.7 to 3.4)$\times 10^5$ psi/min;
Cycles 24-25, 4100 psi;
av load rate = (3.3 to 6.6)$\times 10^5$ psi/min.

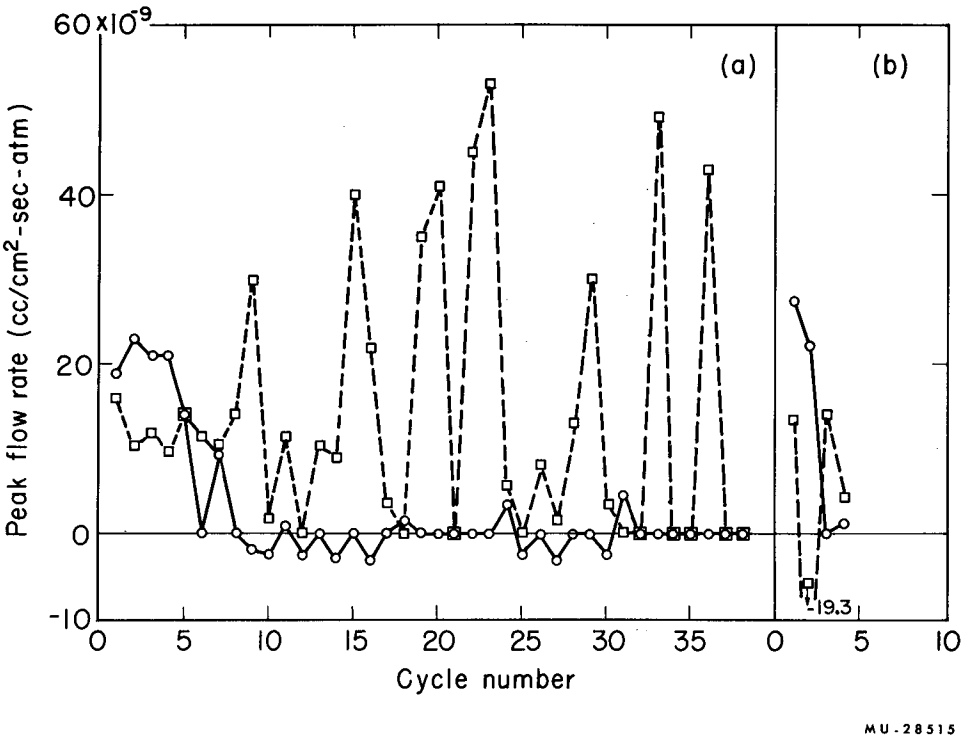

Fig. 25. Peak flow rate for applied and released tensile stress (TS) as a function of cycle for specimen 1-7-3. (Data from Table XXV.)
□-----□ released TS.
O ——— O applied TS.
TS = 4100 psi; stress rate: cycles 1-38, 4.7×10^{4} psi/min; next four cycles, $(3.3 \text{ to } 6.6)\times10^{5}$ psi/min.

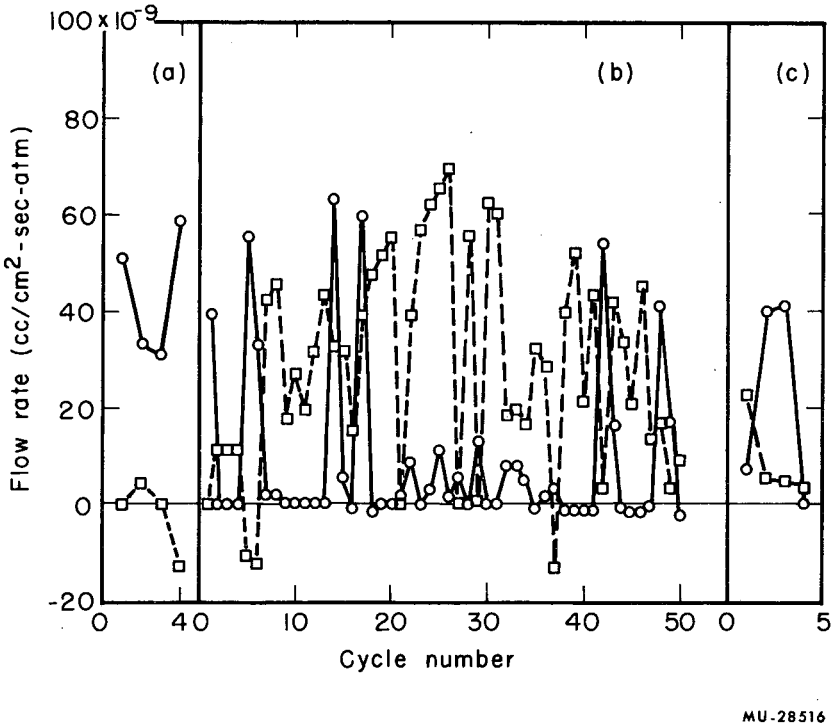

Fig. 26. Flow rate for applied and released tensile stress (TS) as a function of cycle for specimen 1-7-3.
(Data from Table XXV.)
□ - - - - - □ released TS.
O ——— O applied TS.
(a) and (c) TS=5800 psi; load rate = (4.9 to 9.8)$\times 10^5$ psi/min.
(b) TS=4.1$\times 10^3$ psi; stress rate = 4.1$\times 10^3$ psi/min.

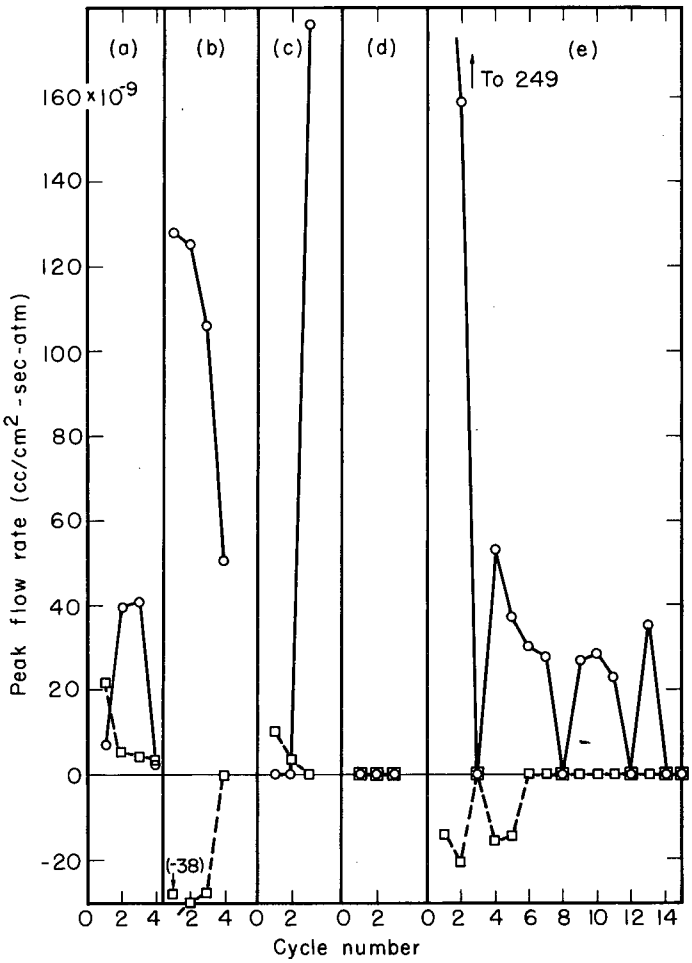

Fig. 27. Flow rate for applied and released tensile stress (TS) as a function of cycle for specimen 1-7-3.
(Data from Table XXV.)
□-----□ released TS.
O ——— O applied TS.
(a) (Repeated from Fig. 26) TS = 5700 psi;
av load rate = (4.9 to 7.8)×10^5 psi/min.
(b) TS = 7600 psi; av load rate = (6.8 to 13.6)×10^5 psi/min.
(c) TS = 7600 psi; av load rate = 6.2×10^4 psi/min.
(d) TS = 4.1×10^3 psi; av load rate = (3.3 to 6.6)×10^5 psi/min.
(e) 2 min load, 2 min no load; TS = 6000 psi;
av load rate = (4.9 to 9.8)×10^5 psi/min.

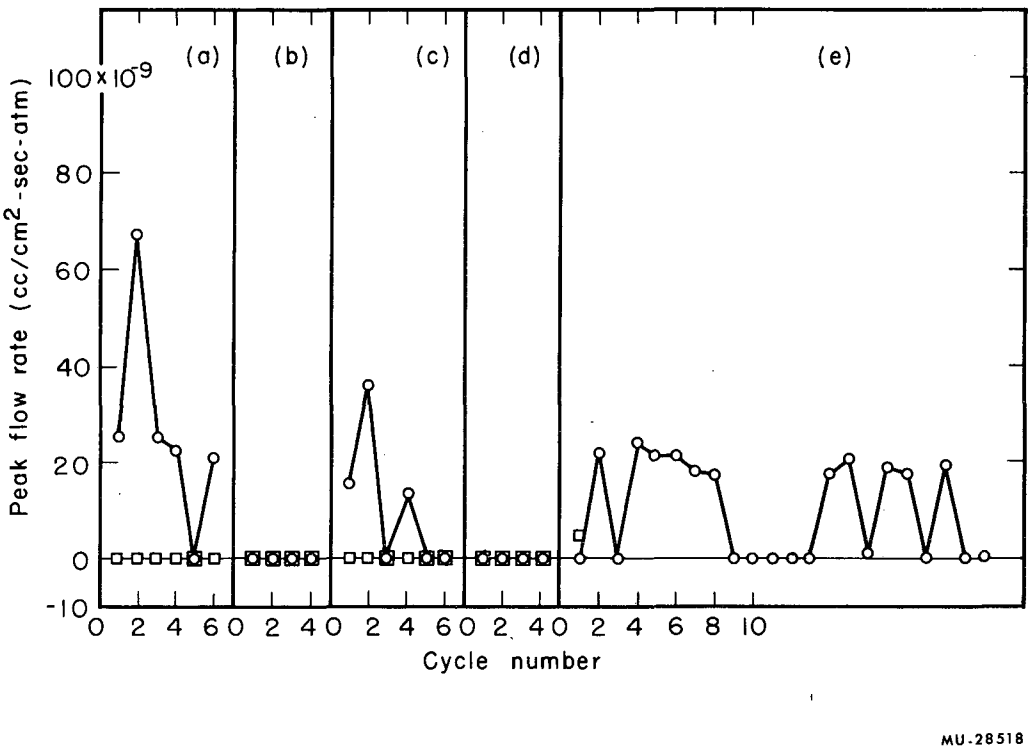

Fig. 28. Peak flow rate for applied and released tensile stress (TS) as a function of cycle for specimen 1-7-4.
(Data from Table XXV.)
O——O applied TS.
□-----□ released TS.
Cycle time: (a) through (d), 2 min load, 2 min no load;
(e) 0.33 min load, 0.66 min no load.
(a) and (c) TS = 7600 psi; av load rate = (6.8 to 13.6)$\times 10^5$ psi/min.
(b) TS = 7600 psi; av load rate = 8.4×10^4 psi/min.
(d) and (e) TS = 9200 psi, av load rate = (8.4 to 16.8)$\times 10^5$ psi/min.

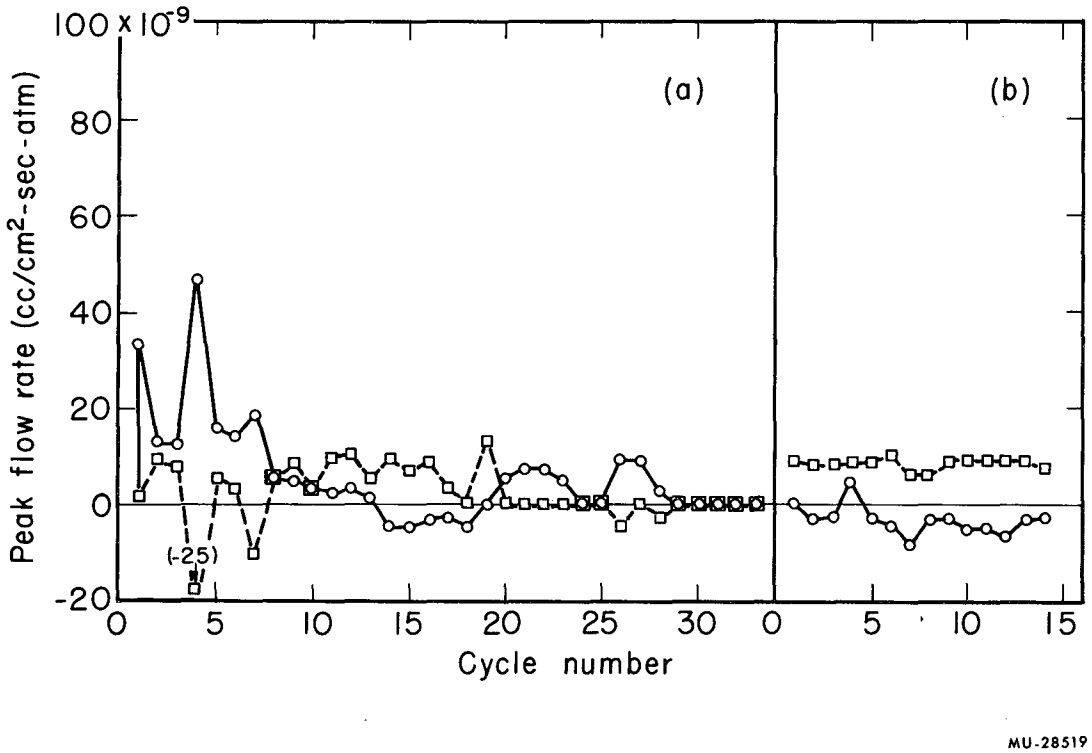

Fig. 29. Peak flow rate for applied and released tensile stress (TS) as a function of cycle for specimen 1-9-1.
(Data from Table XXVII.)
O——— O applied TS.
□-----□ released TS.
2 min load, 2 min no load.
TS: first 34 cycles: 2600 psi;
av load rate = (1.8 to 3.6)$\times 10^5$ psi/min;
next 14 cycles: 4300 psi;
av load rate = (3.5 to 7.0)$\times 10^5$ psi/min.

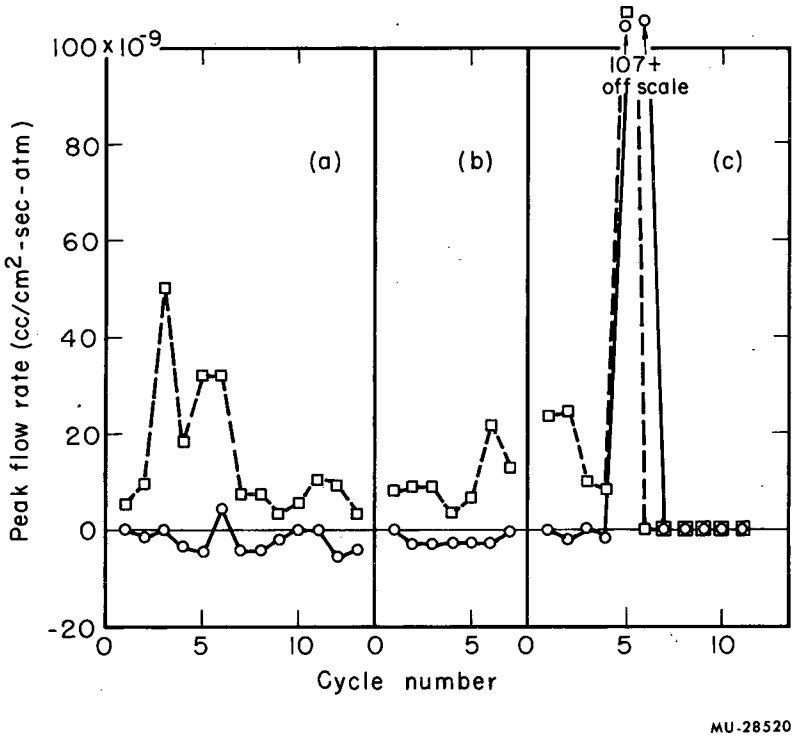

Fig. 30. Peak flow rate for applied and released tensile stress (TS) as a function of cycle for specimen 1-9-1.
(Data from Table XXVII.)
O——O applied TS.
□-----□ released TS.
2 min load, 2 min no load.
(a) TS = 5700 psi;
av load rate = (5.2 to 10.4) $\times 10^5$ psi/min.
(b) TS = 7200 psi;
av load rate = (6.8 to 13.6) $\times 10^5$ psi/min.
(c) TS = 7600 psi;
av load rate = (6.8 to 13.6) $\times 10^5$ psi/min.

five specimens contained four 1/8-in.-diameter blind holes each. Membrane thicknesses for these specimens are given in Table XIV along with total membrane surface area. All specimens were ring loaded.

No flow was observed for specimen 1-2. This specimen contained one 1/4-in.-diameter blind hole and did exhibit compressive stress-induced flow similar to specimen 1-2, but for release of tensile stress rather than for release of compressive stress. These flow-rate data were best plotted against magnitude of stress, and are given in Fig. 21. Specimen 1-7 exhibited stress-enhanced flow rates that were best plotted against cycle. Specimens 1-9 and 1-10 also exhibited similar stress-enhanced flow rates. Stress-enhanced flow-rate data for 1-9 were best plotted against cycle, and are given in Figs. 23 through 27. The flow-rate data for 1-10 consisted of two effects. Initially stress release or application acted to momentarily increase the envelope width for rapidly fluctuating flow rates. After approximately one-half hour the rapid fluctuations ceased. Tensile stress release and application then caused momentary flow to occur, very similar to that found for specimens 1-7 and 1-9. No stress-enhanced flow rates were detected for specimen 1-8.

b. Material No. 2

Two specimens of material No. 2 were investigated. Peak flow rates for tensile stresses for specimens 2-9 and 2-8 are given in Tables XXX and XXXI, respectively. Data for specimen 2-9 are plotted as Fig. 31. Membrane thicknesses are given in Table XIV. Both specimens contained four 1/8-in.-diameter blind holes and were ring loaded. No change in flow rate under tensile stresses was detected for 2-8.

c. Material No. 3

No flow-rate dependence on tensile stress was detected for specimen 3-7. Data for this specimen are given in Table XXXII. This specimen contained four 1/8-in.-diameter holes and was ring

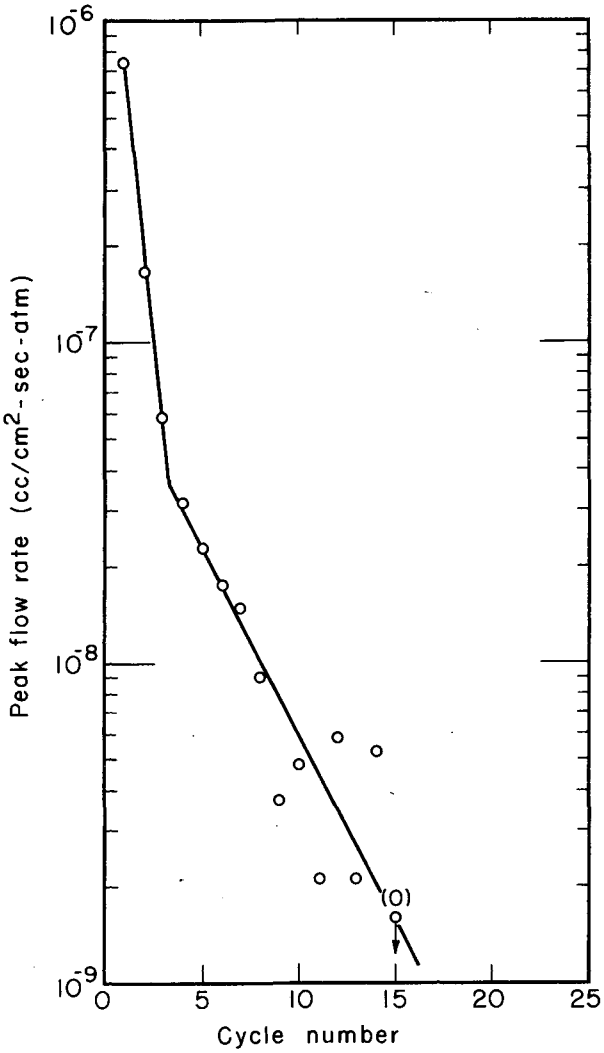

Fig. 31. Peak flow rate for applied tensile stress (TS) as a function of cycle for specimen 2-9-1.
(Data from Table XXX.)
2 min load, 2 min no load.
TS = 2500 psi; load rate = (0.7 to 1.4) $\times 10^5$ psi/min.

loaded. Three other specimens of material 3 were tested earlier. They also gave no indication of permeability change with stress. However, these disks had four 1/4-in. blind holes each and were stressed through center-point loading. Actual stresses were thus uncertain. For this reason they are not listed.

d. Material No. 4

Two specimens of material No. 4 were investigated. Peak-flow-rate data for specimens 4-2 and 4-5 are given in Tables XXXIII and XXXIV. Specimen 4-2 contained one 1/4-in.-diameter blind hole and 4-5 contained four 1/8-in.-diameter blind holes. Both were ring loaded. No flow-rate dependence on stress was detected for any of these specimens.

3. Membranes Free of Stress

Maximum flow rates observed under no externally applied load on initial contact of the specimen with 1 atmosphere of helium are given in Table XXIX. Flow rate as a function of time for specimen 1-7 for these same conditions is given in Table XXIV (a). Initial permeability was shown only by material No. 1. The other three materials were impermeable under these conditions. Figure 22 is a plot of the flow-rate data of Table XXIV (a) as a function of time. Figure 31 is a plot of the maximum flow rates as a function of membrane thickness for material No. 1. Membranes 1 mm thick or thicker showed no initial permeability.

E. Discussion

Changing stress levels cause the normally impermeable disks of material No. 1 to become temporarily permeable. This is shown in Figs. 21 and 23 through 30. To a lesser extent changing stress levels also cause disks of material No. 2 to become permeable. This is shown by Fig 31. Changing stress levels do not cause materials No. 3 or 4 to become permeable--at least within the limits of sensitivity of the instruments used in these experiments.

Initial permeability to helium was observed for material No. 1. The magnitude of this permeability to helium is shown by Fig. 22. Specimens 1-7 and 1-9 both showed this. Whether or not specimen 1-2 or specimen 1-5 was also initially permeable is unknown, as the initial test conditions for them precluded gaining such information. The magnitude of this effect is strongly dependent on the thickness of the membrane, as shown by Fig. 32. A pronounced feature of this initial permeability is its decay with time under essentially zero stress conditions. This decrease in the initial permeability is shown by Fig. 22. No such initial permeability was observed for material No. 2 even though its permeability was dependent on stress. Once the initial permeability disappeared, recleaning and drying the disk in an oven did not bring back this initial permeability.

Two different types of stress dependence on permeability were found for material No. 1. The first stress dependence is shown by Fig. 21. The effect of stress on permeability shown by this plot is completely reversible. A given change in stress from the unstressed state results in a given flow of helium (a fixed peak height for a given stress change). Maximum variation in peak height for a specific stress change lies between 10 and 15 percent. The peak flow rate is essentially linearly dependent on the stress change until stresses near the fracture value are reached.

The second kind of permeability stress dependence is shown by Fig. 23, 24, and 32. The peak flow rates decrease with time and in some cases cease until the magnitude of the cyclic stress is increased. These two related phenomena of peak flow rate decline, and subsequent increase in flow rate with increased stress are shown by Fig. 27.

The last basic aspect of change of gaseous permeability with stress is its dependence on rate of stress application. Figures 23 and 24 compare peak flow rates for release and for application of tensile stress. In these figures it is shown that peak flow rates are caused by application of tensile stress. In this case the loading rate is about $(3.3 \text{ to } 6.6) \times 10^5$ psi/min. Stress release has almost no

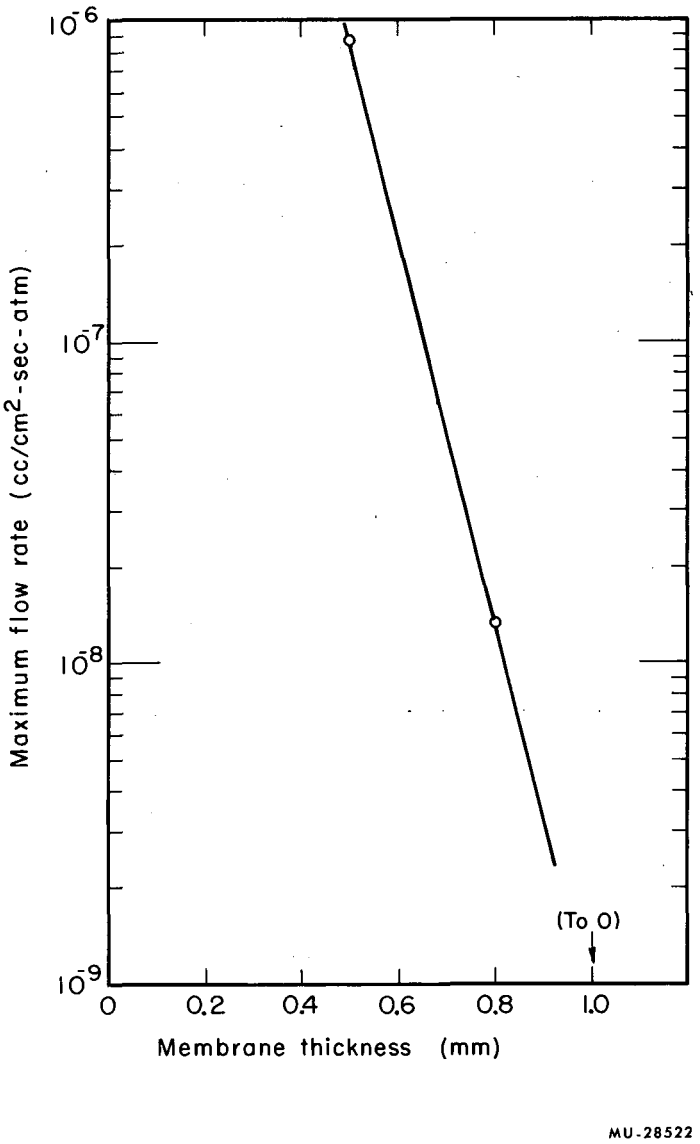

Fig. 32. Maximum flow rate for initial contact of 1 atm helium with material No. 1 as a function of membrane thickness. (Data from Table XXIX.)

effect. Figures 25 and 26, on the other hand, show just the opposite dependence on stress. In Fig. 25 the tensile stress application rate has been reduced to about 4.1×10^4 psi/min, which is an order of magnitude less than the rate in Fig. 24. Peak flow rates now are caused by the release of the tensile stress rather than by its application. Figure 26 shows this same phenomenon. In addition, a return to dependence of peak flow rate on application of tensile stress as stress application rate is increased is indicated by the latter portion of Fig. 26.

The latter portions of Figs. 29 and 30 show a somewhat changed peak-flow-rate dependence on stress change. Peak flow rates are found in tensile stress release, and flow is stopped or decreased by tensile stress application.

No specimens with membranes as thick as or thicker than 1 mm were permeable under stressed or unstressed conditions, within the limits of sensitivity of these experiments.

Material No. 2 was permeable under tensile stress conditions but was not initially permeable under no-load conditions. The decay in peak flow rate under cyclic stress conditions was significantly greater for material No. 2 than for material No. 1, as shown by comparison of Figs. 23 and 24 with Fig. 31.

These varied phenomena may be explained by considering the microstructures of these ceramic bodies, the theory developed above for activated gaseous permeation through membranes, and some of the concepts developed to explain interactions between gases and porous materials.

First consider the microstructures of these four materials as shown by the photomicrographs Figs. 14 through 18. Material No. 1 clearly contains a considerable amount of porosity. The pore size is as large as or larger than the crystal grains. Figure 15 shows that the second phase of this material is a softer substance, probably a glassy phase. Comparison of Figs. 14 and 15 shows that the body is composed of clusters of partially sintered and glassy bonded grains with grain-size or larger pores between these clusters.

Even at 5600 times magnification the porosity observed within these clusters seemed always to be at grain-boundary junctions or along a grain boundary. No porosity was found within the grains. Considerable possibility thus exists for these large pores to be connected together over distances relatively large in comparison with the grain size, so that a maximum amount of porosity is therefore available for gaseous permeation. The calculated porosity content is 7.2%, as shown by Table XII. If reference 20 also holds for Al_2O_3, as much as 2.2% of this porosity is "open" porosity.

Material No. 2 has a structure similar to that of material No. 1. Consider Fig. 16. Comparison of this figure with Fig. 14 shows that for both materials the porosity is primarily intergranular rather than intragranular. However, some of the porosity of material No. 2 is contained within the grains. The grain size of material No. 2 is about three times as large as material No. 1 in terms of linear dimensions. Size of the pores is about the same for both materials. The largest pores seem somewhat smaller than the average grain size of material No. 2. More of the bonding between grains in this material appears to be grain-to-grain contact rather than second-glassy-phase bonding. Porosity is about 5.6%.

The microstructure of material No. 3 differs significantly from that of the first two materials. Comparison of Fig. 17 with Figs. 14 and 16 shows that as much as half the porosity of this material lies within grains. The remaining portion lies along grain boundaries. These pores are generally considerably smaller than the grain size of the material. Average grain size is somewhat smaller than that of material No. 2. Almost all grains appear to be in continuous close contact with adjoining grains. This is in marked contrast to the first two materials, in which many of the grain boundaries are in contact with pores rather than other grains. Grain size and porosity are, respectively, 20 μ and 2.4%.

Material No. 4 is a polycrystalline Al_2O_3 body of almost theoretical density. The grains are as large as in any of the other three

bodies. The small amount of porosity that does exist appears to be entirely confined to grain-boundary junctions. Porosity is about 0.3% and grain diameter about 20 to 40 microns.

The scope of microstructures presented for the four materials is thus one that passes from a material in which most grains are in contact with pores of grain diameter or larger to one in which a few grains are in contact with pores, of diameter an order of magnitude smaller. Possibilities for connecting several pores together decrease in like manner.

From the theory developed above for gaseous permeation of glass, Si, and Ge, large increases in flow rate would necessitate unreasonable decreases in activation energies for solution and diffusion. A typical peak flow rate of $20 \times 10^{-8} \frac{cc(STP)}{sec}$ would require a room-temperature diffusion coefficient of 10^{-2} to 10^{-1} cm^2/sec to satisfy the rapid time rise. The stress-free diffusion coefficient must be less than 10^{-7} cm^2/sec to satisfy the fact that the sensitivity of the mass spectrometer allows detection of diffusion coefficients of this order of magnitude. The ratio of these two diffusion coefficients would then be the ratio of the peak flow rate to the steady-state stress-free flow rate. Such a ratio is equivalent to about 8.2 kcal per g atom decrease in the activation energy for diffusion. This value is greater than the stress-free activation energy of 3.0 kcal per g atom reported by Campbell.[54] Even though it is questionable that the data in reference 54 are correct, there is another more serious objection. That is, that materials No. 3 and No. 4 do not show such an effect. All materials are essentially Al_2O_3. They all have the same crystalline structure. Therefore, all these materials must exhibit very similar characteristics if the flow process is to be through the lattice. These materials do not exhibit the same peak-flow-rate characteristics. Only the two most porous materials show stress-enhanced permeation behavior. A third and final objection is that the initial flow rate for material No. 1 is not linearly dependent on membrane thickness, as is required by permeation theory.

Change in microstructure is the major physical characteristic that distinguishes these materials from one another. The important feature of this microstructure change is the amount and distribution of porosity within each of the bodies. It is clear from the discussion of the photomicrographs and flow-rate phenomena given above that the pores must be at least tenuously connected with one another over considerable distances for material No. 1. To a lesser extent this must also be true for material No. 2. Such a conclusion is no longer reasonable for material No. 3. Not only is total porosity less than one-half that of material No. 2, but also a considerable portion of it is isolated within grains. For material No. 4 the porosity content is extremely small, and it is in the form of small pores widely spaced from one another with little possibility for connection between them. The latter two materials therefore have little capability for gaseous flow along porosity paths.

The experimental data show that no flow occurs through materials Nos. 3. and 4. These have no connected porosity paths. Stress-dependent flow occurs through materials Nos. 1 and 2. These do have some connected porosity. Therefore, at room temperature flow must occur along these connected porosity paths. The initial permeability of material No. 1 is direct evidence of this. The extreme dependence of the peak initial flow rate on membrane thickness is further evidence that these paths exist and are of finite length.

The stress dependence of the flow rates may now be explained. Cross sections of many of these paths must of necessity approach dimensions of atomic helium. These paths are formed by discontinuous bonding between grains. When the load is applied rapidly, it acts at these points of contact between grains. Stresses are concentrated at these points as also are the strains. Enhanced flow then occurs when these contact points are tensilely strained and the cross sections enlarged. Once grains are extensively bonded to one another, as in materials Nos. 3 and 4, stresses and strains can no longer be concentrated in the regions of connections between pores. Rapidly applied or released stresses can no longer cause flow through the membranes.

The decay of stress-dependent flow rate with time observed for materials 1 and 2 may be explained as a capillary condensation phenomenon.[42, 58-63] The adsorption or condensation is undoubtedly a physical adsorption and not chemisorption. This condensation must be on the surfaces of the pores and at constrictions in the connecting paths between pores. It is reasonable to assume that once a stable distribution of adsorbed atoms has been achieved, change of stress conditions in the form of higher tensile stresses or more rapid loading rates will disturb the previously stable helium atom distribution and cause flow until a new stable configuration is reached.

An important objection to this discussion of connected porosity is the possibility that cracks are nucleated in the membranes as a result of forming the blind hole. One attempt at determining if this was a possibility was use of the alternative blind-hole-forming methods of diamond drilling and ultrasonic-impact grinding. No difference between the behavior of membranes formed by these methods was detected. a second supporting reason for discarding this possibility is that a crack, once it begins to grow under stress, will continue to flow under ever decreasing stresses.[64] In some of the specimens tested both pre-existing cracks and crack-nucleation sites existed. Their behavior under stress was in accordance with the Griffith flaw theory discussed in reference 64. On the other hand, the observed behavior of peak flow rates when stress is applied and the decay of the magnitude of these peaks with time are just the opposite of the observed flow-rate behavior through these known cracks. Because variation of the grinding methods had no discernible effect on flow rates, and because flow rates for known cracks differed from that reported and discussed, any supposition of permeability induced through crack formation must be discarded.

IV. SUMMARY AND CONCLUSIONS

In the section on gas permeation through glass matrices, single-crystal germanium, and silicon, it was shown that a thermodynamic treatment of solution of He and Ne in glass, coupled with a previously developed theory for activated diffusion, adequately explained and predicted gaseous permeation through glasses. It was further shown that this theory, when applied to He flow through Si and Ge, adequately explained the experimental data. The theory for gaseous permeation was then further developed to explain and predict the activation energies for diffusion, solution, and permeation for Si and Ge. In principle, this treatment also may be applied to calculation of these same energies for gaseous flow through glasses. The primary source for the energies of the gaseous atoms in the solid matrix was found to be in the repulsive forces between atoms and ions.

In the section on stress-enhanced gaseous permeation through Al_2O_3 bodies, stress dependence of the gaseous permeability of Al_2O_3 materials was investigated. Materials that were normally impermeable under no stress or under static stress conditions were found to become permeable under rapidly varying conditions of induced stress. This permeability stress dependence was shown to be a function of the microstructure of the material. About 5% porosity was found necessary for stress-enhanced porosity-dependent permeability. The porosity was found to be interconnected over distances of several hundred microns. The flow was determined to be only through these interconnected pores. It was also found that helium was adsorbed within the materials on the pore surfaces and along their interconnections. Capillary condensation was postulated as the cause for the decay with time of the helium flow rates through the Al_2O_3 materials.

ACKNOWLEDGMENTS

The author expresses grateful appreciation to Professor R. M. Fulrath for his counsel and direction during the course of this work.

He is grateful to Mr. Larry Ernst for preparation of the photomicrographs, and is particularly indebted to Dr. David J. Meschi for many helpful discussions.

Finally, the author acknowledges the valuable general assistance given by Mr. Orlin Stansfield and Mr. Ronald Ross.

This work was done under the auspices of the U. S. Atomic Energy Commission.

APPENDIX I

Determination of Equations for Solubility Coefficient

A. Starting equations

1. $\Delta G_S = RT \ell n P.$

2. $C = PS,$

   where S = solubility coefficient,

   P = pressure,

   C = concentration of gas atoms in solid.

3. $\Delta G_S = \Delta H_S - T\Delta S_S.$

4. $S = S_0 e^{-\Delta H_S/RT}.$

B. S_0 in terms of starting equations

From $P = e^{+\Delta G_S/RT} = e^{+\Delta H_S/RT - T\Delta S_S/RT},$

$S = C/P$

$S = S_0 e^{-\Delta H_S/RT}.$

we obtain $S_0 = C e^{\Delta S_S/R},$ *

$S = C e^{\Delta S_S/R} e^{-\Delta H_S/RT},$ *

where C and ΔS both refer to the same solid-solution concentration and the gas standard state of one atmosphere and the temperature at which C is measured.

C. S for three degrees of vibration in dissolved state

1. $\Delta S_S = -S_{tr} + \overline{S}_c + \overline{S}_{th},$

$$S_{tr} = R\left[\ell n\left\{\left(\frac{V}{N}\right) e \left(\frac{2\pi mkT}{h^2}\right)^{3/2}\right\}\right] + \frac{3}{2} R$$

$$= R\ell n\left\{\left(\frac{V}{N}\right)\left(\frac{2\pi mkT}{h^2}\right)^{3/2}\right\} + \frac{5}{2}R,$$

$$\bar{S}_c = R\ell n\left(\frac{n_s - n_g}{n_g}\right),$$

where n_g = number of gas atoms dissolved per unit volume of solid solution, assuming random distribution of sites and gas atoms.

$$\bar{S}_{th} = 3R\left[\frac{h\gamma}{kT}\Big/\left(\frac{h\gamma}{e^{kT}-1}\right) - \ell n\left(1 - e^{-h\gamma/kT}\right)\right],$$

$$\Delta S_S = -R\left[\ell n\left(\frac{V}{N}\right)\left(\frac{2\pi mkT}{h^2}\right)^{3/2} + \frac{5}{2}\right] + R\ell n\left(\frac{n_s - n_g}{n_g}\right) +$$

$$R\left[\frac{3h\gamma}{kT}\Big/\left(\frac{h\gamma}{e^{kT}-1}\right) - 3\ell n\left(1 - e^{-h\gamma/kT}\right)\right]$$

$$= R\left[-\ell n\left\{\left(\frac{V}{N}\right)\left(\frac{2\pi mkT}{h^2}\right)^{3/2}\left(1 - e^{-h\gamma/kT}\right)^3\left(\frac{n_g}{n_S - n_g}\right)\right\}\right] +$$

$$R\left[-\frac{5}{2} + \frac{3h\gamma}{kT}\Big/\left(e^{h\gamma/kT}-1\right)\right].$$

2. $\Delta\bar{H}_S = \bar{H}_s - \bar{H}_g$,

$$\bar{H}_g = \frac{3}{2}R + PV = \frac{5}{2}RT,$$

$$\bar{H}_s \approx E_s = 3n\left[\frac{h\gamma}{2} + \frac{h\gamma}{e^{h\gamma/kT}-1}\right],$$

$$\Delta H_S = n\left[\frac{3h\gamma}{2} + \frac{3h\gamma}{e^{h\gamma/kT}-1}\right] - \frac{5}{2}RT.$$

3. Solubility coefficient:

From $$C = \frac{n_g}{n_l} ,$$

where n_l = atom density of gas at STP.

$$S = \frac{n_g}{n_l P} ,$$

$$S = C e^{\Delta S/R} e^{-\Delta H/RT},$$

$$S = \frac{n_g}{P n_l} = \frac{n_g}{n_l} \exp \left\{ - \ell n \left[\frac{V}{N} \left(\frac{2\pi mkT}{h^2} \right)^{3/2} \left(1 - e^{-h\gamma/kT} \right)^3 \left(\frac{n_g}{n_S - n_g} \right) \right] + \right.$$

$$\left. + \frac{3\, h\gamma}{kT} \Big/ \left(e^{h\gamma/kT} - 1 \right) - \frac{5}{2} \right\} \exp \left\{ - \left[\frac{3h\nu}{2\,kT} + \frac{3h\nu}{kT} \Big/ \left(e^{h\nu/kT} - 1 \right) - \frac{5}{2} \right] \right\},$$

$$S = \left(\frac{n_S - n_g}{n_l} \right) \frac{\left(P_0 \right) 1 \left(\frac{h\gamma}{e^{2kT}} \right)^3}{\left(\frac{V}{N} \right) \left(\frac{2\pi mk}{h^2} \right)^{3/2} T^{3/2} \left(1 - e^{-\frac{h\gamma}{kT}} \right)^3}$$

$$\frac{V}{N} = \frac{kT}{P} ,$$

we have $$S = \frac{T^{-5/2}}{k \left(\frac{2\pi mk}{h^2} \right)^{3/2}} \left(\frac{e^{-\frac{h\gamma}{2kT}}}{1 - e^{-\frac{h\gamma}{kT}}} \right)^3 \left(\frac{n_S - n_g}{n_l} \right) \left(P_0 \right) \qquad *$$

and $$n_g = \frac{P\, T^{-5/2}}{k \left(\frac{2\pi mk}{h^2} \right)^{3/2}} \left(\frac{e^{-\frac{h\gamma}{2kT}}}{1 - e^{-\frac{h\gamma}{kT}}} \right)^3 (n_S - n_g) (P_0) , \qquad *$$

where P = gas pressure at which n_g is measured.

D. S for two degrees of translation + one degree of vibration

1. ΔS_S:

From $S_{tr} = R\left[\ell n\left\{\left(\frac{V}{N}\right) e \left(\frac{2\pi mkT}{h^2}\right)^{3/2}\right\} + \frac{3}{2}\right]$,

$$\overline{S}_c = R\,\ell n\left(\frac{n_S - n_g}{n_g}\right),$$

and $$\overline{S}_{th} = R\left[\ell n\left\{\left(\frac{A_s}{N}\right) e \left(\frac{2\,mkT}{h^2}\right)^{2/2}\right\} + \frac{2}{2}\right] + R\left[\frac{h\gamma}{kT}\Big/\left(e^{\frac{h\gamma}{kT}} - 1\right) - \ell n\left(1 - e^{\frac{h\gamma}{kT}}\right)\right]$$

we get $\Delta S_S = R\left[\ell n\left\{\left(\frac{n_s - n_g}{n_g}\right)\left(\frac{V}{N}\right)^{-1}\left(\frac{A_s}{N}\right)\left(\frac{2\pi mkT}{h^2}\right)^{-1/2}\left(1 - e^{-h\gamma/kT}\right)^{-1}\right\} + \right.$

$$\left. - \frac{1}{2} + \frac{h\gamma}{kT}\Big/\left(e^{h\gamma/kT} - 1\right)\right] .$$

2. ΔH_S:

From $H_g = \frac{5}{2} RT$,

and $$\overline{H}_S = n\left\{\frac{h\gamma}{2} + \frac{h\gamma}{\left(e^{h\gamma/kT} - 1\right)}\right\} + 2\left(\frac{RT}{2}\right) + RT$$

we have $\Delta H_S = n\left\{\frac{h\gamma}{2} + \frac{h\gamma}{\left(e^{h\gamma/kT} - 1\right)}\right\} - \frac{1}{2} RT$.

3. Solubility coefficients:

$$S = \left(\frac{n_S - n_g}{n_1}\right) \frac{\left(\frac{A_S}{N}\right) T^{-3/2}}{k\left(\frac{2\pi mk}{h^2}\right)^{1/2}} \left(\frac{e^{h\gamma/2kT}}{e^{h\gamma/kT}-1}\right) (P_0) \quad , \qquad *$$

$$n_g = P(n_S - n_g)(P_0) \frac{\left(\frac{A_S}{N}\right)_T^{-3/2}}{k\left(\frac{2\pi mk}{h^2}\right)^{1/2}} \left(\frac{e^{\frac{h\gamma}{2kT}}}{e^{\frac{h\gamma}{kT}}-1}\right) \qquad *$$

E. S for one degree of translation + two degrees of vibration

1. ΔS_S:

$$S_{tr} = R\left[\ell n \left\{\left(\frac{V}{N}\right) e \left(\frac{2\pi mkT}{h^2}\right)^{3/2}\right\} + \frac{3}{2}\right] ,$$

$$\overline{S}_c = R\ell n\left(\frac{n_S - n_g}{n_g}\right) ,$$

$$\overline{S}_{th} = R\left[\ell n\left\{\left(\frac{L_s}{N}\right) e \left(\frac{2\pi mkT}{h^2}\right)^{1/2}\right\} + \frac{1}{2}\right] + R\left[\frac{2h\gamma}{kT} e^{h\gamma/kT} - 1 \right.$$

$$\left. - 2\ell n\left(1 - e^{-h\gamma/kT}\right)\right] .$$

2. ΔH_S:

$$H_g = \frac{5}{2} RT ,$$

$$H_s = 2n\left[\frac{h\gamma}{2} + \frac{h\gamma}{(e^{h\gamma/kT}-1)}\right] + \frac{1}{2} RT + RT \quad ,$$

$$\Delta H_S = n\left[h\gamma + \frac{2h\gamma}{(e^{h\gamma/kT}-1)}\right] - RT .$$

3. Solubility coefficients

$$S = \left(\frac{n_S - n_g}{n_1}\right) \frac{(L_S/N)\,T^{-2}}{k\,(2\pi mk/h^2)} \left(\frac{e^{h\gamma/2kT}}{e^{h\gamma/kT} - 1}\right)^2 (P_0) \quad , \qquad *$$

$$n_g = P(n_S - n_g) \frac{(L_S/N)\,T^{-2}}{k(2\pi mk/h^2)} \left(\frac{e^{h\gamma/2kT}}{e^{h\gamma/kT} - 1}\right)^2 (P_0) \quad . \qquad *$$

F. Three degrees of translation

1. $\Delta\bar{S}_S$:

$$S_{tr} = R\left[\ell n\left\{\left(\frac{V}{N}\right) e \left(\frac{2\pi mkT}{h^2}\right)^{3/2}\right\} + \frac{3}{2}\right]$$

$$\bar{S}_c = R\,\ell n\left(\frac{n_S - n_g}{n_g}\right)$$

$$\bar{S}_{th} = R\left[\ell n\left\{\left(\frac{V_S}{N}\right) e \left(\frac{2\pi mkT}{h^2}\right)^{3/2}\right\} + \frac{3}{2}\right]$$

$$\Delta S_S = R\,\ell n\left[\left(\frac{V_S}{N}\right) \Big/ \left(\frac{V}{N}\right)\left(\frac{n_S - n_g}{n_g}\right)\right]$$

2. $\Delta\bar{H}_S$:

$$H_g = \frac{5}{2} RT$$

$$\bar{H}_s = \frac{5}{2} RT$$

$$\Delta\bar{H}_S = 0$$

3. Solubility coefficient:

$$S = \left(\frac{n_S - n_g}{n_l}\right)\left(\frac{V_S}{N}\right)\left(\frac{P_0}{k}\right) T^{-1}.$$

$$n_g = P(n_S - n_g)\left(\frac{V_s}{N}\right)\left(\frac{P_0}{k}\right) T^{-1}.$$

APPENDIX II.

Calibration of Pressure Regulator

Table XV. Micrometer and air pressure settings for strain-gage-determined applied loads

Load (lb)	Micrometer setting (in.)	Gage reading (psi)
0.000	0.530	0.0
110	0.512	6.0
180	0.504	8.8
20	0.523	2.0
64	0.517	4.0
118	0.511	6.0
164	0.506	8.0
176	0.504	8.8
	0.515	5
	0.500	10
	0.486	15
	0.472	20
	0.459	25
	0.445	30

These data are plotted in Fig. 33.

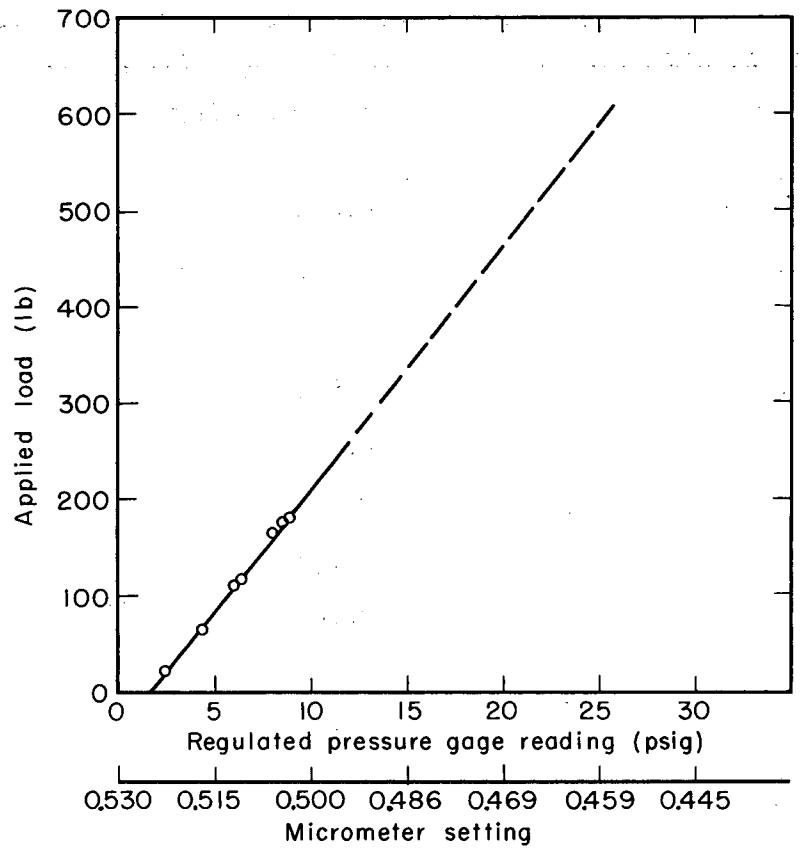

Fig. 33. Load applied to specimen as a function of regulated pressure and micrometer setting.

APPENDIX III.

Calibration of Helium Leak Detector

Helium-calibrated leak rate: $\frac{7.6\times10^{-7} \text{ cc gas (at 1 atm, 79° F)}}{\text{sec}}$

June 7, 1962:

Strip chart recorder reading	28 div on ×100 scale
-Background	- 3 div
	25 div on ×100 scale

$$\frac{7.6\times10^{-7}}{2.5\times10^{3}} = \frac{3.04\times10^{-10} \text{cc gas (at 1 atm, 79° F)}}{\text{sec - div}}$$

July 31, 1962:

Strip chart recorder reading	55 div on ×50 scale
-Background	- 3 div
	52 div on ×50 scale

$$\frac{7.6\times10^{-7}}{5.2\times5\times10^{+2}} = \frac{2.91\times10^{-10} \text{cc gas (at 1 atm, 79° F)}}{\text{sec - div}}$$

Helium leak detector sensitivity = $3.0\times10^{-10} \frac{\text{cc}}{\text{sec-div}}$ *

APPENDIX IV.

Calculation of Stress in Outer Fibers of Disks

A. Stress Caused by Gas Pressures (Theoretical)

1. Loading model:

   see Fig. 34a.

2. Equations (from reference 65):

$$\sigma_{r_{max}} = - \frac{6M_r}{h^2},$$

$$\sigma_{t_{max}} = - \frac{6M_t}{h^2},$$

$$M_r = \frac{q}{16} [\, a^2(1 + \mu) - r^2(3 + \mu) \,],$$

$$M_t = \frac{q}{16} [\, a^2(1 + \mu) - r^2(1 + 3\mu)];$$

$$\sigma_{r_{max}} = - \frac{3}{8} \frac{qa^2}{h^2} \left[(1 + \mu) - \frac{r^2}{a^2} (3 + \mu) \right]$$

$$\sigma_{t_{max}} = - \frac{3}{8} \frac{qa^2}{h^2} \left[(1 + \mu) - \frac{r^2}{a^2} (1 + 3\mu) \right]$$

Uniformly loaded clamped-edge disk. *

B. Stress Caused by Ring Loading (Theoretical)

1. Model:

   see Fig. 34b.

2. Equations (from reference 65):

   a. General:

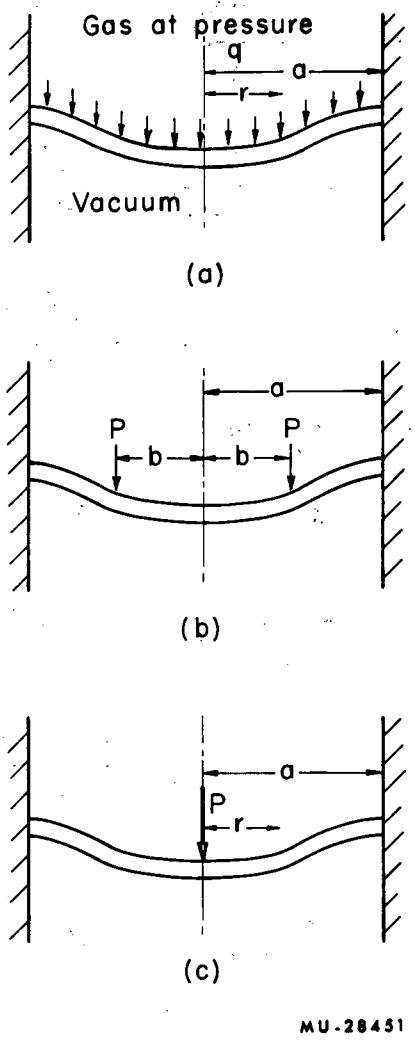

Fig. 34. Loading models for theoretical stress calculations.

$$\sigma_{r_{max}} = \frac{6M_r}{h^2},$$

$$\sigma_{t_{max}} = \frac{6M_t}{h^2},$$

$$M_r = - D \left(\frac{d^2w}{dr^2} + \frac{\mu}{r} \frac{dw}{dr} \right),$$

$$M_t = - D \left(\frac{1}{r} \frac{dw}{dr} + \mu \frac{d^2w}{dr^2} \right).$$

b. Inside the ring:

$$w = \frac{P}{8\pi D} \left[(b^2 + r^2) \ell n \frac{b}{a} + \frac{(a^2 + r^2)(a^2 - b^2)}{2a^2} \right],$$

$$M_{r_i} = - \frac{P}{8\pi} \left[2\ell n \left(\frac{b}{a} \right) + \left(\frac{a^2 - b^2}{a^2} \right) + 2\mu \ell n \left(\frac{b}{a} \right) + \frac{\mu(a^2 - b^2)}{a^2} \right],$$

$$M_{t_i} = - \frac{P}{8\pi} \left[2\ell n \left(\frac{b}{a} \right) + \left(\frac{a^2 - b^2}{a^2} \right) + 2\mu \ell n \left(\frac{b}{a} \right) + \mu \left(\frac{a^2 - b^2}{a^2} \right) \right],$$

$$\sigma_{r_{i_{max}}} = \sigma_{t_{i_{max}}} = - \frac{3}{4} \frac{P}{\pi h^2} \left[2\ell n \left(\frac{b}{a} \right) + 1 - \left(\frac{b}{a} \right)^2 \right] (1 + \mu) \qquad *$$

c. Outside the ring:

$$w = \frac{P}{8\pi D} \left[(a^2 - r^2) \frac{a^2 + b^2}{2a^2} + (b^2 + r^2) \ell n \left(\frac{\mu}{a} \right) \right]$$

$$M_{r_0} = - \frac{P}{8\pi} \left\{ - (1 + \mu) \left[1 + \frac{b^2}{a^2} - 2\ell n \left(\frac{r}{a} \right) \right] + (3 + \mu) + (\mu - 1) \frac{b^2}{r^2} \right\}$$

$$M_{t_0} = -\frac{P}{8\pi}\left\{-(1+\mu)\left[1+\frac{b^2}{a^2}-2\ell n\left(\frac{r}{a}\right)\right] + (1+3\mu)+(1-\mu)\frac{b^2}{r^2}\right\}$$

$$\sigma_{r_{0_{max}}} = -\frac{3P}{4\pi h^2}\left[-(1+\mu)\left(1+\frac{b^2}{a^2}+2\ell n\frac{a}{r}\right) + (3+\mu)+(\mu-1)\frac{b^2}{r^2}\right]^*$$

$$\sigma_{t_{0_{max}}} = -\frac{3P}{4\pi h^2}\left[-(1+\mu)\left(1+\frac{b^2}{a^2}+2\ell n\frac{a}{r}\right) + (1+3\mu)+(1-\mu)\frac{b^2}{r^2}\right]^*$$

C. Stress Caused by Center Loading (Theoretical)

1. Model:

see Fig. 34c.

2. Equations (from reference 65):

For any point not very close to load P,

$$\sigma_{r_{max}} = -\frac{6M_r}{h^2},$$

$$\sigma_{t_{max}} = -\frac{6M_r}{h^2},$$

$$M_r = -\frac{P}{4\pi}\left[(1+\gamma)\ell n\left(\frac{a}{r}\right)-1\right],$$

$$M_t = -\frac{P}{4\pi}\left[(1+\gamma)\ell n\left(\frac{a}{r}\right)-\gamma\right],$$

$$\sigma_{r_{max}} = -\frac{3}{2\pi}\frac{P}{h^2}\left[(1+\gamma)\ell n\left(\frac{a}{r}\right)-1\right], \quad *$$

$$\sigma_{t_{max}} = -\frac{3}{2\pi}\frac{P}{h^2}\left[(1+\gamma)\ell n\left(\frac{a}{r}\right)-\gamma\right]. \quad *$$

D. Calculation of Elastic Modulus and Poisson's Ratio for Al_2O_3 Bodies

1. Elastic Modulus

a. General Equations (from reference 56):

$$E = E_0 e^{-bP},$$

E_0 = 4102 kilobars = 59.4×10^6 psi
[E_0 Theoretical = 59.23×10^6 psi],

b = - 3.95,

P = Fractional pore volume of body.

b. E_{cal} (given in following table)

Table XVI. Calculated elastic moduli for materials investigated

	No. 1	No. 2	No. 3	No. 4*
ρ_{bulk}	3.70 g/cc	3.76	3.89	
ρ_{bulk}/ρ_0	0.928	0.944	0.976	
P	0.072	0.056	0.024	0.003-0.004
bP	0.2844	0.2210	0.0948	
e^{-bP}	0.7525	0.8017	0.9097	
E_{cal}	44.7×10^6	47.6	54.0	57.62

*Values given in Ref. 56: ρ_0 = 3.9879/cc

2. Poisson's Ratio

1. Equation (reference: Knudsen 56)

$$\mu = 0.26 - P(0.30)$$

2. Calculated Values

Table XVII. Calculated Poisson's ratio for materials investigated

	No. 1	No. 2	No. 3	No. 4
P	0.072	0.056	0.024	0.003-0.004
0.3 P	0.0216	0.0168	0.0072	0.0009-0.0012
μ_{cal}	0.2384	0.2432	0.2528	0.26-26

E. Strain Measurements and Corresponding Stresses

1. Material 1-4
2. Equipment and Gage Location
   a. Strain Gages
      Baldwin SR_4 FP
      Foil gages
   b. Strain Gage Indicator
      Baldwin SR_4 strain gage indicator
   c. Strain Gage Location

See Fig. 35(a) for side view and 35(b) for top view of strain gage locations.

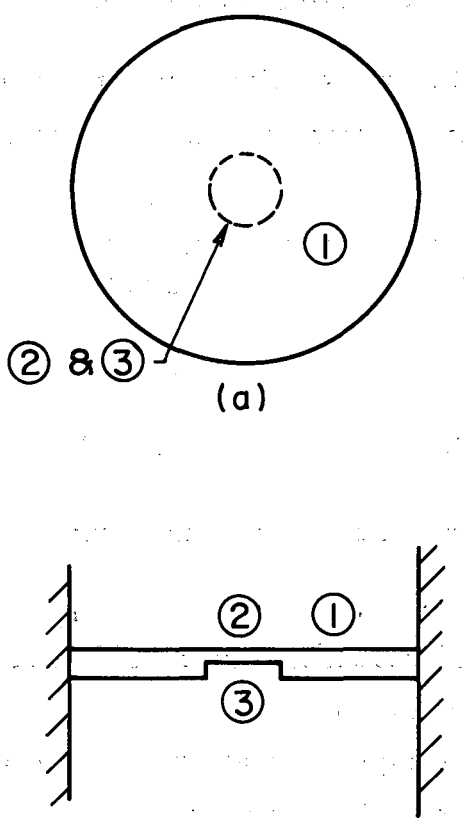

Fig. 35. Locations of strain gages 1, 2, and 3 for specimen 1-4.

3. Strain Measurements vs Load

a. Ring Loading 1-4

See Figs. 36, 37 and 38 for strain measurements for strain gages 1, 2, 3.

b. Uniform Pressure Loading

For a uniform pressure of 14.7 psia gage No. 1 measured -13 μin./in. and gage No. 2 measured -23 μin./in.

4. Comparison of Calculated and Apparent Stresses

The equation for the apparent stress is given by

$$\sigma = \frac{Ee}{(1-\mu)} \quad \text{(biaxial stress)}.$$

Comparison of stresses calculated by this equation by using the measured strains with stresses calculated by the theoretical equations is given in Table XVIII.

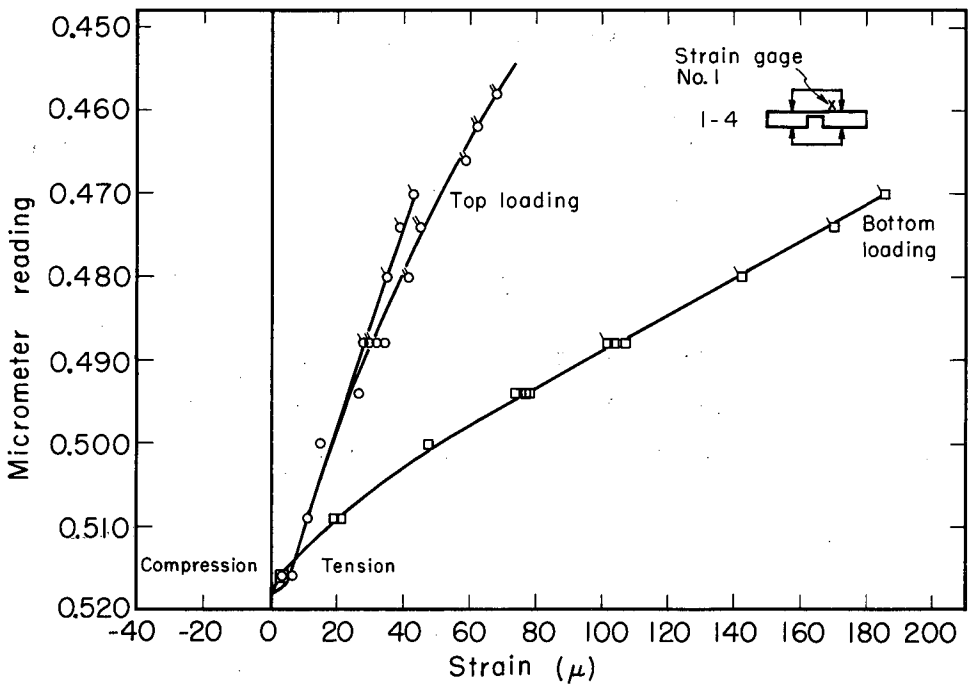

Fig. 36. Strain-gage measurements, gage No. 1. Loading from top and bottom.
O, □ Run No. 1.
O □ Run No. 2.
O Run No. 3.

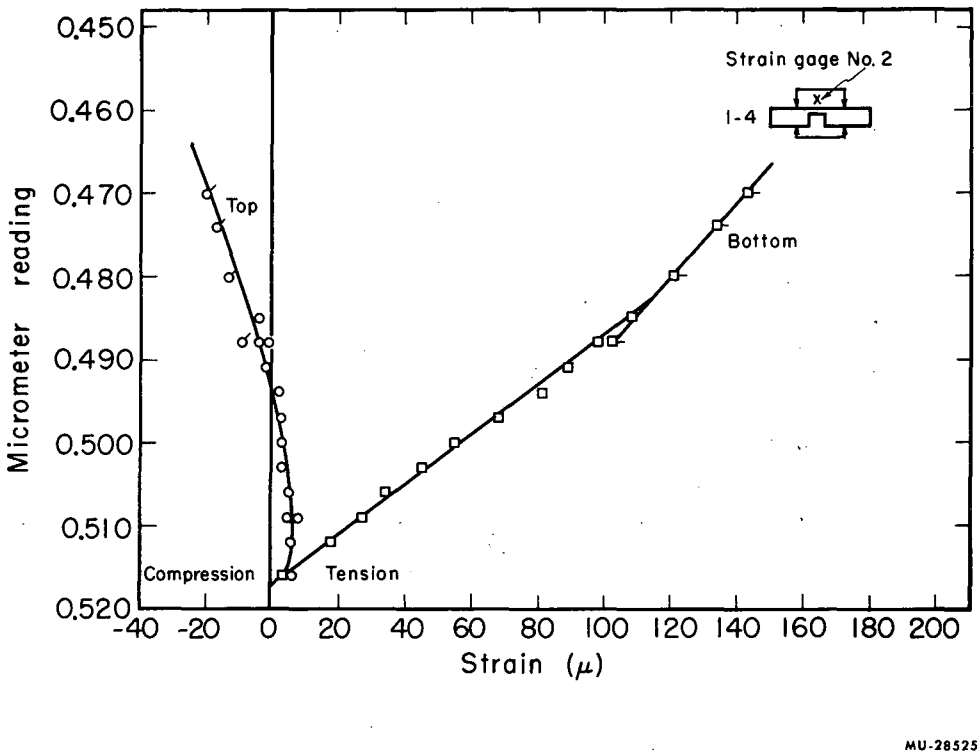

Fig. 37. Strain measurements, gage No. 2.
Loading from top and bottom.
O, □: Run No. 1
O, □: Run No. 2

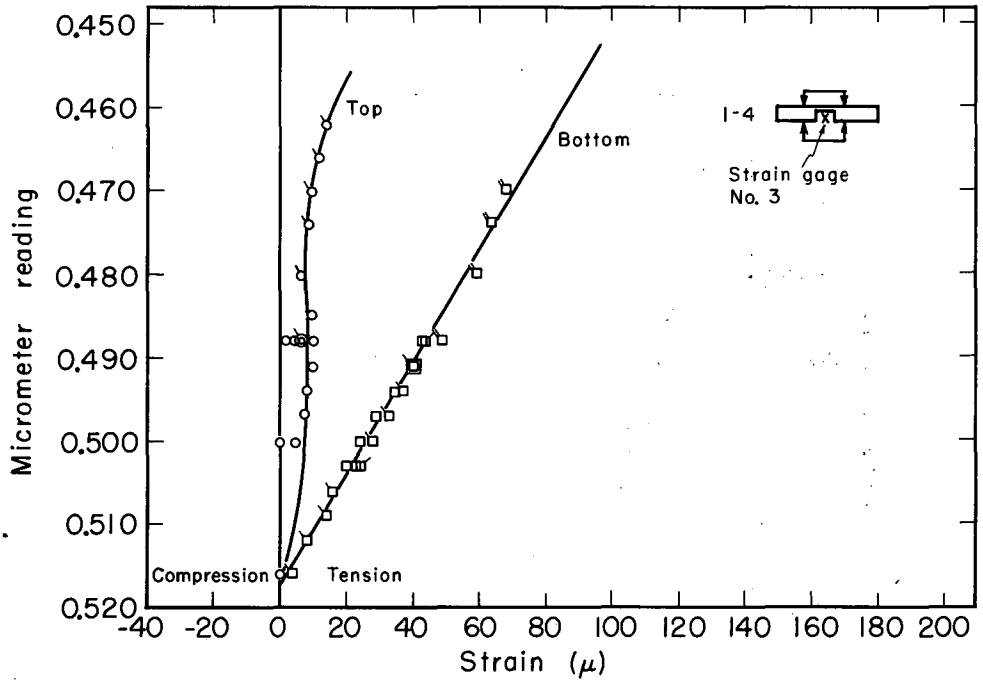

Fig. 38. Strain measurements, gage No. 3. Loading from top and bottom.
○ , □ : Run No. 1
⊘ , ⧄ : Run No. 2
⧄ : Run No. 3
⧄ : Run No. 4

Table XVIII. Comparison of calculated and apparent stresses

Gage point	Load direction	Ring load, P = 300 lb			Uniform load, q = 14.7 psia		
		Strain(e)	σ_{app}	σ_{calc}	Strain	σ_{app}	σ_{calc}
$(\sigma_t)^{(1)}$	bottom	105 $\frac{\mu in.}{in.}$	6160 psi	5970	-	-	-
	top	30	1760 psi	-5970	-13 $\frac{\mu in.}{in.}$	-764 psi	-418 psi
$(\sigma_r)^{(2)}$	bottom	97	5700 psi	5970	-	-	-
	top	-4	-235 psi	-5970	-23	-1350	-1350 psi
$(\sigma_r)^{(3)}$	bottom	44	2580 psi	2985	-	-	-
	top	8.0	468 psi	-2985	-	-	-

(- = compression; + = tension)

Values calculated by assuming $\sigma_{r_{app}} = \sigma_{r_{cal}}$ at gage point (2) for uniform loading in order to calculate a; a was then substituted into the equations for ring loading to calculate ring-loaded stresses. Constants used were

$\mu = 0.238$, $a = 1.405$ in.,
$h = 0.133$ in., $P = 300$ lb.,
$q = 1.405$ in., $E = 44.7 \times 10^6$ psi.

APPENDIX V.

Flow-rate data for materials No. 1 through No. 4, arranged in Tables XIX through XXXIV.

Table XIX. Observed peak flow rates for application of cyclic compressive stresses material No. 1.

Cycle time: 2 min. load, 2 min. no load.
Time to reach maximum load: 0.005 to 0.01 min.
(Flow rates given in cc/cm^2-sec $\times 10^{-9}$)

Part A

Specimen 1-6-1			Specimen 1-7-2			Specimen 1-9-2		
Stress (psi)	No. of cycles	Av. peak flow rates	Stress (psi)	No. of cycles	Av. peak flow rates	Stress (psi)	No. of cycles	Av. peak flow rates
2,200	35	0	2,700	4	0	2,500	29	0
3,000	3	0	4,300	2	0	4,100	10	0
4,100	3	0	5,100	3	0	5,900	4	0
5,900	3	0	6,000	5	0	7,500	11	0
7,500	7	0	7.600	7	0	9,200	3	0
9,200	4	0						
11,000	7	0						

Table XIX. Observed peak flow rates for application of cyclic compressive stresses material No. 1. (Continued)

Part B

Specimen 1-2-19						Specimen 1-2-20						Specimen 1-2-21					
Stress: 4300 psi Peak flow rates for		Stress: 6000 Peak flow rates[a] for		Stress: 7800 psi Peak flow rates for		Stress: 9300 psi Peak flow rates for		Stress: 1000 psi Peak flow rates[a] for		Stress: 11000 psi Peak flow rates for		Stress: 12000 psi Peak flow rates for		Stress: 12800 psi[b] Peak flow rates for		Stress: 13000+ psi Peak flow rates for	
Applied stress	Released stress	Applied stress	Released stress	Applied stress	Released stress	Applied stress	Released stress	Applied stress	Released stress	Applied stress	Released stress	Applied stress	Released stress	Applied stress	Released stress	Applied stress	Released stress
-0.8	3.9	0.0	7.9	0.0	11.8	0.0	13.0	0.0	16.0	0.0	18.2	0.0	22.9	3.9	35.6 47.5	Specimen broke	
13.0	3.2	0.0	7.9	0.0	11.0	0.0	17.0	0.0	15.0	0.0	20.6	0.0	18.2				
0.0	4.7	0.0	7.9	0.0	11.0	0.0	17.0	0.0	?	0.0	14.2	0.0	19.8				
2.4	3.2	0.0	7.1	0.0	9.5	0.0	17.0			0.0	22.1	0.0	22.1				
0.0	3.9	0.0	8.7	0.0	10.0	0.0	16.0			0.0	19.8	0.0	20.6				
0.0	3.9	0.0	7.9	0.0	9.5	Every 5th cycle recorded				0.0	19.0	0.0	19.0				
0.0	2.4	0.0	7.1	0.0	9.5					0.0	19.0						
0.0	3.2	0.0	6.3	0.0	9.5												
0.0	3.2	0.0	5.5														
0.0	3.2	Every 5th cycle recorded															
0.0	3.9																

[a] Every 5th cycle recorded

[b] Manually applied load. Time to reach maximum load was 0.2 min.

Table XX. Observed peak flow rates for application of cyclic compressive stresses. Material No. 4. Cycle time: 2 min load, 2 min no load. Time to reach maximum load: 0.005 to 0.01 min. (Flow rates given in $cc/cm^2\text{-}sec \times 10^{-9}$.)

Specimen 4-2-36		
Stress (psi)	No. of cycles	Av. peak flow rates
2200	7	0
3200	20	0
4100	18	0
5900	3	0
7500	2	0
9200	5	0
11000	2	0

Table XXI. Observed peak flow rates for application of cyclic compressive stresses. Material No. 4. Cycle time: 2 min load, 2 min no load. Time to reach maximum load: 0.005 to 0.01 min. (Flow rates given in cc/cm^2-sec $\times 10^{-9}$.)

Specimen 4-3-1

Stress (psi)	No. of cycles	Av. peak flow rates
4200	2	0.0
6000	2	0.0
7600	2	0.0
9200	2	0.0
11000	2	0.0
12000	2	0.0
12800	2	0.0
Cycle time changed to 15 min load, 2 min no load		
13500	2	0.0
14600	1	0.0
Cycle time returned to 2 min load, 2 min no load		
14900	2	0.0
16000	3	0.0
17000	1	0.0
17900	Fractured	

Table XXII. Observed peak flow rates for application of cyclic tensile stresses. Material No. 1. Cycle time: 2 min load, 2 min no load. Time to reach maximum load: 0.005 min to 0.01 min.

Specimen 1-2-18

Stress (psi)	No. of cycles	Av. peak flow rates for	
		Applied stress	Released stress
		1.3×10^{-9} cc/cm^2-sec	
4300	7		-0.6
5000	4	0.8	-0.8
6000	8	0.8	-0.8
6700	7	0.8	-0.8
7600	30	0.8	-0.8
8300	7	0.8	-0.8
8800	9	0.8	-0.8

Table XXIII. Observed peak flow rates for application of cyclic tensile stresses. Material No. 1. Cycle time: 2 min load, 2 min no load. Time to reach maximum load: 0.005 min to 0.01 min.

Specimen 1-5-6						Specimen 1-5-3		Specimen 1-5-7							
Stress: 4100 psi		Stress: 2200 psi		Stress: 6000 psi		Stress: 8100 psi		Stress: 6000 psi		Stress: 7600 psi		Stress: 9200		Stress: 1100	
Peak flow rates for		Peak flow rates for		Peak flow rates for		Peak flow rates for		Peak flow rates for		Peak flow rates for		Peak flow rates for		Peak flow rates for	
Applied stress	Released stress	Applied stress	Released stress	Applied stress	Released stress	Applied stress	Released stress	Applied stress	Released stress	Applied stress	Released stress	Applied stress	Released stress	Applied stress	Released stress
					5.7×10^{-9}		4.5×10^{-9}		3.6×10^{-9}		7.1×10^{-9}		10×10^{-9}		10.7×10^{-9}
0.0	0.0	0.0	0.0	0.0	cc/cm^2-sec	0.0	cc/cm^2-sec	0.0	cc/cm^2-sec	-0.7	cc/cm^2-sec	-0.7	cc/cm^2-sec	-0.7	cc/cm^2-sec
	2.1×10^{-9}			-1.4×10^{-9}		2.7×10^{-9}									
0.0	cc/cm^2-sec	0.0	0.0	cc/cm^2-sec	5.7	cc/cm^2-sec	4.3	-0.7	3.6	-0.7	5.7	-0.7	7.8	0.0	9.3
0.0	3.6	0.0	0.0	-0.7	6.4	1.1	3.7	-0.7	3.6	-0.7	5.7	-0.7	7.1	-0.7	9.3
-0.7	3.6	0.0	0.0	-1.5	5.7	1.1	4.3	-0.7	3.6	-0.7	5.7	-0.7	7.8	-0.7	9.3
-0.7	4.3	0.0	0.0	-0.7	4.3	1.1	4.8			-0.7	5.0	-0.7	7.8	-0.7	8.6
-0.7	4.3	0.0	0.0	-0.7	5.7					-0.7	5.7	0.0	7.1	-0.7	8.6
-0.7	4.3			-0.7	5.7					-0.7	5.0	0.0	7.1		
0.0	3.6			-0.7	5.7					-0.7	5.0	-0.7	7.1		
-0.7	3.6			-0.7	5.7					-0.7	5.0	-0.7	7.1		
-0.7	2.8			-0.7	4.9					-0.7	5.0	-0.7	7.1		
				-0.7	5.7										
				-0.7	4.9										
				-0.7	5.3										
				-0.7	5.3										
				-0.7	5.3										
				-0.7	5.3										

Table XXIV(A). Observed flow rate with time for initial contact of helium at one atmosphere with specimen 1-7-1 under no applied load helium dried by passage through a liquid nitrogen cold trap.

Time	(min)	0.0	1.5	2.0	2.5	5.0	10.0	15.0
Flow rate	$(\frac{cc \times 10^9}{cm^2\text{-sec}})$	0.0	85.0	870.0	790.0	250.0	53.0	32.0
Time	(min)	20.0	25.0	30.0	34.5	40.0	45.0	47.5
Flow rate	$(\frac{cc \times 10^9}{cm^2\text{-sec}})$	32.0	26.0	0.0	26.0	0.0	0.0	22.0
Time	(min)	54.0	57.0	70.0	80.0	90.0	107.0	110.0	$<t<105$
Flow rate	$(\frac{cc \times 10^9}{cm^2\text{-sec}})$	22.0	21.0	19.0	17.0	15.0	17.0	0.0	0.0

Table XXIV(B). Observed peak flow rates for application of cyclic tensile stresses immediately after cessation of flow shown by Table XVII for specimen 1-7-1.

Cycle time: 2 min load, 2 min no load. Time to reach max. load: 0.005 to 0.01 min			Cycle time: 1 min load, 1 min no load. Time to reach max. load: 0.005 to 0.01 min			Cycle time: 15 sec load, 15 sec no load. Time to reach max. load: 0.005 to 0.01 min		
Stress (psi)	No. of cycles	Av. peak flow rates	Stress (psi)	No. of cycles	Av. peak flow rates	Stress (psi)	No. of cycles	Av. peak flow rates
1250	3	0	3600	5	0	7600	2	0
2700	3	0				9400	4	0
4300	3	0						
6000	3	0						
6900	3	0						
7600	4	0						
8400	17	0						
9400	4	0						

Table XXV. Observed peak flow rates for application of cyclic tensile stresses. Material No. 1. Specimen 1-7-3. Cycle time: 2 min load, 2 min no load. (Flow rates given in cc/cm^2 - sec $\times 10^9$).

Time to reach max. load: 0.005 to 0.01 min				Time to reach max. load: 0.08 min				Time to reach max. load: 0.005 to 0.01 min				Time to reach max. load: 0.005 to 0.01 min				Time to reach max. load: 0.07 min				Time to reach max. load: 0.005 to 0.01 min	
Stress: 2500 psi		Stress: 4100 psi		Stress: 4100 psi				Stress: 4100 psi		Stress: 5800 psi		Stress: 4100 psi								Stress: 5800 psi	
Peak flow rates for		Peak flow rates for		Peak flow rates for				Peak flow rates for		Peak flow rates for		Peak flow rates for								Peak flow rates for	
Applied stress	Released stress	Applied stress	Released stress	Applied stress	Released stress			Applied stress	Released stress	Applied stress	Released stress	Applied stress	Released stress							Applied stress	Released stress
0.0	0.0	52.4	30.0	19.3	16.1	+3.2	5.4	27.3	13.4	50.8	0.0	39.6	0.0	2.7	62.1	-0.5	13.4	7.0	22.5		
0.0	0.0	55.1	17.1	23.0	10.2	-2.7	0.0	22.0	-19.3	33.2	4.3	0.0	10.7	11.2	64.8	40.7	16.1	40.2	5.4		
91.0	-19.3			20.9	12.3	0.0	8.0	0.0	24.1	31.0	0.0	0.0	10.7	-1.1	69.6	17.1	2.7	41.2	4.3		
39.1	4.8			21.4	9.6	-3.2	1.6	1.1	4.3	58.5	-12.8	0.0	10.7	5.4	0.0	-2.1	9.1	2.7	3.7		
16.6	0.0			14.5	13.9	0.0	13.4					55.1	-10.7	0.0	55.6						
25.2	3.7			-2.7	11.8	0.0	30.5					33.2	-12.3	12.8	0.0						
17.1	0.0			9.6	10.2	-2.7	3.7					2.1	42.3	0.0	62.1						
17.7	4.8			-3.2	13.9	+4.8	0.0					2.1	45.5	0.0	60.0						
10.7	0.0			-2.1	30.5	0.0	0.0					0.0	17.7	8.0	18.2						
12.9	0.0			-2.7	1.6	0.0	48.7					0.0	26.8	8.0	19.2						
10.2	0.0			+1.1	11.8	0.0	0.0					0.0	19.8	4.8	16.6						
13.9	3.2			-2.7	0.0	0.0	0.0					0.0	31.6	-1.1	32.1						
10.2	0.0			0.0	10.2	0.0	33.2					0.0	43.4	1.6	28.4						
10.7	0.0			-3.2	9.1	0.0	0.0					63.1	32.1	3.2	-13.4						
14.5	0.0			0.0	39.6	0.0	0.0					5.4	31.6	-1.6	40.2						
0.0	0.0			-3.2	22.0							-1.1	15.0	-1.1	51.8						
3.2	7.5			0.0	38.4							59.4	39.1	-1.1	20.9						
3.2	3.2			+1.6	0.0							-1.6	47.7	-1.6	42.8						
4.3	-1.1			0.0	35.3							0.0	51.8	54.0	3.2						
6.4	4.8			0.0	41.7							0.0	55.1	16.0	41.8						
3.2	-2.7			0.0	0.0							2.1	0.0	-1.1	32.7						
3.2	-2.7			0.0	45.5							8.6	39.0	-1.6	20.3						
1.6	0.0			0.0	53.5							0.0	56.7	-1.6	45.5						

Time to reach max. load: 0.005 to 0.01 min		Time to reach max. load: 0.11 min		Time to reach max. load: 0.005 to 0.01 min		Time to reach max. load: 0.005 to 0.01 min				Time to reach max. load: 0.005 to 0.01 min		Time to reach max. load: 0.08 min		Time to reach max. load: 0.005 to 0.01 min		Time to reach max. load: 0.005 to 0.01 min	
Stress: 7600 psi		Stress: 7600 psi		Stress: 4300 psi		Stress: 6000 psi				Stress: 7600 psi		Stress: 7600 psi		Stress: 7600 psi		Stress: 9200 psi	
Peak flow rates for		Peak flow rates for		Peak flow rates for		Peak flow rates for				Peak flow rates for		Peak flow rates for		Peak flow rates for		Peak flow rates for	
Applied stress	Released stress	Applied stress	Released stress	Applied stress	Released stress	Applied stress	Released stress			Applied stress	Released stress	Applied stress	Released stress	Applied stress	Released stress	Applied stress	Released stress
129.6	-41.1	0.0	10.7	0.0	0.0	242.0	-13.9	27.8	0.0	25.7	0.0	0.0	0.0	16.1	0.0	0.0	4.8
127.0	-32.1	0.0	3.7	0.0	0.0	161.0	-21.4	0.0	0.0	68.0	0.0	0.0	0.0	36.4	0.0	21.9	0.0
107.0	-29.4	180.0	0.0	0.0	0.0	0.0	0.0	0.0	0.0	25.2	0.0	0.0	0.0	0.0	0.0	0.0	0.0
50.8	0.0					53.5	-16.1	0.0	0.0	22.5	0.0	0.0	0.0	13.9	0.0	24.1	0.0
						37.4	15.0	0.0	0.0	0.0	0.0			0.0	0.0	20.9	0.0
						30.5	0.0			21.4	0.0			0.0	0.0	21.4	0.0
						28.4	0.0									18.2	0.0
						0.0	0.0									17.1	0.0
						27.8	0.0									0.0	0.0
						28.9	0.0									0.0	0.0
						23.0	0.0									0.0	0.0
						0.0	0.0									0.0	0.0
						36.0	0.0									0.0	0.0
						0.0	0.0									17.7	0.0
						0.0	0.0									20.9	0.0
						0.0	0.0									1.1	0.0
						0.0	0.0									18.7	0.0
						34.2	0.0									17.1	0.0
						0.0	0.0									0.0	0.0
						0.0	0.0									19.8	0.0
						0.0	0.0									0.0	0.0
																0.0	0.0

Table XXVI. Observed peak flow rates for application of cyclic tensile stresses. Material No. 1. Cycle time: 2 min load, 2 min no load. Time to reach maximum load: 0.005 to 0.01 min.

Specimen 1-8-1

Stress (psi)	No. of cycles	Av. peak flow rate
1000	6	0
2500	4	0
4100	3	0
6000	3	0
7700	4	0
9200	3	0
11000	5	0
No load for 15 hrs. He still in		
4300	4	0
6000	5	0
7700	3	0
9200	2	0
11000	4	0

Table XXVII. Observed peak flow rates for application of cyclic tensile stresses. Material No. 1. Cycle time: 2 min load, 2 min no load. Time to reach maximum load: 0.005 to 0.01 min. (Flow rates given cc/cm^2 - $sec \times 10^9$). Specimen 1-9-1.

Stress: 2600 psi				Stress: 4300 psi		Stress: 5700 psi		Stress: 7200 psi		Stress: 7600 psi	
Peak flow rates for				Peak flow rates for		Peak flow rates for		Peak flow rates for		Peak flow rates for	
Applied stress	Released stress			Applied stress	Released stress	Applied stress	Released stress	Applied stress	Released stress	Applied stress	Released stress
33.7	1.6	4.8	0.0	0.0	9.1	0.0	5.4	0.0	8.0	0.0	23.6
13.4	9.6	0.0	0.0	-3.7	8.0	-1.6	9.6	-3.2	8.6	-2.1	24.1
12.8	8.0	0.0	0.0	-2.7	8.0	0.0	50.0	-3.7	8.6	0.0	9.6
47.1	-26.8	9.6	-4.3	4.3	8.6	-3.7	18.2	-3.2	3.7	-2.1	8.0
16.1	5.4	9.1	0.0	-3.2	9.1	-4.3	32.1	-3.2	6.4	107 + off scale	107 +
14.4	3.7	2.7	-2.7	-4.3	10.2	4.3	31.6	-3.2	21.4	off scale	0.0
18.7	-10.7	0.0	0.0	-8.6	5.9	-4.3	7.5	+0.5	12.8	0.0	0.0
5.4	5.4	0.0	0.0	-3.7	5.9	-4.3	6.9			0.0	0.0
4.8	8.5	0.0	0.0	-3.2	8.6	-2.1	3.7			0.0	0.0
3.2	3.7	0.0	0.0	-5.4	9.1	0.0	5.4			0.0	0.0
2.7	10.2	0.0	0.0	-4.8	9.1	0.0	10.2			0.0	0.0
3.7	10.7			-6.9	9.1	-5.9	9.1				
1.6	4.8			-3.7	8.6	-4.3	3.7				
-4.3	9.6			-2.7	7.5						
-4.8	6.9										
-3.2	8.6										
-3.2	3.2										
-4.8	0.0										
0.0	13.4										
5.4	0.0										
7.5	0.0										
6.9	0.0										

Table XXVIII. Observed peak flow rates for application of cyclic tensile stresses. Material No. 1. Cycle time: 2 min load, 2 min no load. Time to reach maximum load: 0.005 to 0.01 min. (Load applied during flow rate delay 15 min after He inlet.) Specimen 1-10-1. (Flow rates given in $cc/cm^2 - sec \times 10^9$.)

Stress: 1200 psi		Stress: 1900 psi		Stress: 2600 psi		Stress: 4300 psi		Stress: 6000 psi		Stress: 7600 psi	
Peak flow rates for		Peak flow rates for		Peak flow rates for		Peak flow rates for		Peak flow rates for		Peak flow rates for	
Applied stress	Released stress	Applied stress	Released stress	Applied stress	Released stress	Applied stress	Released stress	Applied stress	Released stress	Applied stress	Released stress
±2.7	±2.7	±5.4	±5.4	42.0	0.0	2.7	0.0	0.0	27.8	29.4	0.0
±1.6	±1.6	±1.6	±1.1	0.0	0.0	0.0	-1.6	3.7	5.40	-1.6+ broke	
±1.6	±1.6	±1.1	±1.1	0.0	0.0	0.0	±5.4	0.0	0.0		

Table XXIX. Observed maximum flow rate for initial contact of helium at 1 atmosphere with specimens under no applied load. (Flow rates given in $cc/cm^2\text{-}sec \times 10^{-9}$.)

Specimen	Membrane thickness	Peak above background	Time to reach max. flow rate from He inlet
1-10-1	0.3 mm	107+ (off scale)	0.2 to 0.3 min
1-7-1	0.5 mm	884	0.3 min
1-9-1	0.8 mm	13.4	0.05 min
1-8-1	1.0 mm	0	10 min before load applied
2-8-1	1.0 mm	0	32 min before load applied
2-9-1	0.5 mm	0	15 min before load applied
3-7	0.5 mm	0	20 min before load applied
4-3	1.0 mm	0	2 min before load applied
4-5	0.5 mm	0	85 min before load applied

Table XXX . Observed peak flow rates for application of cyclic tensile stresses. Material No. 2. Cycle time: 2 min load, 2 min no load. Time to reach maximum load: 0.005 to 0.01 min. (Flow rates given in $cc/cm^2\text{-}sec \times 10^{-9}$.)

Specimen 2-9-1

Stress: 2500 psi				Specimen fractured on application of stress of 4100 psi
Peak flow rates for				
Applied stress	Released stress			
750.0	107.0	3.7	-1.6	
166.0	-43.0	4.8	-1.6	
58.4	-17.1	2.1	-2.7	
31.6	-6.4	5.9	0.0	
23.0	-7.5	2.1	+0.5	
17.7	-3.74	5.4	-3.2	
15.0	-3.2	0.0	0.0	
9.1	-2.7			

Table XXXI. Observed peak flow rates for application of cyclic tensile stresses. Material No. 2. Cycle time: 2 min load, 2 min no load. Time to reach maximum load: 0.005 to 0.01 min. (Flow rates given cc/cm^2-sec $\times 10^{-9}$.)

Specimen 2-8-1

Stress (psi)	No. of cycles	Av. peak flow rates
2700	3	0.0
4300	3	0.0
6000	4	0.0
7600	5	0.0

Table XXXII. Observed peak flow rates for application of cyclic tensile stresses. Material No. 3. Cycle time: 2 min load, 2 min no load. Time to reach maximum load: 0.005 to 0.01 min. (Flow rates given in $cc/cm^2\text{-}sec \times 10^{-9}$.)

Specimen 3-7-1

Stress (psi)	No. of cycles	Av. peak flow rates
2600	2	0.0
4300	2	0.0
6000	2	0.0
8000	2	0.0
9500	2	0.0
11000	broke	0.0

Table XXXIII. Observed peak flow rates for application of cyclic tensile stresses. Material No. 4. Cycle time: 2 min load, 2 min no load. Time to reach maximum load: 0.005 to 0.01 min. (Flow rates given in $cc/cm^2\text{-}sec \times 10^{-9}$.)

Specimen 4-2-36		
Stress (psi)	No. of cycles	Av. peak flow rates
4200	3	0
6000	24	0
7600	3	0
9200	2	0
11000	8	0

Table XXXIV. Observed peak flow rates for application of cyclic tensile stresses. Material No. 4. Cycle time: 2 min load, 2 min no load. Time to reach maximum load: 0.005 to 0.01 min. (Flow rates given in cc/cm^2 -sec $\times 10^{-9}$.)

Specimen 4-5-1

Stress (psi)	No. of cycles	Av. peak flow rates
4200	6	0.0
6000	40	0.0
7600	6	0.0
9400	9	0.0
11,000	35	0.0

REFERENCES

1. P. C. Carman, Flow of Gases through Porous Media (Academic Press, Inc., New York, 1956), p. 1.
2. F. J. Norton, "Permeation of Gases through Solids," J. Appl. Phys. 28, 34-39 (1957).
3. D. E. Swets, R. W. Lee, and R. C. Frank, "Diffusion Coefficients of Helium in Fused Quartz," J. Chem. Phys. 34, 17-22 (1961).
4. W. A. Rogers, R. S. Buritz, and D. Alpert, "Diffusion Coefficient, Solubility, and Permeability for Helium in Glass," J. Appl. Phys. 25, 868-75 (1954).
5. C. C. Leiby, Jr., and O. L. Chen, "Diffusion Coefficients, Solubilities, and Permeabilities for He, Ne, H_2, and N_2 in Vycor Glass," J. Appl. Phys. 31, 268-74 (1960).
6. V. O. Altemose, "Helium Diffusion through Glass," J. Appl. Phys. 32, 1309-16 (1961).
7. R. M. Barrer, Diffusion in and through Solids (Cambridge University Press, London, 1941), pp. 117-42.
8. K. B. McAfee, Jr., "Stress-Enhanced Diffusion in Glass. I. Glass under Tension and Compression," J. Chem. Phys. 28, 218-26 (1958); also "II. Glass under Shear," ibid., 226-29.
9. R. C. Frank, D. E. Swets, and D. L. Fry, "Mass Spectrometer Measurements of the Diffusion Coefficient in Steel in the Temperature Range of 25° C-90° C," J. Appl. Phys. 29, 892-98 (1958).
10. R. C. Frank, D. E. Swets, and R. W. Lee, "Diffusion of Neon Isotopes in Fused Quartz," J. Chem. Phys. 35, 1451-59 (1961).
11. A. Van Wieringen and N. Warmoltz, "On the Permeation of Hydrogen and Helium in Single Crystal Silicon and Germanium at Elevated Temperatures," Physica 22, 849-65 (1956).
12. D. Hayes, D. W. Budworth, and J. P. Roberts, "Selective Permeation of Gases through Dense Sintered Alumina," Trans. Brit, Ceram. Soc. 60,494-516 (1961).

13. W. D. Urry, "Further Studies in the Rare Gases. I. The Permeability of Various Glasses to Helium," J. Am. Chem. Soc. 54, 3887-901 (1932).

14. C. C. Van Voorhis, "The Diffusion of Helium through Several Widely Different Glasses," Phys. Rev. 23, 557 (1924).

15. Lord Rayleigh, "Studies on the Passage of Helium at Ordinary Temperature through Glasses, Crystals, and Organic Materials," Proc. Roy. Soc. (London) 156A, 350-57 (1936).

16. N. W. Taylor and W. J. Rast, "The Diffusion of Helium and Hydrogen through Pyrex Chemically Resistant Glass," J. Chem. Phys. 6, 612-19 (1938).

17. G. P. Baxter, "Note on the Leakage of Helium through Pyrex Glass at Room Temperature. III," J. Am. Chem. Soc. 61, 1597 (1939).

18. P. L. Smith and N. W. Taylor, "Diffusion of Helium through Several Glasses," J. Am. Ceram. Soc. 23, 139-46 (1940).

19. T. F. Newkirk and F. V. Tooley, "Study of the Effect of Cation Concentration and Size on Helium Permeability of Alkali-Silica Glasses," J. Am. Ceram. Soc. 32, 272-78 (1949).

20. F. J. Norton, "Helium Diffusion through Glass," J. Am. Ceram. Soc. 36, 90-96 (1953).

21. P. W. Bridgman, "Effects of Very High Pressures on Glass," J. Appl. Phys. 24, 405-13 (1953).

22. E. O. Braaten and G. Clark, "The Diffusion of Helium through Fused Silica," J. Am. Chem. Soc. 57, 2714-17 (1935).

23. E. F. Burton, E. O. Braaten, and J. O. Wilhelm, "Diffusion of Helium through Quartz: Relation to Temperature," Can. J. Research 8, 463-67 (1933).

24. W. M. Jones, "Permeability and Solubility of He^3 and He^4 in Vitreous Silica," J. Am. Chem. Soc. 75, 3093-96 (1953).

25. L. S. T'Sai and T. R. Hogness, "Diffusion of Gases through Fused Quartz," J. Phys. Chem. 36 [10], 2595-600 (1932).

26. A. E. Westman and J. Crowther, "Constitution of Soluble Phosphate Glasses," J. Am. Ceram. Soc. 37, 420-27 (1954).

27. A. F. Prebus and J. W. Michener, "Electron Microscope Investigation of Glass," Ind. Eng. Chem. 46, 147-53 (1954).

28. K. S. Evetropyev, The Structure of Glass (translated from the Russian by Consultants Bureau, Inc., New York, 1958), p. 9.

29. C. Wert and C. Zener, "Interstitial Atomic Diffusion Coefficients," Phys. Rev. 76, 1169-75 (1949).

30. C. Zener, "Theory of D_0 for Atomic Diffusion in Metals," J. Appl. Phys. 22, 372-75 (1951).

31. C. L. Babcock, S. W. Barber, and K. Fajans, "Coexisting Structures in Vitreous Silica," Ind. Eng. Chem. 46, 161-66 (1954).

32. O. L. Anderson and H. E. Bömmel, "Ultrasonic Absorption in Fused Silica at Low Temperatures and High Frequencies," J. Am. Ceram. Soc. 38, 125-31 (1955).

33. P. W. Bridgman, "Bakerian Lecture. Physics above 20,000 kg/cm^2," Proc. Roy. Soc. (London) A203, 1-17 (1950).

34. B. E. Warren, "X-Ray Determination of the Liquid Structure of Liquids and Glass," J. Appl. Phys. 8, 645-54 (1937).

35. T. Alty, "Diffusion of Monatomic Gases through Fused Silica," Phil. Mag. 15, 1035-48 (1933).

36. H. Reiss and C. S. Fuller, "Diffusion in Germanium and Silicon," in Semiconductors, edited by N. B. Hannay (American Chemical Society Monograph Series, No. 140, Reinhold Publishing Corporation, New York, 1959), pp. 225-228.

37. R. A. Swalin, "Diffusion of Interstitial Impurities in Germanium and Silicon," Phys. Chem. Solids 23, 154-155 (1962).

38. O. L. Anderson and D. A. Stuart, "Calculation of Activation Energy of Ionic Conductivity in Silica Glasses by Classical Methods," J. Am. Ceram. Soc. 37, 573-80 (1954).

39. R. C. Frank and J. E. Thomas, "Diffusion of Hydrogen in Germainum," Bull. Am. Phys. Soc. (Ser. 2) 4, 411 (1959).

40. C. S. Fuller, J. D. Severiens, "Nobility of Impurity Ions in Germanium and Silicons," Phys. Rev. 96, 21-26 (1954).

41. E. M. Pell, "Diffusion Rate of Li in Si," Bull. Am. Phys. Soc. (Ser. 2) 4, 410 (1959).

42. J. Wilks, The Third Law of Termodynamics (Oxford University Press, 1961), pp. 20, 43.

43. R. M. Barrer, "Aspects of Sorption in Porous Crystals," in Structure and Properties of Porous Materials, edited by D. H. Everett and F. S. Stone (Butterworths Scientific Publications, London, 1958), pp. 6-34.

44. S. Ross and J. P. Oliver, "On Physical Adsorption. XIII. The Adsorption Potentials and Vibrations of Inert Gases on Graphite," in Solid Surfaces and the Gas Solid Interface (American Chemical Society, Washington, D. C., 1961), Advances in Chemistry Series No. 33, pp. 301-08.

45. A. D. LeClaire, "Diffusion in Metals," in Progress in Metal Physics (Interscience Publishers, Inc., New York, 1953), Vol. 4, pp. 265-332.

46. J. N. Hobstetter, "Equilibrium, Diffusion and Imperfections in Semi-conductors," ibid., Vol. 7 (1958).

47. F. Seitz, The Modern Theory of Solids (McGraw-Hill Book Company, Inc., New York, 1940) p. 82 for H, p. 264 for He.

48. E. L. Pace, "The Theoretical Calculation of the Heat of Adsorption for Gases Physically Adsorbed on Carbon Surfaces," in Proceedings of the Fourth Conference on Carbon (Pergamon Press, New York, 1960), pp. 35-45.

49. A. B. Shand, Glass Engineering Handbook 2nd ed. (McGraw-Hill Book Company, Inc., New York, 1958) pp. 4, 38.

50. J. D. Bernal, "The Structure of Liquids," Scientific American, p. 25-134, (August 1960).

51. D. McLean, Grain Boundaries in Metals (Oxford University Press, London, 1957), pp. 17-18.

52. W. J. Urry, "Further Studies in the Rare Gases. II. The Non-Permeability of Metals Minerals, and Rocks to Helium," J. Am. Chem. Soc. 55, 3242 (1933).

53. L. A. Girifalco and H. H. Grimes, "Effect of Static Strains on Diffusion," Phys. Rev. 121, 982-991 (1961).

54. W. B. Campbell, "Diffusion Rate and Activation Energy of Helium through Single Crystal and Polycrystalline Alumina" (M. S. Thesis), Georgia Institute of Technology, 1960.

55. J. S. O'Neill, A. W. Hey, and D. T. Livey, "Density and Permeability Relationships in Fabricated Beryllia," J. Nuclear Materials 3, 125-37 (1961).

56. F. P. Knudsen, "Effect of Porosity on Young's Modulus of Alumina," J. Am. Ceram. Soc. 45, 94-95 (1962).

57. R. M. Spriggs, "Expression for the Effect of Porosity on Elastic Modulus of Polycrystalline Refractory Materials, Particularly Aluminum Oxide," J. Am. Ceram. Soc. 44, 628-29 (1961).

58. J. H. de Boer, The Dynamical Character of Adsorption (Clarendon Press, Oxford, 1953), pp. 98-122.

59. J. H. de Boer, "Atomic Forces and Adsorption," in Advances in Colloid Science, edited by H. Mark and E. J. W. Verwey (Interscience Publishers, Inc., New York, 1950), Vol. 3.

60. J. H. de Boer, "The Shapes of Capillaries," ibid., pp. 68-95.

61. D. H. Everett, "Some Problems in the Investigation of Porosity by Adsorption Methods," op. cit., pp. 95-120 (141).

62. E. A. Flood, "Statistical Descriptions, Correlation Factors, and Physical Properties of Granular and Porous Solids," op. cit. pp. 151-182.

63. P. K. C. Wiggs, "The Relation Between Gas Permeability and Pore Structure of Solids," op. cit., pp. 183-94.

64. J. Marin, Mechanical Behavior of Engineering Materials, (Prentice-Hall, Inc., Englewood Cliffs, New Jersey, 1962), pp. 138-140.

65. S. Timoshenko, and S. Wainowsky-Krieger, Theory of Plates and Shells (McGraw-Hill, Book Co., Inc., New York, 1959).